


5-2018

## Phase Transitions in Monochalcogenide Monolayers

Mehrshad Mehboudi  
*University of Arkansas, Fayetteville*

Follow this and additional works at: <https://scholarworks.uark.edu/etd>

 Part of the [Applied Mechanics Commons](#), [Nanoscience and Nanotechnology Commons](#), [Polymer and Organic Materials Commons](#), and the [Semiconductor and Optical Materials Commons](#)

---

### Citation

Mehboudi, M. (2018). Phase Transitions in Monochalcogenide Monolayers. *Graduate Theses and Dissertations* Retrieved from <https://scholarworks.uark.edu/etd/2773>

This Dissertation is brought to you for free and open access by ScholarWorks@UARK. It has been accepted for inclusion in Graduate Theses and Dissertations by an authorized administrator of ScholarWorks@UARK. For more information, please contact [scholar@uark.edu](mailto:scholar@uark.edu), [uarepos@uark.edu](mailto:uarepos@uark.edu).

Phase Transitions in Monochalcogenide Monolayers

A dissertation submitted in partial fulfillment  
of the requirements for the degree of  
Doctor of Philosophy in Microelectronics-Photonics

by

Mehrshad Mehboudi  
University of Tehran  
Bachelor of Science in Mechanical Engineering 2004  
Iran University of Science and Technology  
Master of Science in Mechanical Engineering, 2007  
University of Arkansas  
Master of Science in Microelectronics-Photonics, 2014

May 2018  
University of Arkansas

This dissertation is approved for recommendation to the Graduate Council.

---

Salvador Barraza-Lopez, Ph.D.  
Dissertation Director

---

Pradeep Kumar, Ph.D.  
Committee Member

---

Paul Millett, Ph.D.  
Committee Member

---

Hugh Churchill, Ph.D.  
Committee Member

---

Rick Wise, Ph.D.  
Ex-Officio Member

The following signatories attest that all software used in this dissertation was legally licensed for use by Mehrshad Mehboudi for research purposes and publication.

---

Mr. Mehrshad Mehboudi, Student

---

Dr. Salvador Barraza-Lopez, Dissertation Director

This dissertation was submitted to <http://www.turnitin.com> for plagiarism review by the TurnItIn company's software. The signatories have examined the report on this dissertation that was returned by TurnItIn and attest that, in their opinion, the items highlighted by the software are incidental to common usage and are not plagiarized material.

---

Dr. Rick Wise, Program Director

---

Dr. Salvador Barraza-Lopez, Dissertation Director

## Abstract

Since discovery of graphene in 2004 as a truly one-atom-thick material with extraordinary mechanical and electronic properties, researchers successfully predicted and synthesized many other two-dimensional materials such as transition metal dichalcogenides (TMDCs) and monochalcogenide monolayers (MMs). Graphene has a non-degenerate structural ground state that is key to its stability at room temperature. However, group IV monochalcogenides such as monolayers of SnSe, and GeSe have a fourfold degenerate ground state. This degeneracy in ground state can lead to structural instability, disorder, and phase transition in finite temperature. The energy that is required to overcome from one degenerate ground state to another one is called energy barrier ( $E_c$ ). Density Functional Theory (DFT) has been used to calculate energy barriers of many materials in this class such as monolayers of SiSe, GeS, GeSe, GeTe, SnSe SnS, SnTe, PbS, and PbSe along with phosphorene. Degeneracy in the ground state of these materials leads to disorder at finite temperature. This disorder arises in the form of bond reassignment as a result of thermal excitement above a critical temperature ( $T_c$ ).  $T_c$  is proportional to  $E_c/K_B$  where  $K_B$  is Boltzmann's constant. Any of those materials that have a melting temperature larger than  $E_c/K_B$  such as SnSe, SnS, GeSe, and GeS will undergo an order-disorder phase transition before melting point. This order-disorder phase transition will have a significant effect on properties of these 2D materials.

The optical and electronic properties of GeSe and SnSe monolayers and bilayers have been investigated using Car-Parrinello molecular dynamics. These materials undergo phase transition from an average rectangular unit cell below  $T_c$  to an average square unit cell above  $T_c$  where  $T_c$  is well below the melting point. These materials will remain semiconductors below and above  $T_c$ . However, the electronic, optical, and piezoelectric properties modify from earlier predicted values.

In addition, the X and Y points of the Brillouin zone become equivalent as the materials passes  $T_c$  leading to a symmetric electronic structure. The spin polarization at the conduction valley vanishes. The linear optical absorption band edge changes its polarization and makes this structural and electronic transition identifiable by optical means.

## **Acknowledgement**

Foremost, I would like to express my special thanks to my dissertation director, Professor Salvador Barraza-Lopez, for his patience, continuous support, guidance and immense patronage toward completion of this dissertation.

My sincere thanks to Dr. Rick Wise, the director of the microEP program for all his help, motivation, and enthusiasm.

I would like to thank the rest of my group members and collaborators, especially Dr. Pradeep Kumar, Dr. Hugh Churchill for all their help and consulting.

I would like to thank my wife and my son for helping me and loving me during completing my research.

This research study was financially supported by an early career grant from US Department of Energy (DOE), Grant No. SC0016139. Any opinions, findings, and conclusions or recommendations expressed in this material are those of the author and do not necessarily reflect the views of the Department of Energy (DOE).

The calculations of this work were performed on Arkansas Razor and Trestles High Performance Computing Center which is funded through multiple National Science Foundation Grants and Arkansas Economic Development Commission.

## **Dedication**

This thesis is dedicated to my family and my friends.

## Table of Contents

1	Chapter One: Introduction.....	1
2	Chapter Two: Review and motivation.....	4
2.1	2D materials .....	4
2.2	Graphene family.....	5
2.3	Two-dimensional materials based on chalcogens .....	6
2.3.1	Transition metal dichalcogenides (TMDCs):.....	7
2.3.2	Monochalcogenides .....	8
3	Chapter Three: Computational methodology .....	16
3.1	Effective Schrödinger single-particle problem .....	16
3.2	Born-Oppenheimer approximation .....	18
3.3	Hartree-Fock approximation .....	20
3.4	Density Functional Theory (DFT).....	20
3.5	Exchange-correlation energy approximations.....	23
3.6	Local density approximation (LDA).....	24
3.7	Generalized Gradient Approximation (GGA).....	24
3.8	Van der Waals .....	24
3.9	Package codes and other considerations .....	26
4	Chapter Four: Two-dimensional disorder in phosphorene and group IV monochalcogenide monolayers.....	28
4.1	Introduction .....	28
4.2	Lattice parameters of phosphorene and MMs .....	29



4.3	Degeneracy and energy barrier calculations in phosphorene and MMs .....	32
4.4	Energy landscape.....	35
4.5	More on the second source of degeneracy .....	37
4.6	Effect of temperature on the atomic structure by MD calculation.....	38
4.7	Evolution of average lattice parameters $a_1$ and $a_2$ with temperature.....	39
4.8	Discussion and summary.....	47
5	Chapter Five: Structural phase transition in group IV monochalcogenide monolayers and bilayers .....	51
5.1	Introduction: phase transitions in crystalline materials.....	51
5.2	Car-Parrinello MD calculations .....	52
5.3	Transition temperature from MD calculations.....	52
5.4	Material properties of monolayers and bilayers of GeSe and SnSe.....	58
5.5	Electronic band gap and density of states .....	60
5.6	Optical absorption .....	63
5.7	Piezoelectricity and pyroelectricity .....	64
5.8	Summary and discussion.....	66
	References.....	68
	Appendix A: Description of research for popular publication.....	76
	Appendix B: Executive summary of newly created intellectual property .....	78
	Appendix C: Potential patent and commercialization aspects of listed intellectual property items.....	79
	Appendix D: Broader impact of research .....	80

Appendix E: Microsoft Project for PhD Micro-EP degree plan .....	82
Appendix F: Identification of all software used in research and dissertation generation.....	83
Appendix G: Publications and Presentations.....	85

## List of Figures

Figure 1. Hexagonal lattice structure of HBN and graphene.....	6
Figure 2. Lattice structure of MoS <sub>2</sub> from different views.....	7
Figure 3. Monochalcogenide monolayers atomic structures a) GeSe b) PbTe.....	8
Figure 4. One layer of black phosphorus and its unit cell. ....	9
Figure 5. Some elements of group IV and VI of the periodic table.....	11
Figure 6. Group IV monochalcogenides.....	11
Figure 7. One layer of black phosphorus. Zigzag and armchair direction are shown. ....	13
Figure 8. Self-consistent method used in DFT method. ....	26
Figure 9. The structure of phosphorene from different views. A single unit cell and lattice vectors are also shown. ....	30
Figure 10. a) The atomic structure of GeSe from different views and b) the atomic structure of PbTe from different views. ....	31
Figure 11. The correlation of the aspect ratio of rectangular unit cell with MMs mean atomic number. ....	33
Figure 12. The structure of graphene remains unchanged upon a) three-fold rotations and b) reflection about symmetric axis.....	34
Figure 13. The structure of MMs and phosphorene changes upon mirror transformation about symmetric axis. ....	34
Figure 14. The energy landscape of GeS. Two ground states are labeled A and B. The barrier is of the order of 500 K.....	35
Figure 15. The logarithm of the energy barrier for different MMs unveils exponential dependence of the energy barrier with the mean atomic number. ....	37
Figure 16. Atomic decoration of four degenerate ground state on MMs.....	38
Figure 17. Snapshot of MD results at 300 K for different materials. Materials labeled in red have an energy barrier smaller than 300 K and undergo bond reassignments. ....	40
Figure 18. Snapshot of MD results at 1000 K for different materials, showing a melting of most materials except phosphorene (BP).....	41

Figure 19. The evolution of internal potential energy $U$ of a) GeS and b) GeSe with temperature. ....	45
Figure 20. The evolution of the rate of the change of internal energy of a) GeS and b) GeSe with temperature. ....	45
Figure 21. The evolution of the ratio of the two lattice parameters by temperature (top) and its rate of change (bottom).....	47
Figure 22. Snapshot of atomic structure at 100 K, 200 K, and 300 K for GeS (top) and GeSe (bottom).....	48
Figure 23. Snapshot of atomic structure at 400 K, 500 K, and 600 K for GeS (top) and GeS (bottom).....	49
Figure 24. Time evolution instantaneous temperature and energy of the structure (GeSe ML). .	53
Figure 25. Time evolution instantaneous temperature and energy of the structure (SnSe ML)..	53
Figure 26. Structural order parameters. $a_1$ $a_2$ are lattice parameters, $d_1$ , $d_2$ and $d_3$ are the first, second, and third nearest neighbor distances.....	55
Figure 27. Time evolution of order parameters for GeSe ML.....	56
Figure 28. Time evolution of order parameters for GeSe BL.....	56
Figure 29. Time evolution of order parameters for SnSe BL. ....	57
Figure 30. Time evolution of order parameters for SnSe ML. ....	57
Figure 31. The evolution of averaged order parameters by temperature for GeSe monolayer and bilayers. ....	59
Figure 32. The evolution of averaged order parameters by temperature for SnSe monolayer and bilayer.....	60
Figure 33. Highly symmetrical points of MMs structure. ....	61
Figure 34. Band structure and density of states of SnSe monolayer and bilayer.....	62
Figure 35. Band structure and density of states of GeSe monolayer and bilayer. ....	62
Figure 36. The evolution of optical absorption of four investigated materials.....	64
Figure 37. The temperature evolution of the dipole moment and pyroelectric response of GeSe and SnSe monolayers. ....	65

## List of Tables

Table 1. Common 2D materials .....	5
Table 2. The lattice parameters of MMs using VASP code and PBE pseudo-potentials .....	31
Table 3. The lattice parameters of MMs using VASP code and LDA pseudo-potentials. ....	32
Table 4. Energy barrier of MMs using VASP code.....	36
Table 5. Average lattice parameters for phosphorene and MMs at four temperatures.....	43
Table 6. The band gap of SnSe and GeSe monolayers and billayers at $T = 30$ K, $T = T_c$ and $T > T_c$ .....	63

## 1 Chapter One: Introduction

Two-dimensional materials are considered a great opportunity for future devices due to two facts. First, since the electronic charge of two-dimensional materials is confined in 2D, their properties are different from that of their bulk form. Second, the properties of two-dimensional materials are correlated to their shape and geometry [1,2]. This fact leads to the possibility of tuning optoelectronic and mechanical properties by inducing strain or curvature in these materials [2]. Phosphorene is a two-dimensional material that acquired more attention in 2014 [3-5]. Black phosphorus, the bulk form of phosphorene, has been known to humans for almost a century [6]. Phosphorene has a band gap which makes it a potential optoelectronic material. However, this material is reactive and degrades with oxygen.

The excitement about phosphorene led to discovery of a new class of materials which is compounds of elements in group IV and VI of the periodic table [5]. These materials are called monochalcogenide monolayers (MMs). MMs are semiconductors with suitable band gap value for optoelectronic applications. In addition, they possess a piezoelectric effect [7,8] and photostriction [9].

Most numerical calculations on phosphorene and MMs are performed at zero temperature. However, one of the main results from the present dissertation is that the movement of ions at finite temperature will have effects on the promising properties of these materials. In addition, the reduced symmetry in the rectangular unit cell of these materials will cause the unit cell to have at least two choices to place in the structure of the material, vertical or horizontal. This fact may cause disorder at finite temperature for some of the materials in this class because some unit cells will stand vertically and some horizontally [10,11]. The main part of this dissertation focuses on the structure of phosphorene and MMs and the evolution of these structures by temperature. In addition, as the structure changes at finite temperature, the electronic, optical, and piezoelectric

properties of these materials become altered. These modifications to mentioned properties of phosphorene and MMs are discussed as well.

The ground state structure and electronic properties of crystalline materials are to calculate by solving a many-body Schrödinger equation. Solving Schrödinger many-body problem will result in a wave-function which can be used to obtain all the properties of the material. However, due to the complexity of this equation, Density Functional Theory (DFT) method has been used to approximate ground states and properties of crystalline materials. The principles of the DFT method were established five decades ago by Walter Kohn, Lu Sham and Pierre Hohenberg [12,13]. In DFT, instead of solving the many-body problem for wave-function, the objective is to find a fictitious potential for the material to have the same effect as all the electrons of the material. This non-interacting potential is only a function of electron density. Finding the effective potential is one of the challenges of the DFT method. The fast improvement in computation tools and modification of effective potentials have made DFT a reliable and popular method to predict the electronic, chemical, and mechanical properties of materials.

To outline this dissertation, in Chapter Two the DFT methodology (which contains a brief description of Schrödinger many-body problem) will be explained. In addition, the types of pseudo-potentials that have been used in this dissertation will be discussed. In Chapter Three, a literature review on two-dimensional class of materials with a focus on chalcogen compounds is presented.

Chapter Four is devoted to the atomic structure of phosphorene and monochalcogenide monolayers. In this chapter, the atomic structure of these materials is discussed. This contains the results of DFT calculations to find the lattice parameters and basis vectors of these materials. In addition, the results of Car-Parrinello molecular dynamics calculation are used to study possible order to disorder phase transition in monochalcogenide monolayers at finite temperature.

Chapter Five is the continuation of Chapter Four, with more emphasis on the effect of temperature on the electronic and piezoelectric properties of germanium selenide (GeSe) and tin selenide (SnSe) monolayers and bilayers. The reason behind choosing these materials from the monochalcogenide family is that the transition temperature of these materials is close to room temperature, and well below their melting points. Car-Parrinello molecular dynamics (i.e, where forces are computed from DFT) is used to explore the structure and properties of four mentioned materials at different temperatures ranging from 0 K to 1000 K with steps of 25 K. In this chapter, signatures of two-dimensional structural phase transitions in GeSe and SnSe monolayers and bilayers are derived from comprehensive molecular calculations. In addition, the effect of structural phase transitions, on the electronic properties such as the band gap are presented. The structural phase transition also alters optical absorption and piezoelectricity of these materials which is discussed at the end of Chapter Five.



## **2 Chapter Two: Review and motivation.**

For a long time, the existence of two-dimensional materials was considered impossible due to structural instability [14]. Therefore, it was deemed that two-dimensional materials are unstable and cannot be synthesized. However, in 2004, by exfoliating one sheet of graphite (graphene), Novoselov and Geim demonstrated not only that two-dimensional materials are stable, but they also possess extraordinary properties [15]. Graphene was considered a viable candidate to replace silicon in transistor-based devices due to extremely high carrier mobility [16,17], flexibility, and high mechanical strength. In addition, much excitement arose when the possibility of using graphene in optical devices, sensors, batteries, and so on was suggested. Graphene's band structure has a linear behavior around the K point, so that its carriers behave as massless Dirac fermions [18]. This leads to phenomena such as a quantum Hall effect at room temperature [19] and provides a new field as Fermi-Dirac physics. Although graphene is only one atom thick, it has very high electronic and thermal conductivity [20-22]. Graphene properties become altered in presence of different substrates [23,24], mechanical deformation [25-27], and external electronic field [28,29].

Graphene is comprised of only one element of the periodic table. The possibility of fabricating other two-dimensional materials with novel physical properties provides extensive opportunities for research.

### **2.1 2D materials**

Many 2D materials have been synthesized and characterized after the discovery of graphene. Most of these 2D materials originate from exfoliating van der Waals materials. A van der Waals material in two-dimensions has strong covalent or ionic bonds and weak van der Waals interaction in the third dimension. Table 1 shows a summary of different types of 2D materials. A brief introduction to different types of 2D materials is provided afterward.

Table 1. Common 2D materials.

Graphene Family	graphene	HBN	Fluorographene	BCN
monochalcogenides and puckered single element 2D materials	GeSe, SnSe, SnS, GeS, phosphorene	stanene, germanene	GaS, GaSe, InSe, GaTe, Bi <sub>2</sub> Se <sub>3</sub>	
Transition metal Dichalcogenides	MoS <sub>2</sub> , WS <sub>2</sub> , MoSe <sub>2</sub> , WSe <sub>2</sub>	MoTe <sub>2</sub> , WTe <sub>2</sub>	NbSe <sub>2</sub> , NiSe <sub>2</sub> , NbS <sub>2</sub> ,	
Trichalcogenides	CrSiTe <sub>3</sub> , CrGeTe <sub>3</sub> , MnPS <sub>3</sub>			
Oxides	Mo <sub>3</sub> , WO <sub>3</sub>	Proveskite: Ca <sub>2</sub> Ta <sub>2</sub> TiO <sub>10</sub> , Bi <sub>4</sub> Ti <sub>3</sub> O <sub>12</sub>	Hydroxides: Ni(OH) <sub>2</sub> ,	

## 2.2 Graphene family

This group consist of graphene, graphene bilayer, graphene oxide, and chemically modified graphene. Hexagonal boron nitride (HBN) can also be placed in this family. This group will be selected from its hexagonal honeycomb unit cell.

Graphene has semimetal properties with high intrinsic carrier mobility of  $200,000 \frac{\text{cm}^2}{\text{V}\cdot\text{s}}$  [30], a high Young modulus of approximately 1.0 TPa [31], and high thermal conductivity of  $5000 \frac{\text{W}}{\text{m}\cdot\text{K}}$  [22]. Bernal bilayer (AB) graphene consists of two layers of graphene stacked together in an AB pattern which means the top layer of graphene is shifted with respect to the lower layers by  $(\vec{a}_1 + \vec{a}_2)/3$ , where  $\vec{a}_1$  and  $\vec{a}_2$  are the lattice vectors.

AB graphene maintains semimetal properties of graphene and can synthesized by graphite exfoliation [32] or CVD [33]. The zero-band gap of AB graphene can be modified by applying an electric field [34]. Fluorographene is a graphene derivative with  $\text{sp}^3$  hybridized carbon atoms bonded to a fluorine atom. Fluorographene has a wide band gap of 3.8 eV [35]. Hexagonal boron nitride (HBN) in bulk form is a van der Waals material very much like graphite. The weak interaction between layers allows it to be synthesized down to a monolayer. HBN has a wide band

gap of 5.9 eV and is widely used as an insulator in production of ultrahigh mobility 2D heterostructures. The structure of graphene and HBN are illustrated in Figure 1.

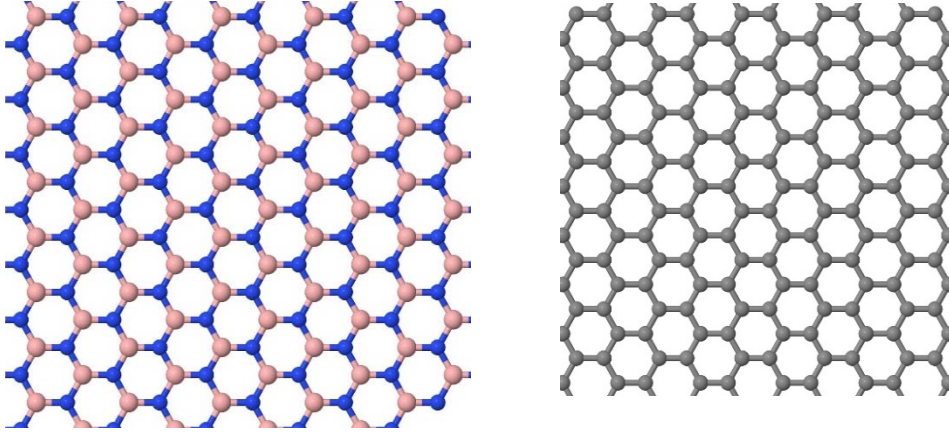


Figure 1. Hexagonal lattice structure of HBN and graphene.

### 2.3 Two-dimensional materials based on chalcogens

Chalcogens are elements in the sixth column of the periodic table (oxygen, sulfur, selenium, and tellurium). Bulk chalcogenide compounds have become a great material choice as an electronic material. For example, the best thermoelectric materials, such as PbTe and Bi<sub>2</sub>Te<sub>3</sub>, are chalcogenides [36,37]. Interestingly, many good topological insulators, such as Sb<sub>2</sub>Te<sub>3</sub> and Bi<sub>2</sub>Se<sub>3</sub> [38] are compounds of chalcogenides. The next generation of solar cells are very likely to be made of direct band gap compounds of CdTe and other chalcogenide compound. Superconductivity and magnetism are also other applications of chalcogenide compounds. FeS and FeSe are two examples of chalcogenides with superconducting properties at atmospheric pressure [39-41]. Most of these chalcogenides have weak van der Waals interaction between layers, which means they can be exfoliated mechanically and possibly down to a monolayer. Therefore, one can expect to predict many stable 2D materials based on chalcogens.

### 2.3.1 Transition metal dichalcogenides (TMDCs):

With the formula of  $\text{TX}_2$  where T is a transition metal element (Ti, Zr, Hf, V, Nb, Ta, Mo and W) and X represents a chalcogen (S, Se and Te), TMDCs are a large group of 2D materials. The structure of these 2D materials has three sublayers. The middle sublayer is formed by metal elements which is sandwiched by two chalcogen sublayers. A feature of these materials is the electronic band gap increases by moving from multilayer to monolayer. In addition, the indirect band gap in the bulk form transforms to a direct one in the monolayer. These materials have a suitable band gap, decent carrier mobility, high on/off ratio, and can be easily exfoliated. High performance transistors are fabricated and characterized using monolayers of molybdenum

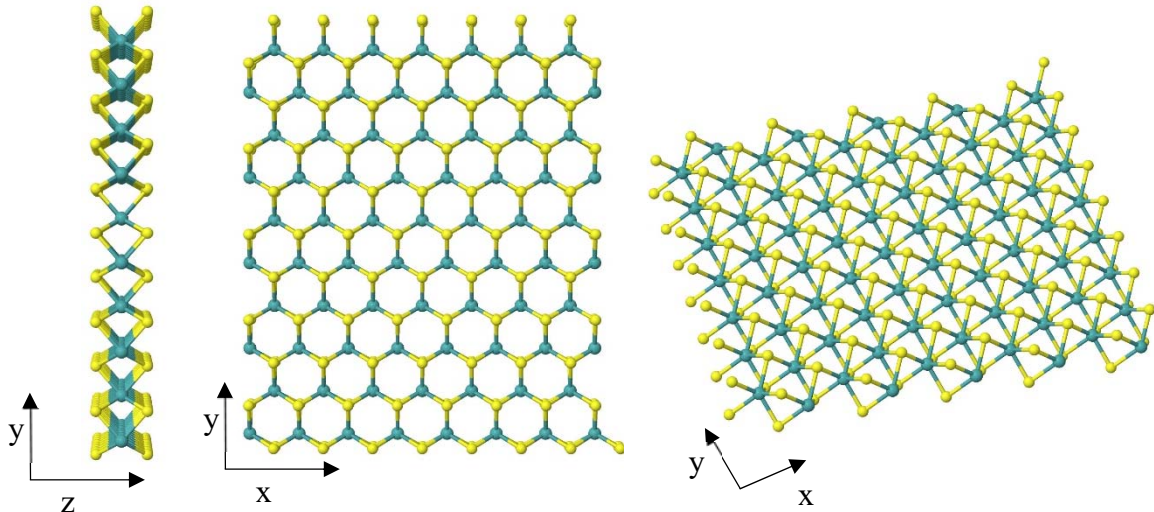


Figure 2. Lattice structure of  $\text{MoS}_2$  from different views.

disulfide [42-44]. Transition metal dichalcogenides (TMTCs) also have very good catalytic activities and have lower cost compared to noble metals [45]. Figure 2 shows the structure of  $\text{MoS}_2$ , an example of these materials.

### 2.3.2 Monochalcogenides

Among other 2D materials, phosphorene (one layer of black phosphorus) has an orthorhombic structure that differs from that of graphene and LMDCs [2,3]. This structure allows phosphorene to withstand very high strain, and shows a tunable band gap with the number of stacked layers. The discovery and synthesis of phosphorene led to a new class of 2D materials based on chalcogenides, called group IV-monochalcogenides (SnS, SnSe, GeS, and GeSe with a structure shown in Figure 3). These monochalcogenides have the same anisotropic structure as

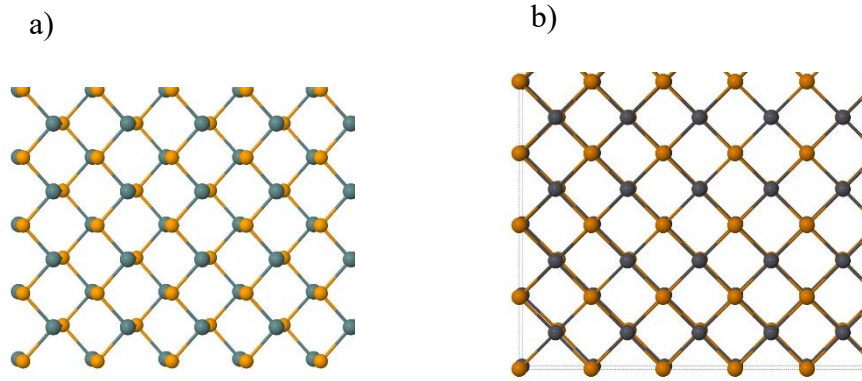


Figure 3. Monochalcogenide monolayers atomic structures a) GeSe b) PbTe.

phosphorene. This class of materials are shown to have a four-fold degenerate ground state at zero temperature that is different from other 2D materials like graphene and LMTDs with only one ground state at zero temperature. This fact suggests that phosphorene and monochalcogenides experience structural disorder at finite temperature and, consequently, have unexplored properties at room temperature.

To identify exotic properties in two-dimensions, a reasonable starting point is to review the properties of the bulk form of these materials. Therefore, in this section a brief review of properties of black phosphorus and bulk forms of group IV monochalcogenides are also presented.

**Black phosphorus:** Phosphorus is an element of group V of the periodic table with semiconducting properties and an indirect band gap of 0.3 eV [46]. The electronic configuration of phosphorus is  $1s^2 2s^2 2p^6 3s^2 3p^3$ , which allows up to five bonds with other elements. Phosphorus has many allotropes, among them red phosphorus, white phosphorus, and black phosphorus are the most common forms. Although black phosphorus is more stable than white phosphorus, it was discovered in 1914 by heating up white phosphorus under pressure [6]. Black phosphorus is a layered material with strong in-plane covalent bonds and weak van der Waals interaction between layers similar to graphite and other layer materials. However, black phosphorus has five electrons in its outer shell, which makes the structure less symmetric compared to sheets of graphite (graphene). From the top view, black phosphorus has a hexagonal lattice structure with two different bonds between phosphorus atoms. The longer one is 2.244 Å long and the shorter is 2.224 Å long as illustrated in Figure 4.

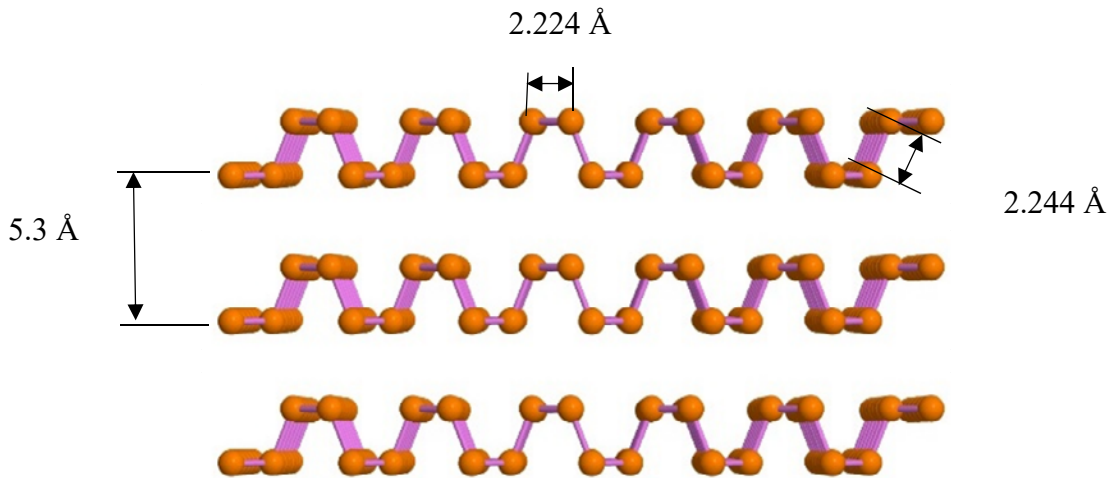


Figure 4. One layer of black phosphorus and its unit cell.

Black phosphorus is a semiconductor but during the 20<sup>th</sup> century, there was not enough interest in studying this material mainly due to much more excitement in silicon based devices. In 2014 [47] the rediscovery of black phosphorus in the context of two-dimensional materials gave a

lot of momentum to the research on this material and its 2D allotropes as candidates for optoelectronic devices. The two-dimensional form of black phosphorus is called phosphorene, which will be discussed later.

**Group IV Monochalcogenides in the bulk form:** These materials are compounds of the fourth and sixth column of the periodic table. The elements of these two groups are illustrated in Figure 5. The examples of these compound materials are SnS, SnSe, GeS and GeSe. The bulk forms of Group IV monochalcogenides have semiconducting properties and have been the subject of studies for decades [48, 49]. The structure of these materials can be classified into two groups. PbTe, PbSe, PbS and SnTe have  $Fm\bar{3}m$  space group with a rock-salt crystalline structure. On the hand, SnSe, SnS, GeSe, and GeS are classified into the  $Pcmn$  space group with an orthorhombic structure. The structure of the latter group forms a layered structure with strong in-plane covalent or ionic bonds and weak van der Waals bonds between layers. These materials have been studied extensively because of their unique properties. The nanocrystals of tin and germanium monochalcogenides have proved to have suitable photo absorption properties which makes them a suitable alternative for lead-free photovoltaic materials [50,51]. Tin selenide exhibits a very high thermal figure of merit of equal to 2.6 at 923 K along one direction and 2.3 along another direction [52]. This value for the figure of merit is comparable to the best known thermoelectric materials [53]. Thermoelectric properties are also seen in SnS and since it is an abundant material, it has been investigated as potential candidate for commercial piezoelectric devices. This material is also investigated for the next generation of solar cells [54-56]. PbS and PbSe have been used as an infrared detector in military applications. PbTe has thermoelectric properties with  $ZT$  of 1.5 at 773 K [57]. The atomic structure of GeSe in the bulk form is shown in Figure 6.

**Phosphorene:** An electronic band gap is required to switch computer circuits on and off.

Group IV	Chalcogenides
Si Silicon	O Oxygen
Ge Germanium	S Sulfur
Sn Tin	Se Selenium
Pb Lead	Te Tellurium

Figure 6. Some elements of group IV and VI of the periodic table.

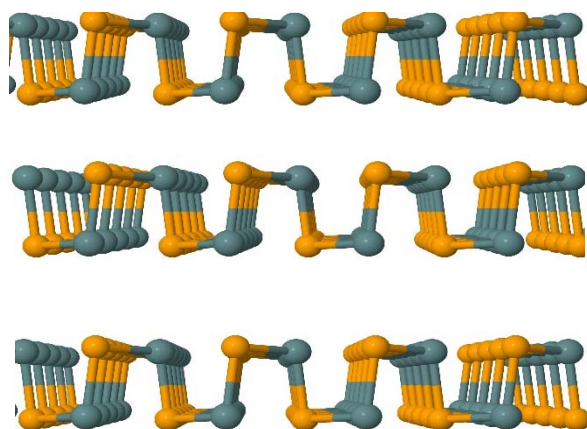


Figure 5. Group IV monochalcogenides.

Though graphene possesses unique properties such as a very high electron mobility, it lacks a natural band gap. By applying electric field to AB graphene, the band gap increases from zero to mid-infrared energies [58]. Graphene nanoribbon also has been reported to have a non-zero band



gap. The band gap of graphene nanoribbons increases as the width of ribbon decreases [59]. Despite all these efforts, the band gap is still not suitable for most applications, where a larger band gap is needed. This fact limits graphene usage as a replacement for silicon in computer circuits.

Unlike graphene, few-layer black phosphorene has a natural semiconducting band gap. The electronic band gap of black phosphorus depends on the number of stacked layers and it ranges from 0.3 eV in the bulk to 2 eV in the monolayer limit [46]. In addition to the thickness to tune electronic properties, strain is also an effective tool to alter the properties of black phosphorus. Studies show that compressive strain can change the direct band gap of black phosphorus to an indirect one and reduce the band gap to the limits of a metal [60]. The transport properties of black phosphorus are somewhere between those of graphene and transition metal dichalcogenides. The electron mobility of phosphorene is around  $1000 \text{ cm}^2/\text{V}\cdot\text{s}$  and hole mobility is in the order of  $286 \text{ cm}^2/\text{V}\cdot\text{s}$ , which makes it a viable candidate for electronic applications [46]. Rather than electronic band gap and transport properties, perhaps the most celebrated property of phosphorene is its in-plane anisotropic behavior. Phosphorene has an armchair structure along one direction and zigzag structure along the other perpendicular direction. Along the armchair direction, atoms are puckered and along the zigzag direction, atoms form a “bilayer” structure as seen in Figure 7.

This unique structure is responsible for angle dependent properties of phosphorene. For instance, the anisotropic Raman response of few layer phosphorene enables one to determine its orientation much easier without using scanning tunneling microscopy or tunneling electron microscopy[61]. The mobility and electron effective mass of phosphorene and few layer black phosphorus, and their optical properties, also depends on the angle [62-64].

**Challenges of phosphorene:** The main challenge of using black phosphorus in real devices is its tendency to degrade by oxygen and water [65]. Nevertheless, a dimer of oxygen requires 10

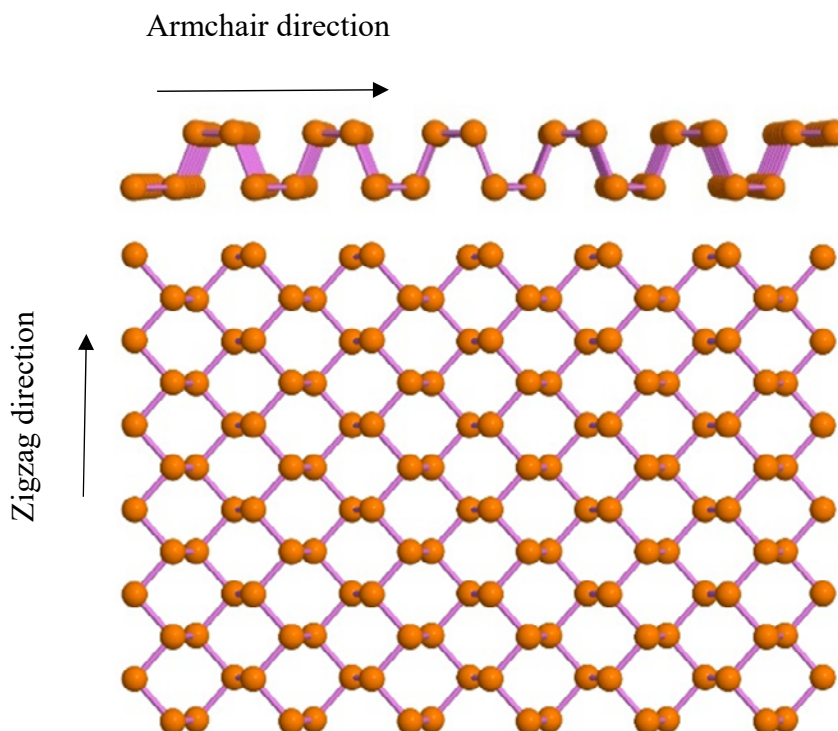


Figure 7. One layer of black phosphorus. Zigzag and armchair direction are shown.

eV (250 kcal/mol) energy to be added to an ideal phosphorene structure [66]. This value is much higher than the energy of visible light and suggests that ideal phosphorene does not degrade in ambient light. However, this chemisorption barrier is reduced to the energy of visible light (3.2 eV) in presence of structural defects and the curvature of the phosphorene sheet [66]. The promising optical and electronic properties of phosphorene and other single element 2D materials in group V intrigue researchers to investigate their counterparts which are compounds of group IV and VI elements of the periodic table.

**Group IV Monochalcogenides Monolayers (MMs):** Investigating phosphorene's isoelectronic counterparts is similar to broadening the scope of silicon by investigating compounds of group III and group V elements. The bulk form of these materials exhibits unique properties. In early works on MMs in 2011, nano sheets of SnSe, but not necessarily monolayers, were

synthesized and characterized [67]. However, the single layer of SnSe [68] and GeSe [69] were synthesized. Due to promising properties of group IV monochalcogenides, numerical calculations predicted the stability of their two-dimensional forms [5,70]. In addition, MMs were considered as phosphorene's isoelectronic counterparts. Most of MMs are semiconductors with electronic band gaps ranging from 0.9eV to 1.7eV. These band gaps are mostly indirect, except for GeSe, which has a direct band gap. The application of some of MMs, such as GeS and GeSe as cathode catalysts in Li-O<sub>2</sub> batteries [71] and in the photocatalytic splitting of water [72], are explored numerically. In addition, these materials are potentially desirable for efficient oxygen reduction reactions [71] and developing photostriction effects [9]. Thermoelectricity has been observed in the bulk form of these materials, with great promise due to high a figure of merit. DFT calculations show that the MMs exhibits better thermoelectric properties than their bulk form [73]. For example, the thermoelectric figure of merit ( $ZT$ ) is 2.63 for a SnSe monolayer, which is more than its value of 2.43 for the bulk form. The same results have been observed for other compounds of MMs such as SnS, GeSe, and GeS [73]. Great interest in these materials arose when numerical calculations showed that MMs have piezoelectric properties[7,8]. It is numerically predicted that all four compounds of GeS, GeSe, SnSe, and SnS have piezoelectric coefficients one or two orders of magnitude larger than that of other 2D materials [8]. These numerical calculations have been performed at zero temperature. However, it is essential to investigate whether these materials maintain their large piezoelectricity effect at finite temperature. This fact is discussed with more detail in Chapters Four and Five.

Ferroelectricity has also been observed experimentally in some of these materials such as SnTe. The bulk form of SnTe exhibits ferroelectric properties at temperatures below 98 K. The SnTe monolayer retains its ferroelectricity at 270 K which is near room temperature[74]. SnTe

monolayer makes a transition from a ferroelectric material to paraelectric material at 270 K. This transition can be explained as a result of phase transition from a rectangular unit cell to a square one. This fact is discussed in more detail in Chapters Four and Five.

### 3 Chapter Three: Computational methodology

In this chapter, the computational methodology used in the dissertation is discussed. Density functional theory (DFT) is the main method that is used here. DFT is used in a wide range of applications such as molecular properties and structures, ionization energies, and magnetic and electronic properties. In Chapters Four and Five of this dissertation, Car-Parrinello molecular dynamics calculations are used to find the structural behavior and electronic properties of SnSe and GeSe monolayers and bilayers.

#### 3.1 Effective Schrödinger single-particle problem

All the information about a given system lies in quantum mechanical wavefunctions. In order to get the wavefunctions, one should solve Schrödinger equation (Equations 1 and 2).

$$i\hbar \frac{\partial}{\partial t} \Psi(r, t) = \left[ \frac{-\hbar^2}{2\mu} \nabla^2 + V(r, t) \right] \Psi(r, t) \quad \text{time dependent form} \quad (\text{Equation 1})$$

$$\left[ \frac{\hbar^2}{2\mu} \nabla^2 + V(r) \right] \Psi(r) = E\Psi(r) \quad \text{time independent form} \quad (\text{Equation 2})$$

$$H\Psi(r) = E\Psi(r) \quad \text{compact form} \quad (\text{Equation 3})$$

where  $i$  is the imaginary unit,  $\hbar$  is the Planck constant over  $\pi$ ,  $\frac{\partial}{\partial t}$  is the partial derivative with respect to time,  $\mu$  is the particle's reduced mass,  $H$  is the Hamiltonian,  $V$  is the effective potential energy that may include the effects from other electrons,  $\nabla^2$  is the Laplacian operator and  $\Psi$  is the position-space wavefunction.

Equation 4 shows the Schrödinger for many body problems:

$$(V_{NN} + V_{NE} + V_{EE} + T_N + T_E) \psi = E\psi \quad (\text{Equation 4})$$

where  $V_{NN}$  is the interaction between nuclei,  $V_{NE}$  is the interaction between nuclei and electrons,

$V_{EE}$  is the electron-electron interactions,  $T_N$  is the kinetic energy of nuclei,  $T_E$  is the kinetic energy of electrons, and  $\psi$  is the wave-function; they will be described in more detail later.  $\psi$  is function of the positions of all atoms and nuclei and the spin states,

$$\psi = \psi(\vec{r}_1, \vec{r}_2, \vec{r}_3, \dots, \vec{r}_l, S_1, S_2, \dots, S_l) \quad l=N+M \quad (\text{Equation 5})$$

Each of the five terms in the above Hamiltonian operator in Equation 4 can be expanded. Starting from  $T_E$  as the kinetic energy of electrons, one can write  $T_E$  as:

$$T_E = \sum_{i=1}^N \frac{\hbar^2}{2m_{ef}} \left( \frac{\partial^2}{\partial r_{i1}^2} + \frac{\partial^2}{\partial r_{i2}^2} + \frac{\partial^2}{\partial r_{i3}^2} \right) \quad (\text{Equation 6})$$

where  $i$  is the index that reflects each electron and  $\mathbf{r}$  vector is the position of each electron.  $m_{ef}$  is the effective mass of electrons.  $T_N$  in Equation 4 is the kinetic energy of nuclei and can be expressed as in Equation 7.

$$T_N = \sum_{p=1}^M \frac{\hbar^2}{2m_p} \left( \frac{\partial^2}{\partial r_{p1}^2} + \frac{\partial^2}{\partial r_{p2}^2} + \frac{\partial^2}{\partial r_{p3}^2} \right) \quad (\text{Equation 7})$$

where  $m_p$  is the mass of nuclei, and vector  $\mathbf{r}$  is the position of each nuclei and index  $p$  runs over all the nuclei.  $V_{NE}$  operator is the interaction between nuclei and electrons and can be expanded as in Equation 8.

$$V_{NE} = - \sum_{p=1}^M \sum_{i=1}^N e^2 \frac{Z_p}{4\pi\epsilon_0 r_{ip}} \quad (\text{Equation 8})$$

where  $e$  is the electron charge,  $\epsilon_0$  is vacuum permittivity constant and  $Z_p$  is atomic number of nucleus  $p$ . The electron-electron Coulomb interaction are expressed as  $V_{EE}$  which can be calculated by Equation 9.

$$V_{EE} = \sum_{i=1}^N \sum_{\substack{j=1 \\ j \neq i}}^N \frac{e^2}{4\pi\epsilon_0} \frac{1}{r_{ij}} \cdot \frac{1}{2} \quad (\text{Equation 9})$$

where  $r_{ij}$  is the distance between two electrons  $i$  and  $j$ , and factor of  $\frac{1}{2}$  takes care of double counting. The Coulomb interaction between nuclei is shown as  $V_{NN}$  and can be expressed as

$$V_{NN} = \sum_{p=1}^M \sum_{\substack{q=1 \\ p \neq q}}^M \frac{Z_p Z_q e^2}{4\pi\epsilon_0} \frac{1}{r_{pq}} \cdot \frac{1}{2} \quad (\text{Equation 10})$$

In Equation 10,  $r_{pq}$  is the distance between two nuclei and  $Z$  represents the atomic number of each one of them.

Equation 4 with all terms as defined here cannot be solved explicitly for many body problems and only can be solved for trivial cases like a hydrogen atom. Therefore, it requires other approximations. In the following, some of these approximations and simplifications will be discussed.

### 3.2 Born-Oppenheimer approximation

The first simplification to the many-body Schrödinger equation is the Born-Oppenheimer approximation [75]. This approximation assumes that the motion of atomic nuclei and electrons can be separated. Therefore, the wavefunction can be written as a product of two terms. One term is the electronic wavefunction and the other is the nuclear wavefunction. The nuclear wavefunction also may be divided into two terms, one for rotational motion of the nuclei and the other one correspond to the vibrational component of the motion. The justification of this approximation comes from the huge difference between the mass of electrons and nuclei. That means, that a small

movement of nuclei may have an “instantaneous effect” on electrons. Therefore, it is reasonable to fix the position of nuclei and only consider the movements of electrons under a fixed potential exerted by the nuclei. Mathematically, this means ignoring  $T_n$  and  $V_{nn}$  due to existence of large masses of nuclei in the denominators.

Therefore, after the Born-Oppenheimer approximation the many-body problem will reduce to a many-electron problem. That means, one only needs solve for wavefunctions of the electrons for given positions of nuclei. Equation 11 shows the reduced Hamiltonian of the many-electron Schrödinger equation.

$$H = \sum_{i=1}^N \frac{\hbar^2}{2m_{ef}} \nabla^2 r_i + \sum_{i=1}^N \sum_{\substack{j=1 \\ j \neq i}}^N \frac{e^2}{4\pi\epsilon_0} \frac{1}{r_{ij}} \cdot \frac{1}{2} + - \sum_{p=1}^M \sum_{i=1}^N e^2 \frac{Z_p}{4\pi\epsilon_0} \frac{1}{r_{ip}} \quad (\text{Equation 11})$$

Therefore, the Hamiltonian can be summarized into three terms: Kinetic energy  $T_E$ , Coulomb interaction between electrons  $V_{EE}$ , and Coulomb interaction between electrons and nuclei  $V_{EN}$ . These terms are shown in Equation 12.

$$(T_E + V_{EE} + V_{EN})\psi_n^N = E\psi_n^N \quad (\text{Equation 12})$$

where the super-index  $N$  in the wave-function indicates the fact that this remains a many-body problem. This form of Schrödinger equation is still hard to solve because the interaction between electron-electron and nuclei-electron is complicated. Two main approaches have been used to tackle this problem. One is the Hartree-Fock ansatz, and the other approach is density functional theory. Hartree and Fock presented a method to further simplify this equation by replacing Coulomb interactions by an effective potential. The Hartree-Fock approximation has been used since the beginning of quantum mechanics [76].



### 3.3 Hartree-Fock approximation

In Equation 4, the wavefunction has the general form of

$$\psi(\vec{r}_1, \vec{r}_2, \dots, \vec{r}_N, S_1, S_2, \dots, S_N) \quad (\text{Equation 13})$$

where  $\mathbf{r}$  is the position of each electron and  $S$  is the spin of the of each electron in  $z$  direction. As mentioned before, the solution of Schrödinger equation in this form is complicated. Hartree-Fock sets the trial wavefunction as a determinant of single-particle wavefunctions. Each of these wavefunctions is the solution of a one electron system with an effective potential coming from other particles.

$$\psi = \frac{1}{N!} \begin{vmatrix} \psi_1(\vec{r}_1 s_1) & \psi_1(\vec{r}_2 s_2) & \dots & \psi_1(\vec{r}_N s_N) \\ \psi_2(\vec{r}_1 s_1) & \psi_2(\vec{r}_2 s_2) & \dots & \psi_2(\vec{r}_N s_N) \\ \vdots & \vdots & \ddots & \vdots \\ \psi_N(\vec{r}_1 s_1) & \psi_N(\vec{r}_2 s_2) & \dots & \psi_N(\vec{r}_N s_N) \end{vmatrix} \quad (\text{Equation 14})$$

Each  $\psi$  in Equation 14 satisfies the following form of Schrödinger equation where  $V_{ef}(r)$  the effective potential.

$$\left( -\frac{\hbar^2}{2m} \nabla_i^2 + V_{ef}(r) \right) \psi_i(r) = E_i \psi_i(r) \quad (\text{Equation 15})$$

### 3.4 Density Functional Theory (DFT)

DFT is an approximation to deal with the ground state many-electron problem. Initially, Thomas and Fermi introduced the electron density to deal with many-body problem [77]. They proposed a functional for determining the energy of the system based on the uniform electron gas and shown in Equation 16.

$$E_{tot}[n(\vec{r})] = C \int n^{\frac{5}{3}}(\vec{r}) dr - Z \int \frac{n(\vec{r})}{r} d\vec{r} + \int \int \frac{1}{2} \frac{n(\vec{r}_1) \cdot n(\vec{r}_2)}{r_{12}} d\vec{r}_1 d\vec{r}_2 \quad (\text{Equation 16})$$

where  $E_{tot}$  the total energy is expressed solely as a functional of density which is expressed as  $n(\vec{r}_2)$  and C is:

$$C = \frac{3h^2}{10m_e} \left( \frac{3}{8\pi} \right)^{\frac{2}{3}} \quad (\text{Equation 17})$$

where  $m_e$  is mass of an electron and h is Planck's constant.

Many years later, Kohn and Hohenberg proved the possibility of using the electron density to solve the many-electron problem [78]. In this method, instead of solving the many-electron problem for wavefunctions, the focus is to find the electron density as a function of three spatial dimensions. The reason is that although the wavefunction has the complete information of the system, it depends on  $4N$  variables where  $N$  is the number of electrons. In DFT, all the variables are expressed in terms of electron density. This method avoids dealing with a wavefunction with high dimension variables. In two works in 1964 and 1965 [12,13], two theorems suggested that the ground-state total energy of a solid can be expressed in terms of electron density due to all electrons at every single point. Therefore, one can find the ground state of a material by minimizing the functional  $E(n(\vec{r}))$  with respect to electron density, which leads to

$$n(r) = \sum_{i=1}^n \int \delta(\vec{r} - \vec{r}_i) |\psi(\vec{r}_1, \vec{r}_2, \dots, \vec{r}_N)|^2 d\vec{r}_1 d\vec{r}_2 \dots d\vec{r}_N \quad (\text{Equation 18})$$

In addition, the mentioned theorems demonstrate that, for the purpose of electronic ground-state, one can work with the solution of a one electron problem with an effective potential and avoid the burden of working with electron density from a many-electron wavefunction. The basic

idea is to use the total energy functional to produce an effective potential for one electron, and use this potential to find a density equal to the ground state density of the many-electron problem. This equation is called Kohn-Sham equation and shown below.

$$(T + V_{ef})\psi_i(\vec{r}) = E_i\psi_i(\vec{r}) \quad (\text{Equation 19})$$

where  $T$  is kinetic energy operator and  $V_{ef}$  is an effective potential for a single electron state which has the same effect as the many-electron state.

It is important to find the effective potential in Equation 19. This effective potential can be determined as the functional derivative:

$$V_{ef}(\vec{r}) = \frac{\delta}{\delta(n(\vec{r}))} [E_H(n(\vec{r})) + E_{xc}(n(\vec{r})) + E_{eN}(n(\vec{r}))] \quad (\text{Equation 20})$$

where  $E_H$  is the classical Hartree function,  $E_{eN}$  is the electrostatic interaction between electrons and nuclei, and  $E_{xc}$  corresponds to the part of interactions which deviates from Hartree's term. Each of the terms on the right-hand side of the Equation 21 is part of the total energy. Adding the kinetic and ionic terms this energy can be expressed as:

$$E(n(\vec{r})) = T(n(\vec{r})) + E_H(n(\vec{r})) + E_{xc}(n(\vec{r})) + E_{eN}(n(\vec{r})) + E_{NN} \quad (\text{Equation 21})$$

where  $T(n(\vec{r}))$  is the kinetic energy of one-electron,  $E_H(n(\vec{r}))$  is the (Hartree) electrostatic energy between electron charges,  $E_{eN}(n(\vec{r}))$  is the interaction energy between nuclei and electrons,  $E_{NN}$  is the interaction energy between nuclei, and, finally  $E_{xc}(n(\vec{r}))$  is the exchange correlation term that goes beyond classical Hartree term, but which also appears in the Hartree-Fock approach.

Equations 22-26 show how each term is defined.

$$T(n(\vec{r})) = \sum_j \int \psi_i^*(\vec{r}) \hat{T} \psi_j(\vec{r}) d\vec{r} \quad (\text{Equation 22})$$

$$E_H(n(\vec{r})) = \frac{e^2}{2} \int \frac{n(\vec{r}_1)n(\vec{r}_2)}{|\vec{r}_1 - \vec{r}_2|} d\vec{r}_1 d\vec{r}_2 \quad (\text{Equation 23})$$

$$E_{eN}(n(\vec{r})) = -e^2 \sum_R Z_{\vec{R}} \int \frac{n(\vec{r})}{|\vec{r} - \vec{R}|} d\vec{r} \quad (\text{Equation 24})$$

$$E_{NN} = \frac{e^2}{2} \sum_{\vec{R}_1} \sum_{\vec{R}_2 \neq \vec{R}_1} \frac{Z_{\vec{R}_1}}{Z_{\vec{R}_2}} \quad (\text{Equation 25})$$

$$E_{xc}(n(\vec{r})) = \int n(\vec{r}) \varepsilon_{exch}(n(\vec{r})) d\vec{r} \quad (\text{Equation 26})$$

By looking at these terms, one can see that Kohn and Sham placed all the complexity of the energy into functional exchange-correlation energy.

### 3.5 Exchange-correlation energy approximations

The only unknown term in Kohn-Sham energy term is the exchange-correlation term. Estimating exchange interactions is one of the fundamental parts of density functional theory. The first step to find exchange correlation energy is to divide it into two terms, one is related to the exchange term and the other related to the correlation term.

$$E_{exch}(n(\vec{r})) = E_x(n(\vec{r})) + E_c(n(\vec{r})) \quad (\text{Equation 27})$$

The idea here is to find the exact form for the large part and make an estimate for the smaller part. There are many methods that approximates this term. Local density approximation (LDA) [79], and generalized gradient approximation (GGA) [80,81] are two popular methods to approximate exchange-correlation energy, and further development permit taking care of van der

Waals interactions in the layered materials that are of concern in the present dissertation.

### 3.6 Local density approximation (LDA)

The LDA assumes that the density of a solid as a function of homogeneous electron gas:

$$E_{exch}^{LDA}(n(\vec{r})) = \sum_{\sigma} -\frac{2}{3} \frac{3}{2} \left(\frac{3}{4\pi}\right)^{\frac{1}{3}} \int n_{\sigma}^{\frac{4}{3}}(\vec{r}) d\vec{r} \quad (\text{Equation 28})$$

and the correlation part are estimated by quantum Monte-Carlo simulation [82]. In cases where the density undergoes sharp spatial changes this method has limitations. Examples of limitations are magnetism in iron, and overestimating the dielectric constant. LDA can be improved by including the gradient of the electron density in approximating the ground state exchange correlation energy, and the generalized gradient approximation is an example of this approach.

### 3.7 Generalized Gradient Approximation (GGA)

In GGA, the exchange correlation energy is written not only as a function of density functions, but of the gradient of the density as well, which is calculated numerically. One example of this method is the Perdew–Burke–Ernzerhof (PBE) exchange-correlation functional [83], which has been used in many DFT calculations in this dissertation.

### 3.8 Van der Waals

LDA gives an appropriate approximation to simple dense homogeneous systems like metals and semiconductors. GGA and other methods of the semi-local family are reliable for more complicated compounds like transition metals and interfaces [84]. However, in many systems, the long-ranged van der Waals interactions, where electron interactions are sparse, play a significant role. Local or semi-local density functionals fail to describe these interactions effectively. To

tackle this issue, van der Waals exchange correlations are proposed to deal with non-local electron density interactions[84-86]. Van der Waals method describes the exchange correlation in three terms:

$$E_{exch}(n(\vec{r})) = E_x^{GGA}(n(\vec{r})) + E_c^{LDA}(n(\vec{r})) + E_c^{nl}(n(\vec{r})) \quad (\text{Equation 29})$$

where  $E_x^{GGA}$  is the exchange energy and it is approximated by GGA. The correlation part consists of a local part  $E_c^{LDA}$  and a non-local part  $E_c^{nl}$ .

The non-local part can be written as:

$$E_c^{nl}(n(r)) = \frac{1}{2} \iint d^3\vec{r}_1 d^3\vec{r}_2 n(\vec{r}_1) n(\vec{r}_2) f(q_1, q_2, |\vec{r}_1 - \vec{r}_2|) \quad (\text{Equation 30})$$

where function  $f$  is a general kernel and can be written as a function of  $q_1$  and  $q_2$  and the position vectors.  $q_1$  and  $q_2$  are obtained using the general function:

$$q_0[n(\vec{r}), |\nabla n(\vec{r})|] \quad (\text{Equation 31})$$

The non-local correlation energy in the Equation 30 can be directly calculated by integration. This equation has been used effectively in many systems [87]. However, the double spatial integration is not efficient for large systems which requires more approximations. Reference [85] provides an approximation to the non-local part of correlation energy by fixing  $q_1$  and  $q_2$  and expanding the kernel  $f$  in Equation 30 as:

$$f(q_1, q_1, |r_1 - r_2|) = \sum_{\alpha\beta} f(q_\alpha, q_\beta, |r_1 - r_2|) p_\alpha(q_1) p_\beta(q_2) \quad (\text{Equation 32})$$

where  $q_\alpha$  and  $q_\beta$  are interpolation points. For more information on this method, and how to perform interpolation, readers can refer to reference [85]. In this dissertation, the molecular

dynamics calculations on GeSe and SnSe monolayers and bilayers are performed with SIESTA code with van der Waals interactions. Figure 8 shows a schematic of different steps of solving Kohn-Sham equation also known as the self-consistent method.

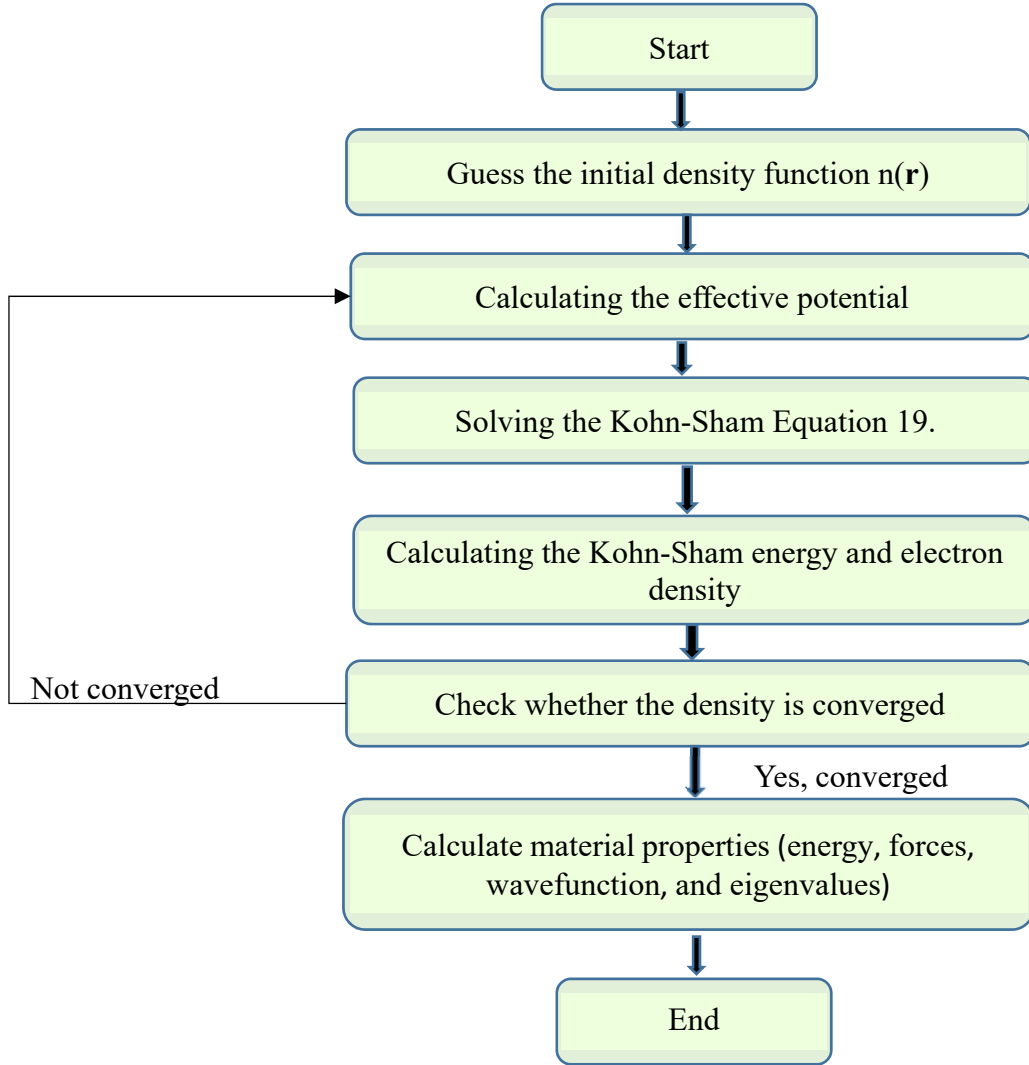


Figure 8. Self-consistent method used in DFT method.

### 3.9 Package codes and other considerations

In this dissertation, the ground state and lattice parameters of phosphorene and MMs are calculated using first principles calculations as implemented in plane-wave, density-functional

theory VASP code [88,89]. In addition, SIESTA[90-92] code has been used to perform MD calculations on monochalcogenide monolayers to predict the behavior of material at finite temperatures. For the pseudo-potentials, LDA and Pedrew-Burke-Ernzerhof (PBE) exchange-correlation functional are used in ground state calculations [81] and van der Waals exchange potential are used in molecular dynamics calculations. For the k-point sampling, Monkhorst Pack scheme [93] has been used. The k-point samplings that were used were different for different materials. For most MMs, 18x18x1 k-points were chosen. All structures were optimized until the force tolerance was smaller than 0.001 eV/Å. To ensure the interaction between layers of material did not interfere with in-plane properties, large value at the third lattice constant were considered. This vacuum space is 21 Å for phosphorene and MMs.



## **4 Chapter Four: Two-dimensional disorder in phosphorene and group IV monochalcogenide monolayers**

### **4.1 Introduction**

The focus of this chapter is on 2D materials with a rectangular unit cell, such as phosphorene, and group IV monochalcogenide monolayers (MMs) which have a lower symmetry when compared to graphene. The rectangular unit cell of phosphorene and MMs adds degeneracy to the ground state of these materials. The ground state of the hexagonal structure of graphene is non-degenerate, because atoms return to their original position upon three-fold rotations or mirror reflections. However, degeneracy is observable in materials with rectangular unit cells because the choice of the rectangular unit cell orientation (horizontal, vertical) changes the location of atoms.

Phosphorene and MMs have an additional two-fold degeneracy. The source of this additional two-fold degeneracy comes from the choice of atomic bonds in the unit cell. In fact, the choice of atomic position in the unit cell creates two additional phases.

In the following, the degeneracy in the ground state of phosphorene and MMs are discussed by exploring the effect of lattice shape and atomic number on the energy of these materials. In addition, the energy required for each compound to transition from one elastically ground state to the other are calculated. This energy is called energy barrier, and it depends on chemical species in the compound.

In this chapter, the structural parameters of monochalcogenide monolayers, and the correlation of the shape of the unit cell with atomic number are also discussed.

The consequence of all degeneracies mentioned for MMs and phosphorene is a four-fold degenerate ground state. This four-fold degenerate ground state leads to an order-disorder

structural phase transition. The effect of temperature on the structure of MMs and phosphorene is corroborated by Car-Parrinello molecular dynamics calculations.

## 4.2 Lattice parameters of phosphorene and MMs

As mentioned before, phosphorene has a rectangular primitive unit cell. The real space unit vectors of phosphorene in Cartesian coordinates are:

$$\vec{a}_1 = (4.628, 0, 0) \text{ \AA}, \quad \vec{a}_2 = (0, 3.365, 0) \text{ \AA} \quad (\text{Equation 33})$$

These results are obtained by DFT calculation with VASP code and PBE pseudo potential.

In addition, the reciprocal space unit cell is described by vectors  $\vec{b}_1$  and  $\vec{b}_2$ .

$$\vec{b}_1 = 2\pi \frac{\vec{a}_2 \times \vec{a}_3}{\vec{a}_1 \cdot (\vec{a}_2 \times \vec{a}_3)} = 2\pi \frac{|\vec{a}_2| \hat{j} \times \hat{k}}{|\vec{a}_1| \cdot |\vec{a}_2|} = \frac{2\pi}{|\vec{a}_1|} \hat{i} = 1.867 \text{ \AA} \hat{i} \quad (\text{Equation 34})$$

$$\vec{b}_2 = 2\pi \frac{\vec{a}_3 \times \vec{a}_1}{\vec{a}_2 \cdot (\vec{a}_3 \times \vec{a}_1)} = 2\pi \frac{|\vec{a}_1| \hat{k} \times \hat{i}}{|\vec{a}_1| \cdot |\vec{a}_2|} = \frac{2\pi}{|\vec{a}_2|} \hat{j} = 1.358 \text{ \AA} \hat{j} \quad (\text{Equation 35})$$

The primitive unit cell and lattice vectors of phosphorene are shown in Figure 9 from different views. Each primitive unit cell of phosphorene and MMs contains four atoms. The structure of phosphorene from the top view is hexagonal. In one direction, the structure forms an armchair pattern and from the other side it has a zigzag pattern. This anisotropy in the structure of phosphorene and MMs is the source of many interesting phenomena in these compounds. For instance, phosphorene is flexible along the armchair pattern and stiff along the zigzag direction. The thermal conductivity of phosphorene along the zigzag direction is 40% larger than that along the armchair direction [94-96].

The rectangular unit cell of phosphorene is also generic to all group IV-monochalcogenides

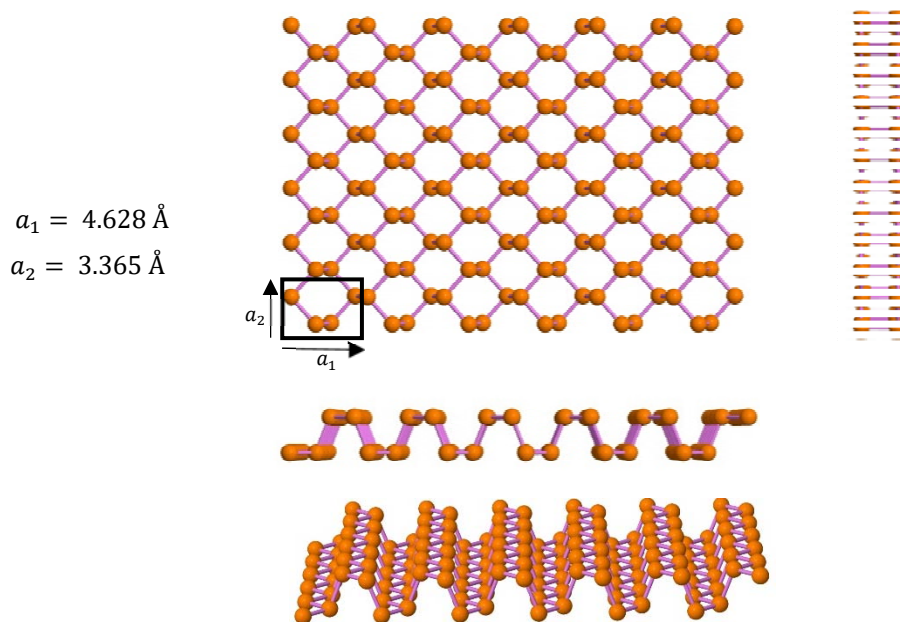


Figure 9. The structure of phosphorene from different views. A single unit cell and lattice vectors are also shown.

where each unit cell contains four atoms. However, the aspect ratio of the unit cell depends on atomic number, with lighter elements displaying the largest aspect ratio. The atomic structure of GeSe is illustrated in Figure 10a, and it is similar to that of phosphorene. The atomic structure of PbTe is shown in Figure 10b. Being heavier than GeSe, PbTe and other MMs with large atomic number have square unit cells.

The first step to study these materials is to find the lattice parameters and lattice vectors. Therefore, a series of DFT calculations with VASP code on 12 MMs were performed to determine the lattice parameters and basis vectors of SiS, SiSe, SiTe, GeS, GeSe, GeTe, SnS, SnSe, SnTe, PbS, PbSe, and PbTe. In these DFT calculations, both PBE and LDA pseudo-potentials were used. The results of these calculations along with the atomic numbers and melting points of bulk form of these compounds are summarized in Table 2 and 3.

In Tables 2 and 3,  $\frac{a_1}{a_2}$  is the aspect ratio of the primitive unit cell which shows the deviation

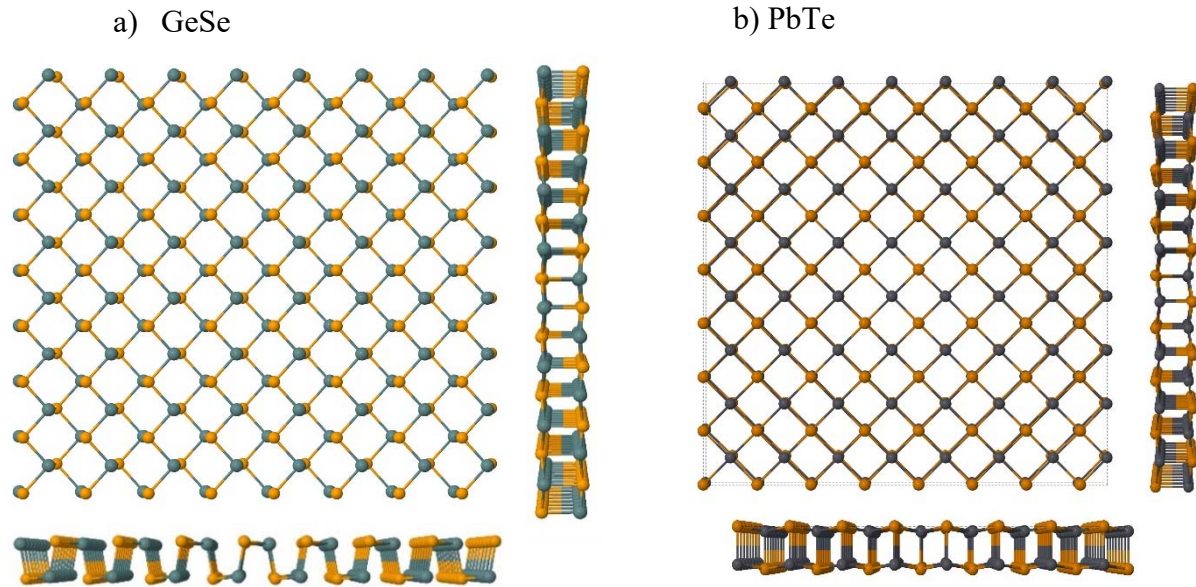


Figure 10. a) The atomic structure of GeSe from different views and b) the atomic structure of PbTe from different views.

Table 2. The lattice parameters of MMs using VASP code and PBE pseudo-potentials.

	$a_1$ (Å)	$a_2$ (Å)	Atomic number	$a_1/a_2$	Melting point of bulk (K) [97]
phosphorene	4.628	3.365	60	1.375	883
SiS	4.820	3.340	60	1.44	1173
SiSe	4.780	3.600	96	1.352	
SiTe	4.290	4.110	132	1.044	
GeS	4.337	3.739	96	1.16	888
GeSe	4.473	4.074	132	1.098	940
GeTe	4.411	4.231	168	1.043	998
SnS	4.329	4.157	132	1.041	1153
SnSe	4.702	4.401	168	1.068	1134
SnTe	4.681	4.586	204	1.021	1063
PbS	4.350	4.349	196	1.00	1391
PbSe	4.417	4.417	232	1.00	1351
PbTe	4.650	4.650	268	1.00	1197

of the unit cell from a square unit cell. Based on the calculated lattice constants, for all group IV monochalcogenide compounds, one can see that there is a correlation between atomic number of the compound and aspect ratio of the unit cell. Furthermore, additional calculations with SIESTA

Table 3. The lattice parameters of MMs using VASP code and LDA pseudo-potentials.

	$a_1$ (Å)	$a_2$ (Å)	Atomic number	$a_1/a_2$	Melting point of bulk (K) [97]
phosphorene			60		883
SiS	4.460	3.300	60	1.352	1173
SiSe	3.980	3.780	96	1.053	
SiTe	4.120	4.040	132	1.020	
GeS	3.960	3.720	96	1.065	888
GeSe	4.020	3.900	132	1.031	940
GeTe	4.200	4.140	168	1.014	998
SnS	4.040	4.000	132	1.010	1153
SnSe	4.20	4.200	168	1.000	1134
SnTe	4.440	4.440	204	1.000	1063
PbS	4.120	4.120	196	1.000	1391
PbSe	4.280	4.280	232	1.000	1351
PbTe	4.520	4.520	268	1.000	1197

code that include vdW correction are consistent with the results of LDA and PBE pseudo-potentials.

To illustrate this correlation better, Figure 11 shows the variation of the primitive unit cell aspect ratio versus the mean atomic number of the compound  $\bar{Z}$  where

$$\bar{Z} = \frac{1}{2}(Z_{IV} + Z_{VI}) \quad (\text{Equation 36})$$

These aspect ratios range from about 1.40 for the cases of phosphorene and silicon sulfide (with small atomic numbers) to 1.00 for heavier compounds such as PbTe and PbSe, which means as the atomic number increases the unit cell of the compound becomes closer to a square unit cell. Consequently, the unit cells of materials with large atomic number such as PbSe and PbTe have a square shape.

### 4.3 Degeneracy and energy barrier calculations in phosphorene and MMs

Graphene has a non-degenerate ground state; its structure does not change under a three-

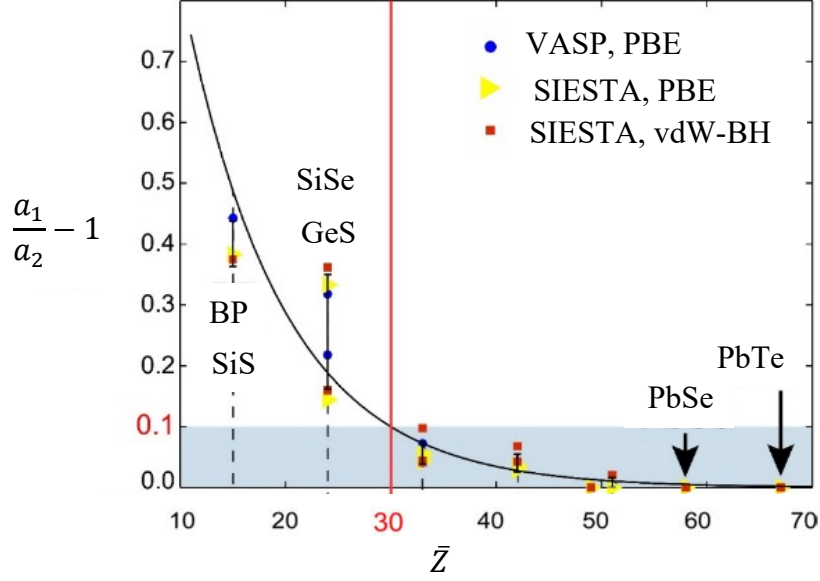


Figure 11. The correlation of the aspect ratio of rectangular unit cell with MMs mean atomic number.

fold rotation nor upon mirror reflections along any of three-fold axes. Figure 12 illustrates these transformations. This fact leads to non-degeneracy its the ground state and is one reason behind its structural stability. On the other hand, 2D materials with lower symmetries have degenerated structural ground states. For example, phosphorene and MMs have a  $Pnma$  structure with an orthorhombic unit cell. As shown in Figure 13, these structures will change upon mirror transformation or rotation about symmetric axes. This leads to a four-fold degeneracy. As illustrated in Figure 13, two of these degeneracies comes from exchange of lattice parameters along cell. Each unit two in-plane axes and the other two degeneracies come from the choice of atomic bonds in the unit cell consists of two atoms in upper sub-layer (shown in green) and two atoms in lower sublayers (shown in gray). In Figure 13a and 13c the larger lattice parameters are along the x-direction but the choice of atomic bonds is different. In Figure 13b and 13d the larger lattice vector is along the y-direction, with two different choices of atomic bonds.

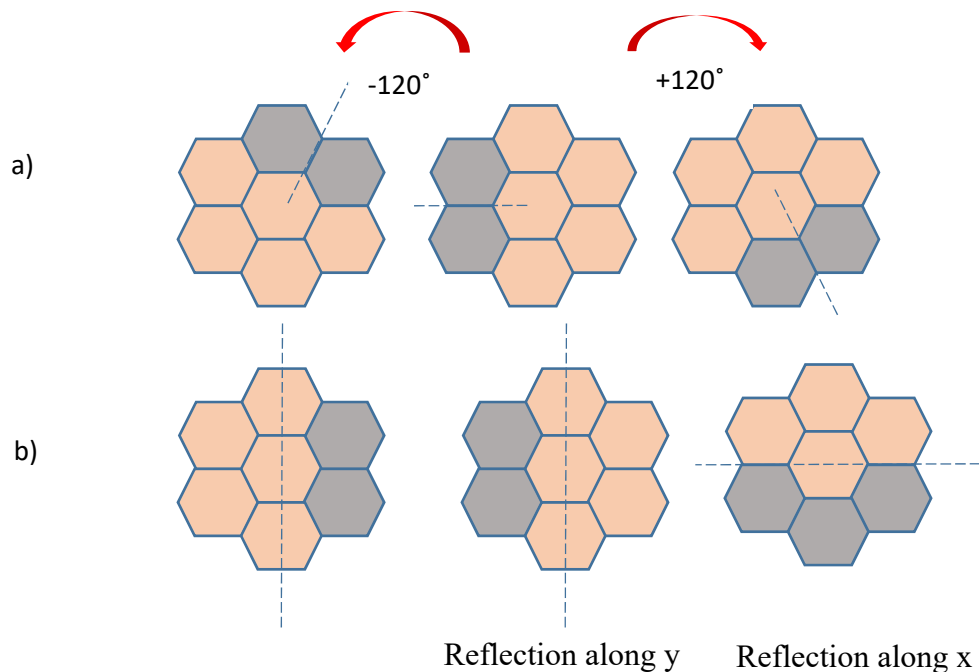


Figure 12. The structure of graphene remains unchanged upon a) three-fold rotations and b) reflection about symmetric axis.

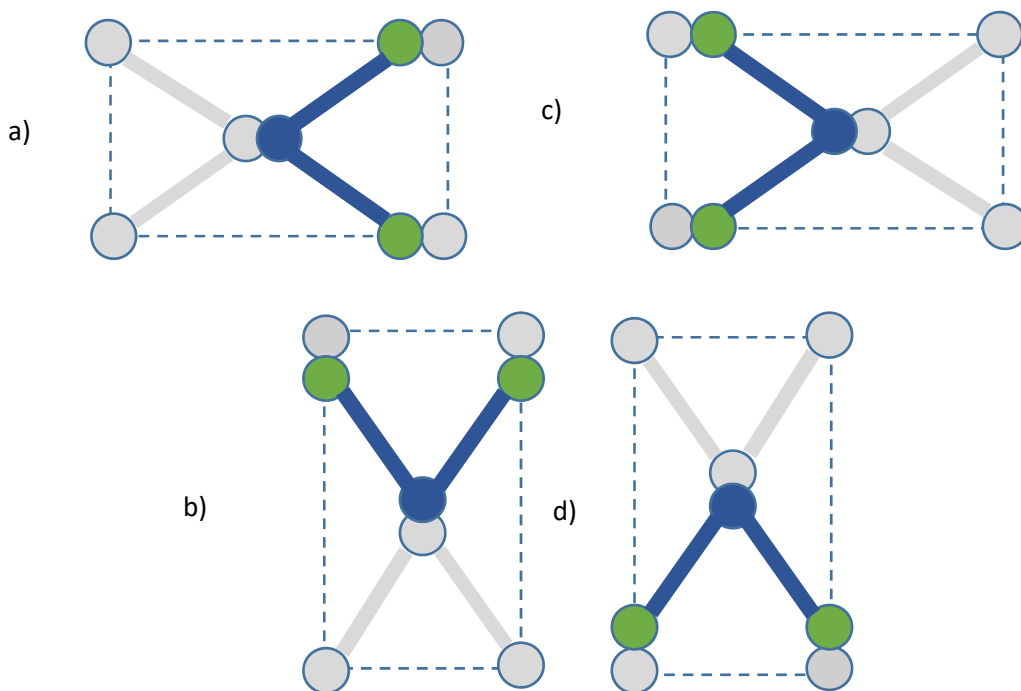


Figure 13. The structure of MM and phosphorene changes upon mirror transformation about symmetric axis.

#### 4.4 Energy landscape

The degeneracy in the ground state of MMs and phosphorene, which comes from the orientation of rectangular unit cell, can be investigated using elastic energy landscape [98]. The elastic energy landscape ( $E(a_1, a_2)$ ) is the energy of a unit cell at zero temperature as a function of the length and width of the rectangular unit cell. The range of lattice parameters are determined in a way that contains the two ground states of the material. For instance, for GeS, unit cell energy was calculated when  $a_1$  and  $a_2$  changes from 3.5 Å to 4.7 Å with small steps of 0.02 Å. This energy landscape is illustrated in Figure 14.

Figure 14 shows that the elastic energy landscape contains two minima which are labeled A and B. These two points are separated by an energy barrier, which is the energy that must be overcome to move from point A to point B in Figure 14. Point C on the Figure 14 is a saddle point that corresponds to the minimum energy of the structure when the two lattice constants are equal (square unit cell). The energy barrier is  $E_C - E_B$ . This energy is calculated for all the compounds and shown in Table 4 as  $E_C/k_B$  (K) per unit cell.

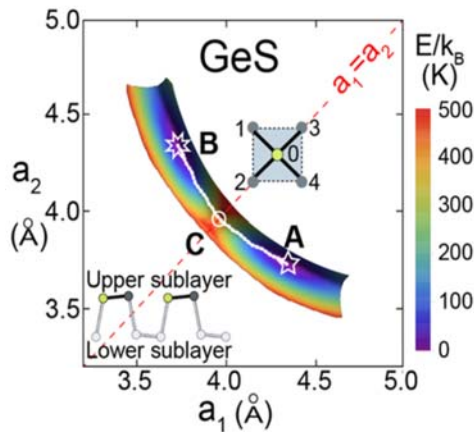


Figure 14. The energy landscape of GeS. Two ground states are labeled A and B. The barrier is of the order of 500 K



The energy barrier has a wide range, from 5159 K for phosphorene to 0 K for lead-based compounds, which implies wide tunability.

**Two groups of MMs based on their energy barrier:** Comparing the wide range of energy barrier with the experimental melting points shown in Table 4 allows the phosphorene and MMs to be categorized into two groups: (i) those compounds with melting points much smaller than the energy barrier i.e.  $E_c \geq k_B T_m$  such as phosphorene and SiS; and, (ii) those with an energy barrier less than their melting point i.e.  $E_c \leq k_B T_m$  such as GeTe.

The value of energy barrier plays a significant role in the structure of phosphorene and MM compounds at finite temperature. Most of theoretical studies on phosphorene and MMs are performed at zero temperature and under the assumption that the atomic structure does not change at finite temperature before the melting point. However, in the case that the ground state is degenerate, one can expect that materials change structurally at finite temperature and this is the main point of the present dissertation.

Table 4. Energy barrier of MMs using VASP code.

	Atomic number	$a_1/a_2$	$E_c/k_B$ (K)	Melting point of bulk (K) [97]
phosphorene	60		$5159 \pm 75$	883
SiS	60	1.352	$3536 \pm 462$	1173
SiSe	96	1.053	$730 \pm 446$	
GeS	96	1.020	$653 \pm 221$	888
GeSe	132	1.065	$220 \pm 76$	940
SiTe	132	1.031	$154 \pm 24$	
GeTe	168	1.014	$95 \pm 9$	998
SnS	132	1.010	$63 \pm 0$	1153
SnSe	168	1.000	$87 \pm 79$	1134
SnTe	204	1.000	$10 \pm 14$	1063
PbS	196	1.000	0	1391
PbSe	232	1.000	0	1351
PbTe	268	1.000	0	1197

The energy barrier of phosphorene as calculated in this study is 5100 K which is thermally driven much higher than its melting point. As a result of this huge barrier, one cannot expect to see 2D structural phase transition in phosphorene. However, those materials (GeSe, GeS, SnSe, SnS) which have energy barriers smaller than melting points will undergo a 2D phase transition. To see the effect of these structural changes on properties of MMs, it is essential to investigate the effect of temperature as a cause of structure changes on material properties. Chapter Five of this dissertation focuses mainly on the effect of temperature and consequently structural changes on properties of MMs.

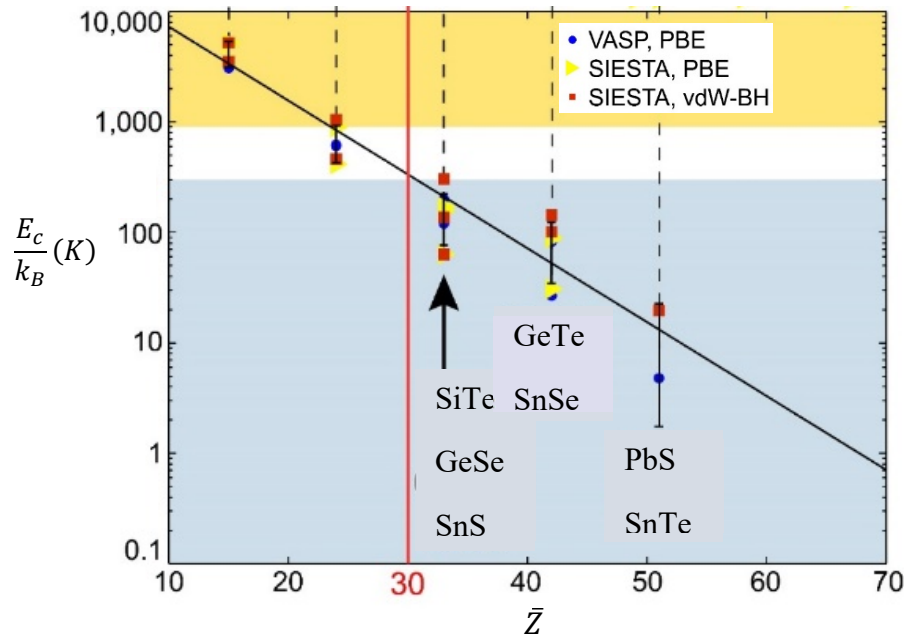


Figure 15. The logarithm of the energy barrier for different MMs unveils exponential dependence of the energy barrier with the mean atomic number.

#### 4.5 More on the second source of degeneracy

The second source of degeneracy comes from the choice of bonding in the unit cell, which can be explained using Figure 16. The structure of MMs has two sublayers. In Figure 16, the upper

sublayer is shown in darker color. A single rectangular unit cell of the structure is shown within black dashed lines. The atom labeled 0 shown in bright color has four different choices of combinations to create bonds with its neighbors. In structure  $A_1$ , atom 0 is bonded to atom 1 and 2 while in structure  $A_2$  it is bonded to atoms 3 and 4. In the same pattern in configuration  $B_1$ , atom 0 is bonded to atoms 1 and 3 and in  $B_2$ , 0 is bonded to 2 and 4. Each of these atoms is also bonded to an atom in the lower sublayer. The lower sublayer bonds follow the trend described for the upper sublayer, leading to four combinations in total.

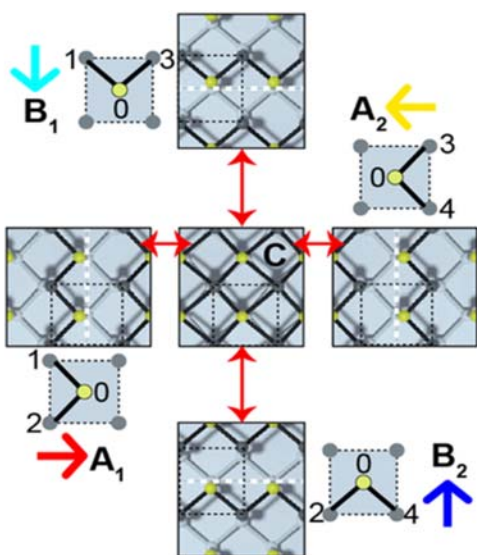


Figure 16. Atomic decoration of four degenerate ground state on MMs.

#### 4.6 Effect of temperature on the atomic structure by MD calculation

As a first attempt to see the effect of temperature on the structure of phosphorene and MMs, a series of Car-Parrinello molecular calculations with the SIESTA code were performed at  $T = 30$  K, 300 K, and 100 K. These calculations were run for 1000 fs on a periodic supercell containing 576 atoms within NPT ensemble. Periodic images have a separation of  $20 \text{ \AA}$ . In these calculations, a total of 500 fs time is required for the structure to equilibrate. Initially, all unit cells have atomic

decoration of  $A_1$  as shown in Figure 16. These calculations already validate categorizing MMs and phosphorene into two groups based on the value of energy barrier and melting point that were discussed earlier. Figure 17 shows snapshots of the MD calculation on phosphorene and different MMs at 300 K. For a better understanding of the snapshots of MMs, only the upper sublayer is depicted. These snapshots are taken after 500 fs and show what happens at room temperature to these materials. In Figures 17a and 17b phosphorene and SiSe at  $T = 300$  K show no major structural changes. This is in agreement with the fact that phosphorene and SiSe have a very high-energy barrier. The snapshot of GeS in Figure 17c shows few bond reassignments. While in the initial condition all unit cell followed  $A_1$  configuration, two bond reassignments occurred which are shown in the figure with arrows in different directions than  $A_1$ . Based on Table 4, the energy barrier of GeS is 653 K, still higher than 300 K.

However, when the simulation temperature is higher than the energy barrier, bond reassignment happens which leads to disorder in the structure of the material: Figure 17 d-f shows the MD snapshot of GeSe, SnS, and SnSe, respectively, for which  $E_c < 300$  K. In these snapshots, the number of bond reassignments increases, which is consistent with their energy barrier being smaller than the simulation temperature. Orange lines correspond to the initial configuration of atomic bonds.

The behavior of these material at higher temperature can be discussed by looking at snapshots of MD calculations at  $T = 1000$  K. Figure 18a shows phosphorene retains its  $Pnma$  structure at 1000 K.

#### **4.7 Evolution of average lattice parameters $a_1$ and $a_2$ with temperature**

Figures 17 and 18 provide visual evidence of order-disorder transition of some MMs.

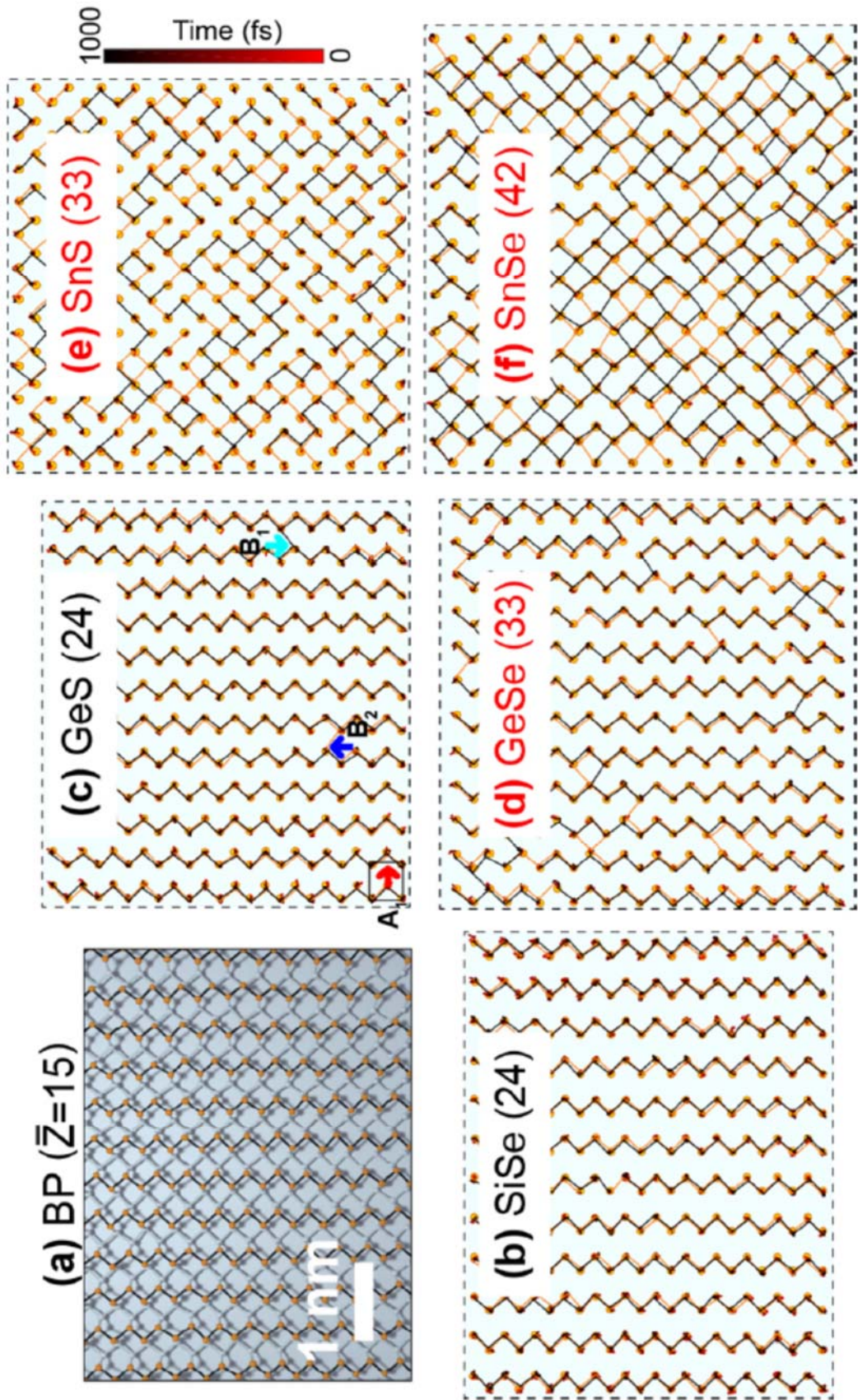


Figure 17. Snapshot of MD results at 300 K for different materials. Materials labeled in red have an energy barrier smaller than 300 K and undergo bond reassignments.

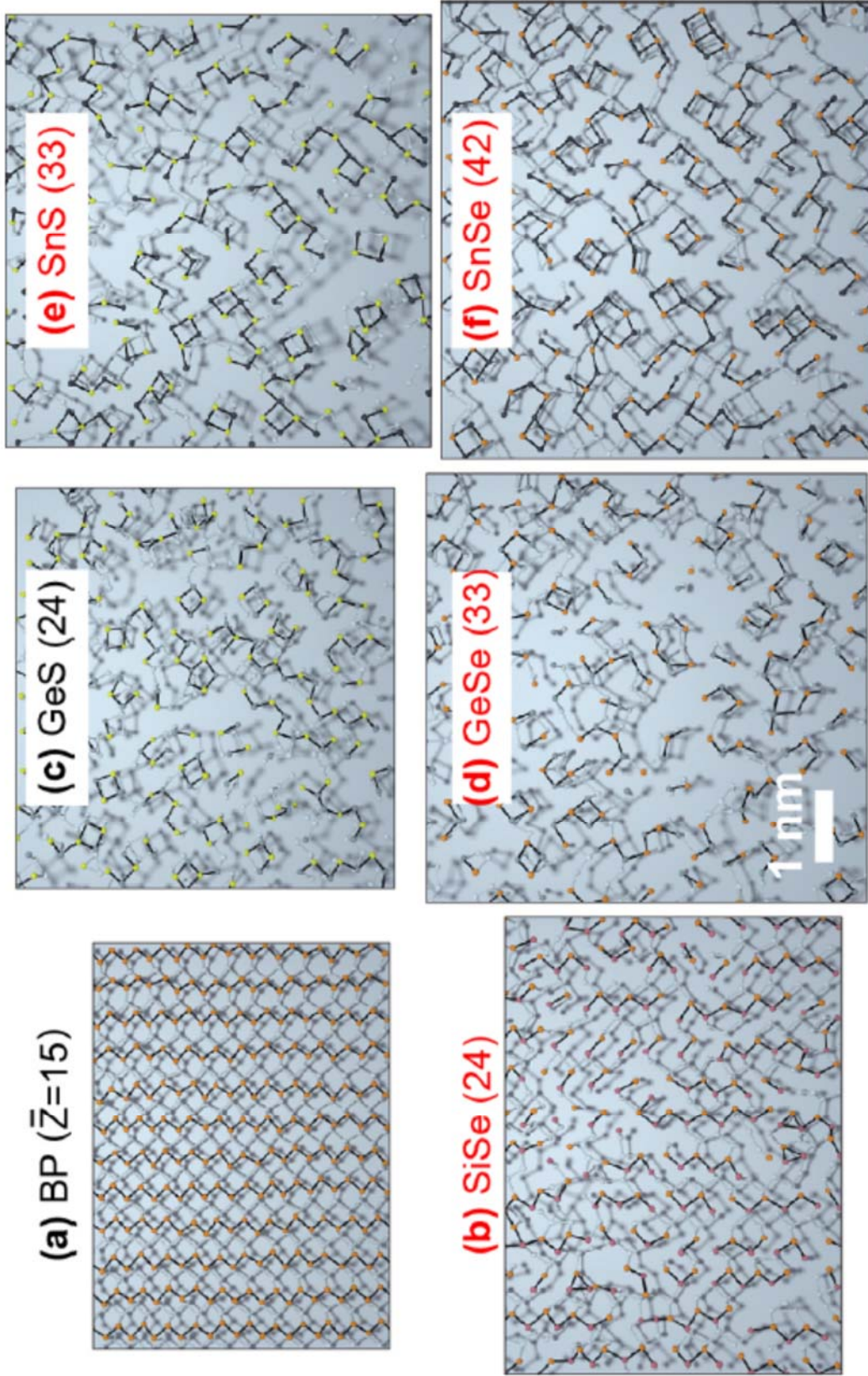


Figure 18. Snapshot of MD results at 1000 K for different materials, showing a melting of most materials except phosphorene (BP).

However, the evolution of average lattice parameters of the 12x12 supercell with temperature provides initial credence for such a transition. As discussed before, the transition starts by bond reassignment of nearest neighbors. The temperature increases and becomes closer to the value of  $E_c/k_B$  per unit cell as more bond reassignments between nearest neighbors occurs, leading to a macroscopic effect on the value of average lattice parameters, by increasing the smaller lattice parameter and decreasing the larger one. Finally, at a macroscopic level and at a temperature above  $E_c/k_B$ , the average of the two lattice parameters becomes equal, which signals the occurrence of a structural phase transition. Although a full description of the transition is reserved to Chapter Five, it is important to begin making a case for it. The value of average lattice vectors and the ratio of  $\frac{a_1}{a_2}$  at temperatures of 0 K, 30 K, 300 K, and 1000 K are shown in Table 5, for that purpose. Based on these results, phosphorene and SiSe retain a ratio of lattice parameters  $\frac{a_1}{a_2} > 1$  in all four sampled temperatures, which means their rectangular unit cell does not alter up to melting point. This is consistent with their high value of  $E_c$ . Phosphorene and SiSe maintain their two-dimensional *Pnma* structure up to 1000 K.

In case of PbS, the ratio of  $\frac{a_1}{a_2}$  is equal to one for all the four sampled temperatures, which is consistent with the value of  $E_c = 0$  previously mentioned in Table 5. In all other cases, bond reassignment at finite temperature happens, which is a sign of an order-disorder transition before the melting point [99]. In fact, GeS shows a significant reduction of  $\frac{a_1}{a_2}$  ratio from  $1.156 \pm 0.106$  to  $1.048 \pm 0.541$  between  $T = 300$  K and  $T = 1000$  K. GeSe also shows a drastic change of  $\frac{a_1}{a_2}$ , from  $1.084 \pm 0.116$  at  $T = 300$  K, down to  $1.016 \pm 0.541$  at  $T = 1000$  K. These are evidence showing order-disorder transition happens for these materials between  $T = 300$  K and  $T = 1000$  K

and agrees with their value of  $E_c = 653 \pm 221$  and  $E_c = 220 \pm 76$  for GeS and GeSe, respectively.

Along similar lines, the lattice ratio of SnSe, SnTe, and GeTe has a sudden change between 30 K and 300 K which may imply that SnSe, SnTe, and GeTe will have an order-disorder transition between 30 K and 300 K. According to Table 4, SnS has  $E_c = 63 \pm 0$ , which implies that a drastic change of  $a_1/a_2$  ratio should happen between 30 K and 300 K as a result of order-disorder transition. Accordingly, Table 5 shows a decrease of  $a_1/a_2$  ratio from  $1.041 \pm 0.027$  to  $1.003 \pm 0.096$  from 30 K to 300 K.

Table 5. Average lattice parameters for phosphorene and MMs at four temperatures.

T(K)	$a_1$ (Å)	$a_2$ (Å)	$a_1/a_2$	$a_1$ (Å)	$a_2$ (Å)	$a_1/a_2$
	phosphorene			SiSe		
0	$4.628 \pm 0.000$	$3.365 \pm 0.000$	$1.375 \pm 0.000$	$5.039 \pm 0.000$	$3.728 \pm 0.000$	$1.352 \pm 0.000$
30	$4.625 \pm 0.050$	$3.364 \pm 0.033$	$1.375 \pm 0.028$	$5.029 \pm 0.058$	$3.733 \pm 0.077$	$1.347 \pm 0.042$
300	$4.628 \pm 0.181$	$3.368 \pm 0.103$	$1.374 \pm 0.096$	$5.054 \pm 0.187$	$3.748 \pm 0.272$	$1.348 \pm 0.140$
1000	$4.632 \pm 0.388$	$3.384 \pm 0.207$	$1.369 \pm 0.198$	$5.090 \pm 1.298$	$3.861 \pm 1.302$	$1.318 \pm 0.780$
	GeS			GeSe		
0	$4.337 \pm 0.000$	$3.739 \pm 0.000$	$1.160 \pm 0.000$	$4.473 \pm 0.000$	$4.074 \pm 0.000$	$1.098 \pm 0.000$
30	$4.338 \pm 0.069$	$3.744 \pm 0.044$	$1.159 \pm 0.032$	$4.475 \pm 0.071$	$4.073 \pm 0.051$	$1.099 \pm 0.031$
300	$4.351 \pm 0.228$	$3.764 \pm 0.148$	$1.156 \pm 0.106$	$4.474 \pm 0.266$	$4.128 \pm 0.197$	$1.084 \pm 0.116$
1000	$4.478 \pm 1.304$	$4.271 \pm 0.960$	$1.048 \pm 0.541$	$4.942 \pm 1.349$	$5.019 \pm 1.386$	$1.016 \pm 0.541$
	GeTe			SnS		
0	$4.411 \pm 0.000$	$4.231 \pm 0.000$	$1.043 \pm 0.000$	$4.329 \pm 0.000$	$4.628 \pm 0.000$	$1.041 \pm 0.000$
30	$4.414 \pm 0.052$	$4.230 \pm 0.055$	$1.043 \pm 0.026$	$4.330 \pm 0.061$	$4.628 \pm 0.050$	$1.041 \pm 0.027$
300	$4.408 \pm 0.199$	$4.266 \pm 0.175$	$1.033 \pm 0.089$	$4.258 \pm 0.218$	$4.628 \pm 0.190$	$1.003 \pm 0.096$
1000	$4.479 \pm 0.720$	$4.415 \pm 0.645$	$1.014 \pm 0.311$	$4.837 \pm 1.109$	$4.628 \pm 0.171$	$1.028 \pm 0.492$
	SnSe			SnTe		
0	$4.702 \pm 0.000$	$4.401 \pm 0.000$	$1.068 \pm 0.000$	$4.681 \pm 0.000$	$4.157 \pm 0.000$	$1.021 \pm 0.000$
30	$4.695 \pm 0.075$	$4.406 \pm 0.060$	$1.066 \pm 0.032$	$4.686 \pm 0.060$	$4.159 \pm 0.057$	$1.022 \pm 0.026$
300	$4.687 \pm 0.282$	$4.468 \pm 0.254$	$1.049 \pm 0.123$	$4.630 \pm 0.219$	$4.245 \pm 0.220$	$1.008 \pm 0.094$
1000	$4.826 \pm 0.595$	$4.585 \pm 0.474$	$1.052 \pm 0.238$	$4.908 \pm 0.875$	$4.704 \pm 0.854$	$1.026 \pm 0.366$
	PbS					
0	$4.350 \pm 0.000$	$4.349 \pm 0.000$	$1.000 \pm 0.000$			
30	$4.355 \pm 0.049$	$4.354 \pm 0.044$	$1.000 \pm 0.021$			
300	$4.372 \pm 0.179$	$4.371 \pm 0.174$	$1.000 \pm 0.081$			
1000	$4.416 \pm 0.397$	$4.427 \pm 0.375$	$1.002 \pm 0.175$			



**Thermal evolution of the total energy:** Table 5 builds general evidence of 2D transitions in MMs. Signatures of this transition can also be observed in the energy behavior with temperature. However, finding the evolution of specific heat by temperature requires MD calculations at intermediate temperatures. For this reason, extra MD calculations are performed on GeS and GeSe. These MD calculations were performed with SIESTA package with temperature ranging from 0 K to 1000 K with steps of 50 K within the NPT ensemble, and P set to standard atmospheric pressure. For these MD calculation, an 8x8 supercell (256 atoms) was chosen.  $E(T)$  is the total energy of the structure which is achieved by averaging over 500-1000 fs of MD calculations.  $E(T)$  consists of both kinetic and potential energy terms:

$$E(T) = U(T) + K(T), \quad (\text{Equation 37})$$

where  $E(T)$  is the total energy as a function of temperature and  $U$  and  $K$  are potential and kinetic energy, respectively. Based on the equipartition theorem, the kinetic energy linearly depends on temperature. Therefore, one can write the potential energy as:

$$U(T) = E(T) - \alpha T \quad (\text{Equation 38})$$

where  $\alpha$  is a proportional constant.

The evolution of the potential energy of GeSe and GeS are shown in Figure 19. By looking at the trend of the potential energy versus temperature, it is seen that the rate of change of the potential energy reduces around 510 K for GeS and 380 K for GeSe. These are further evidence of phase transition in these materials. This concept is more apparent by looking at the evolution of the specific heat (derivative of total energy over temperature) at constant pressure.

$$c_p = \frac{d(E(T))}{dT} = \frac{d(U(T))}{dT} + \alpha \quad (\text{Equation 39})$$

which is illustrated in Figure 20.

Figure 20 shows that there are two sudden changes in the specific heat of both GeS and GeSe. One of these sudden changes is related to the melting point, around 900 K. The other sudden change corresponds to the 2D phase transition of these materials, which is being introduced in this dissertation. The sudden change is around 510 K for GeS and 380 K for GeSe. These temperatures

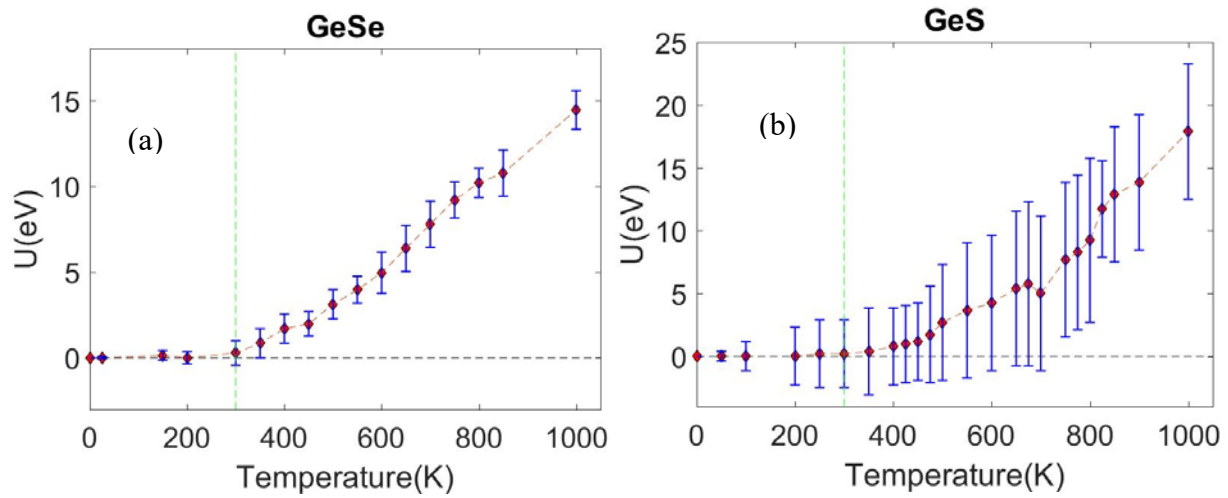


Figure 19. The evolution of internal potential energy  $U$  of a) GeS and b) GeSe with temperature.

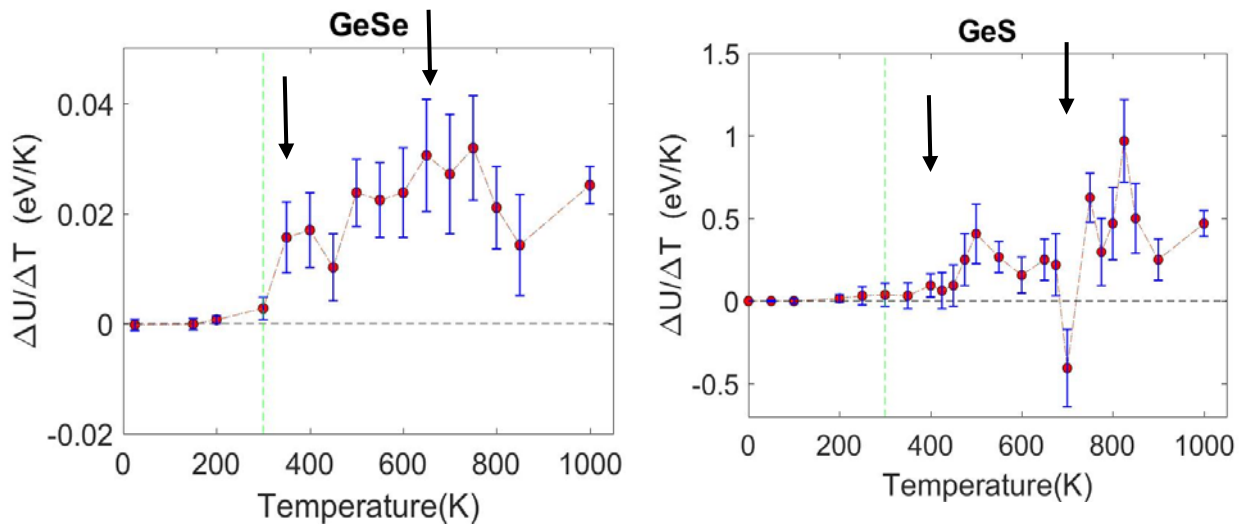


Figure 20. The evolution of the rate of the change of internal energy of a) GeS and b) GeSe with temperature.

are in agreement with previously mentioned results of order-disorder transition temperatures in Table 4 and Figures 15 and 16.

**Aspect ratio of the unit cell:** Another sign of transition in these materials is the change in the aspect ratio of the rectangular unit cell. That means the rectangular unit cell of these materials becomes a square at temperatures larger than  $E_c$ , as demonstrated in Figure 21. The ratio of  $\frac{a_1}{a_2}$  is an order parameter which can be used to determine the structural transition. A sudden change of this order parameter at a small temperature interval is a sign of such transition. The change of this order parameter over temperature can be calculated using Equation 40.

$$\frac{\Delta(a_1/a_2)}{\Delta T} \quad (\text{Equation 40})$$

A sudden change of this rate at temperatures close to  $E_c$  for GeS and GeSe is shown in Figure 21. To be consistent with showing MD results at 300 K and 1000 K in Figures 17 and 18, the trajectories of GeS and GeSe on an 8x8 super-cell are shown in Figures 22 and 23. The upper sublayer of the MMs has a zigzag pattern at zero temperature. However, at finite temperature, the zigzag pattern changes because of reassignment of atomic bonds between nearest neighbors. These bond reassignments are shown in Figures 22 and 23 with arrows. Figure 22 is snapshots of the atomic temperature at 100 K, 200 K, and 300 K. At these temperatures, the bond reassignments are minimum. However, as temperature increases, the number of sites for which bond reassignment occurs increases until the crystal becomes completely disordered as illustrated in Figure 23. These results are generic for all MMs.

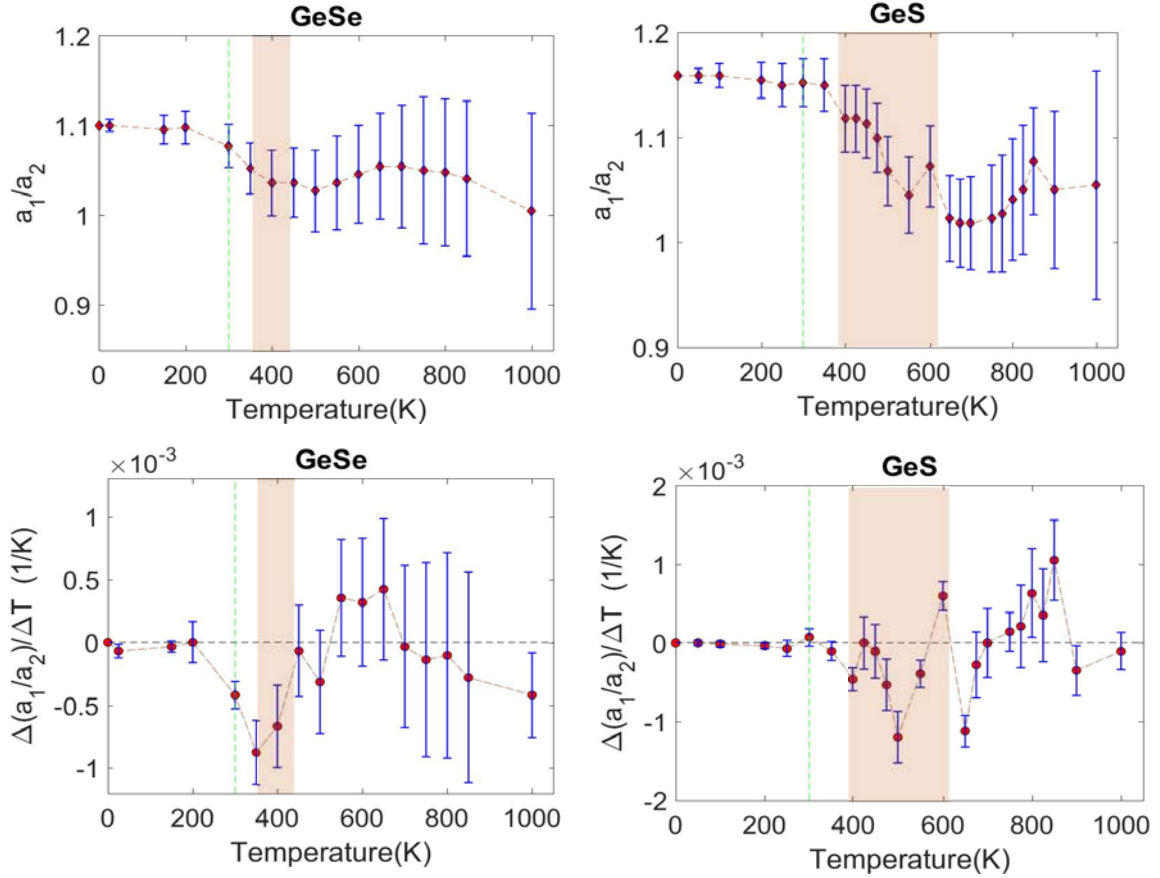


Figure 19. The evolution of the ratio of the two lattice parameters by temperature (top) and its rate of change (bottom).

#### 4.8 Discussion and summary

Graphene has a degenerate ground state which makes it a stable material. However, most two-dimensional materials have lower symmetric crystalline structures which adds degeneracy to their structural ground state. Along these lines, MMs and phosphorene have a four-fold degenerate ground state. Two of which can be obtained by exchange of the two lattice parameters and two come from the position of atoms in the unit cell. The required energy to move from one ground state to the other is called the energy barrier. This value can be normalized by Boltzmann's constant which will have a Kelvin unit per unit cell. In this chapter, phosphorene and MMs were categorized into two groups based on their energy barrier: i) the energy barriers of phosphorene

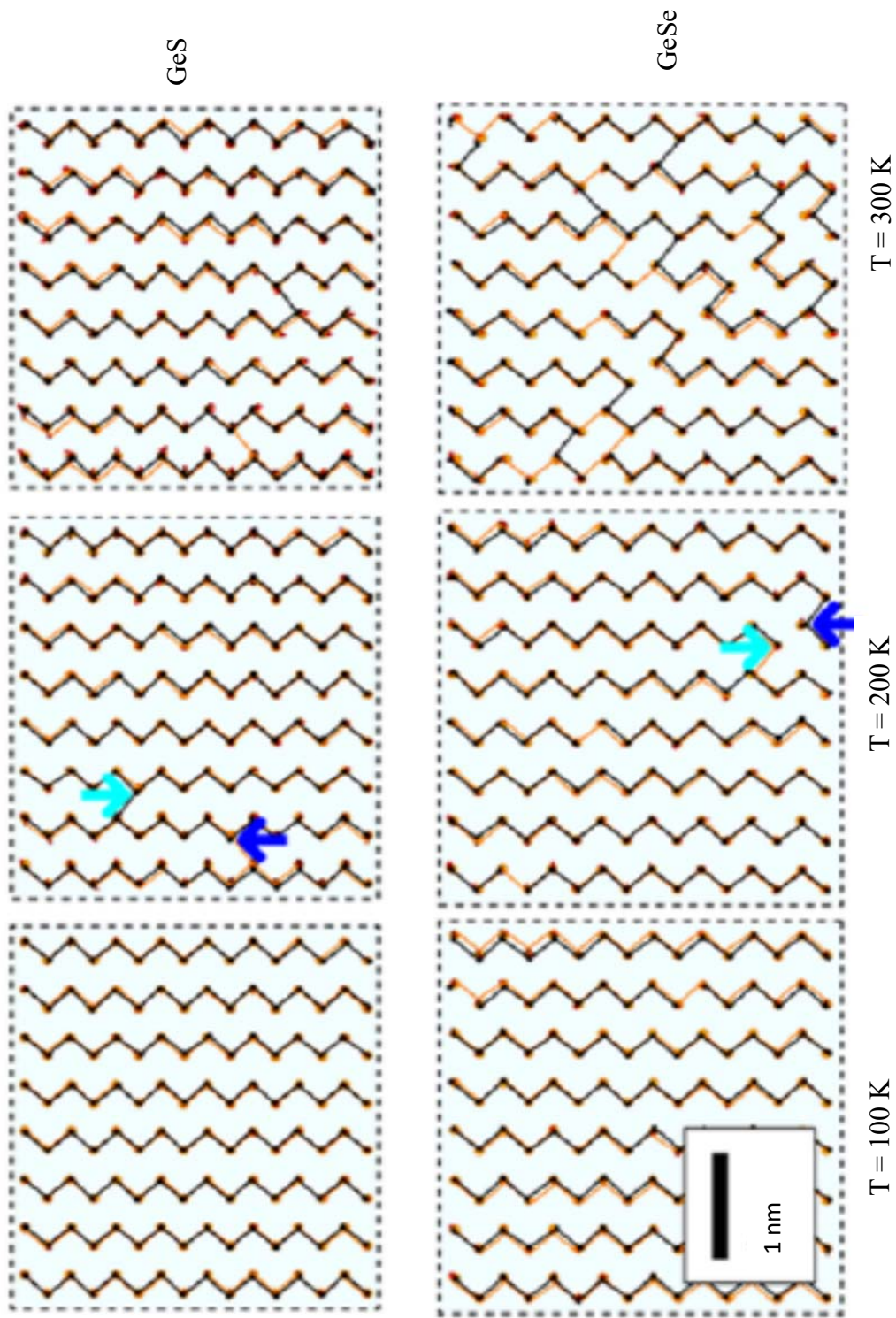


Figure 20. Snapshot of atomic structure at 100 K, 200 K, and 300 K for GeS (top) and GeSe (bottom).

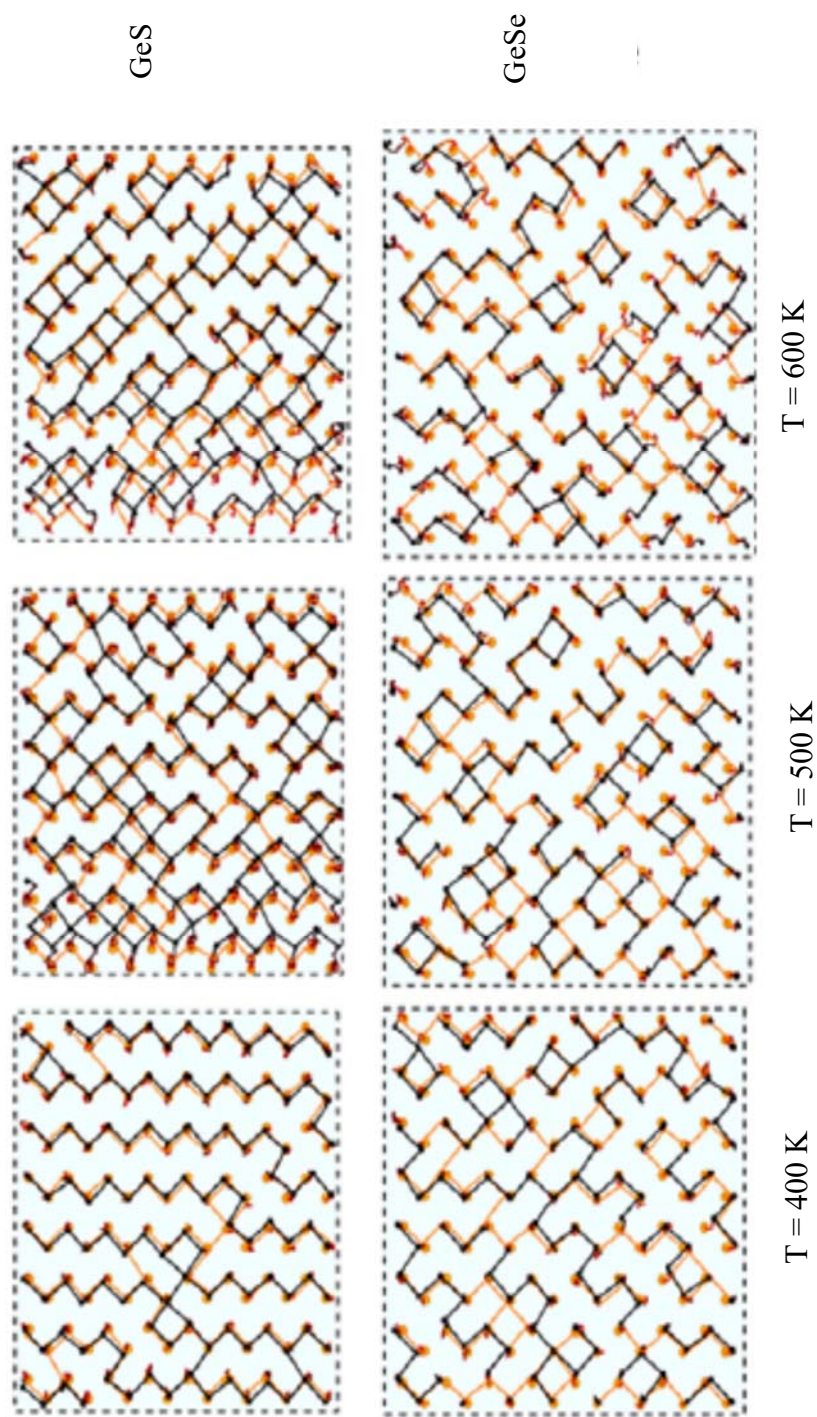


Figure 21 . Snapshot of atomic structure at 400 K, 500 K, and 600 K for GeS (top) and GeSe (bottom).

and SiS are much higher than their melting points; and ii) GeSe, GeSe, SnSe, SnS and Pb compounds have energy barriers much less than their melting points.

The energy landscape of a single unit cell of GeS as a function of the two lattice parameters was plotted and discussed. This energy landscape shows two minima which corresponds to the two ground states of the material. In addition, the energy barrier was calculated by comparing the ground state energy with the minimum energy of the unit cell when the two lattice parameters are equal. The energy barrier for phosphorene and 12 compounds of MMs were calculated and tabulated.

The crystal structure of the first group remains intact by increasing the temperature until it reaches the melting point. However, the second group undergoes 2D transitions in the crystalline structure before the melting point, signified by abrupt change of  $a_1/a_2$  into unity.

Various evidence of this 2D transition was investigated and is listed below.

- Snapshot of MD calculations at temperatures well below the melting point show visual evidence of disorder in the crystalline structure of the second group by bond reassignments.
- The evolution of the specific heat of these materials by temperature shows a significant change at a critical temperature close to the barrier energy.
  - The average of the two lattice parameters becomes equal at critical temperature which means the unit cell changes from a rectangular unit cell to a square one.

## 5 Chapter Five: Structural phase transition in group IV monochalcogenide monolayers and bilayers

### 5.1 Introduction: phase transitions in crystalline materials

Phase transitions are very important in physics. Very exciting phenomena such as multiferroicity, ferromagnetism, ferroelectricity, superconductivity, ferroelectricity, liquid crystals and magnetoresistance are directly related to phase transitions. Different types of phase transitions exist in crystalline materials:

- Structural phase transitions
- Metal-insulator phase transitions
- Superconducting-normal phase transitions
- Superfluid-normal phase transitions
- Magnetic phase transitions
- Quantum phase transitions, which are non-thermally driven.

In the previous chapter, the four-fold degeneracy in the ground state of monochalcogenide monolayers was introduced. The degeneracy of the structural ground state leads to a structural two-dimensional order-disorder phase transition in these materials. The ferroelectric properties [74, 100] observed in these materials are the consequence of their structural degeneracies [74].

In this chapter, SnSe and GeSe monolayers and bilayers are the focus of investigation: more evidence of phase transitions by means of new structural order parameters are given, along with effect of the 2D phase transition on their optical, electronic, and piezoelectric properties. Most of the results are based on Car-Parinello MD calculations with SIESTA package on the NPT ensemble.



## 5.2 Car-Parrinello MD calculations

According to Figure 15, the structural phase transition in MMs happens at a material dependent critical temperature,  $T_c$ . Therefore, it is essential to investigate the structure of these materials at different temperatures before the melting point. For this purpose, among different MMs, SnSe and GeSe were chosen. The reason for this selection is the fact that the value of  $T_c$  for these materials is close to room temperature. In addition to monolayers of SnSe and GeSe, the same investigation was performed on AB bilayers of SnSe and GeSe which are anti-ferromagnetically coupled. The sample size of MD calculations for monolayer materials contained a supercell with 256 atoms (8x8 unit cell) and the bilayer materials were built by putting two layers of single layer material on an AB stacking configuration. These, MD calculations were run for 20,000 steps by Professor Barraza-Lopez, with a step size of 1.5 fs. This leads to a total 30 ps simulation of the structures. MD calculations were performed with a 25 K resolution.

Thermal equilibrium requires obtaining thermal averages which is ranging from 1000 fs to 5000 fs. Figures 24 and 25 show the change of Kohn-Sham energy versus time at 200 K, 300 K, and 425 K for SnSe and GeSe monolayers. Thermal fluctuations are also depicted in Figures 24 and 25.

## 5.3 Transition temperature from MD calculations.

**New structural order parameters:** In this section, the transition temperature,  $T_c$ , of monolayers of SnSe and GeSe is determined from the structural evolution in MD calculations. Sudden changes in order parameters show the transition temperature and the nature of the transition. These order parameters are:

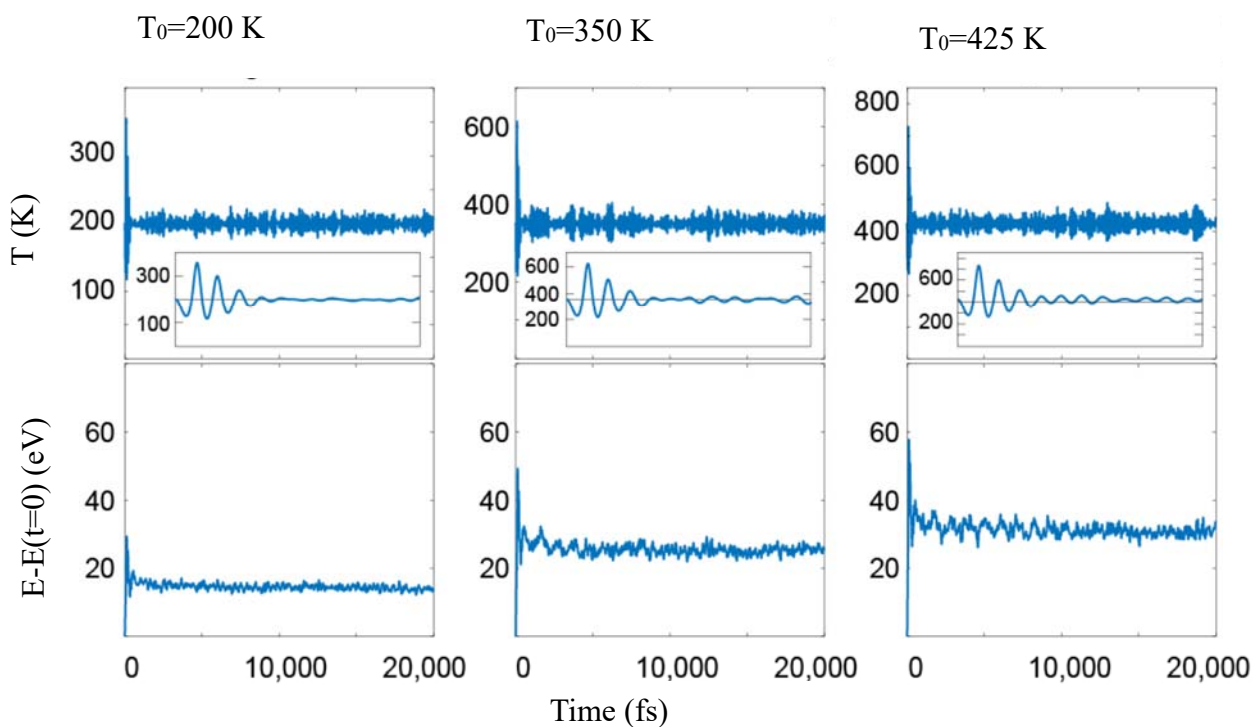


Figure 24. Time evolution instantaneous temperature and energy of the structure (GeSe ML).

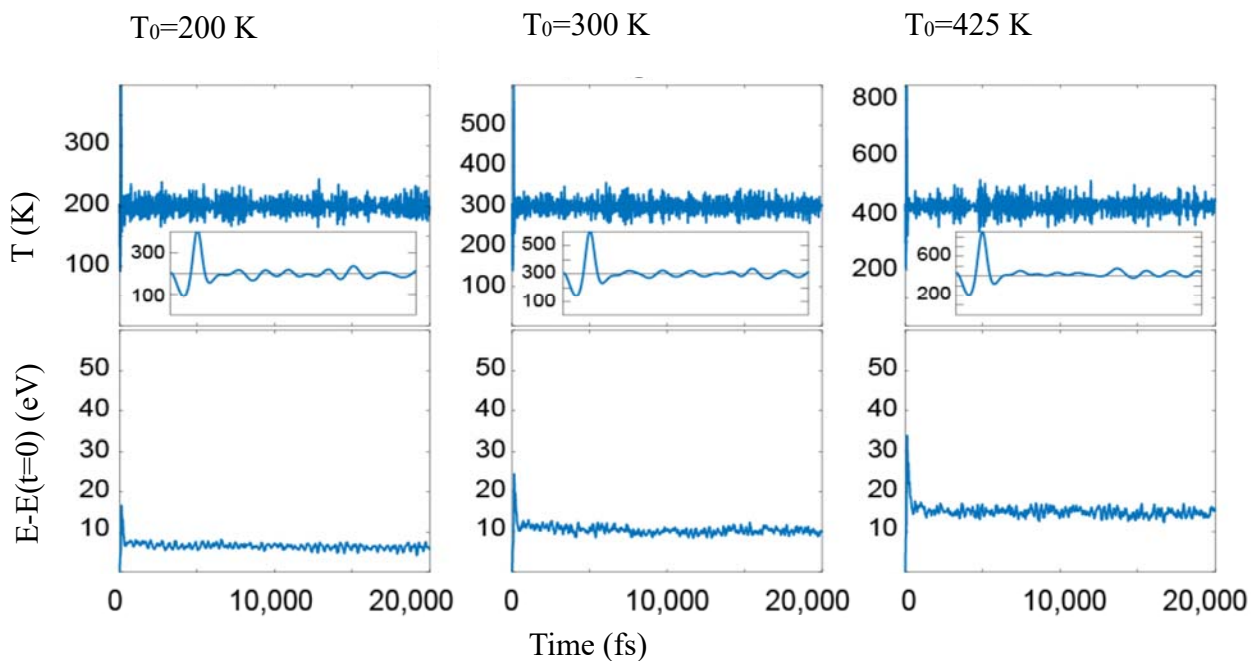


Figure 25. Time evolution instantaneous temperature and energy of the structure (SnSe ML).

- 1- The average of two in-plane lattice parameters of the materials. Since a sign of the structural transition is a change from a rectangular unit cell to a square one, the evolution of the two lattice parameters can show the transition temperature. The lattice parameters  $a_1$  and  $a_2$  are obtained by finding the average of four distances between similar atoms of two neighbor unit cells on the entire supercell, as shown in Figure 26.
- 2- Interatomic distances up to the third nearest neighbor,  $d_1$ ,  $d_2$ , and  $d_3$ , shown in Figure 26. One of the signatures of structural transition of these materials is when the distance between the second and third nearest neighbors becomes identical.
- 3- The other order parameters are related to bond angles of the structure.  $\alpha_1$  is the angle between a given atom and its third nearest neighbors;  $\alpha_2$  is the angle between second and third nearest neighbors; and,  $\alpha_3$  represents the angle between an atom and its second nearest neighbors. These angles are illustrated in Figure 26 too.

**Evolution of order parameters with temperature:** Figure 27 shows the values of order parameters as a function of time in monolayer GeSe at 200 K, 300 K, and 425 K, while Figure 28 illustrates the evolution of these order parameters as a function of time for GeSe bilayers at 200 K, 350 K and 450 K.

In Figures 27 and 28, the two lattice parameters  $a_1$  and  $a_2$  remain almost constant at  $T = 30$  K and  $a_2$  is smaller than  $a_1$  in all time steps of the simulation. In addition, the order of all other parameters remains constant, that means in the entire MD steps  $d_3 > d_2 > d_1$  and  $\alpha_3 > \alpha_2 > \alpha_1$ . This fact is generic for a bilayer at low temperature and suggests that there are no structural changes at low temperature for a monolayer and a bilayer of GeSe. However, at an intermediate temperature, 300 K for GeSe monolayer and 350 K for GeSe bilayer, the order parameters start to fluctuate and become equal on average.

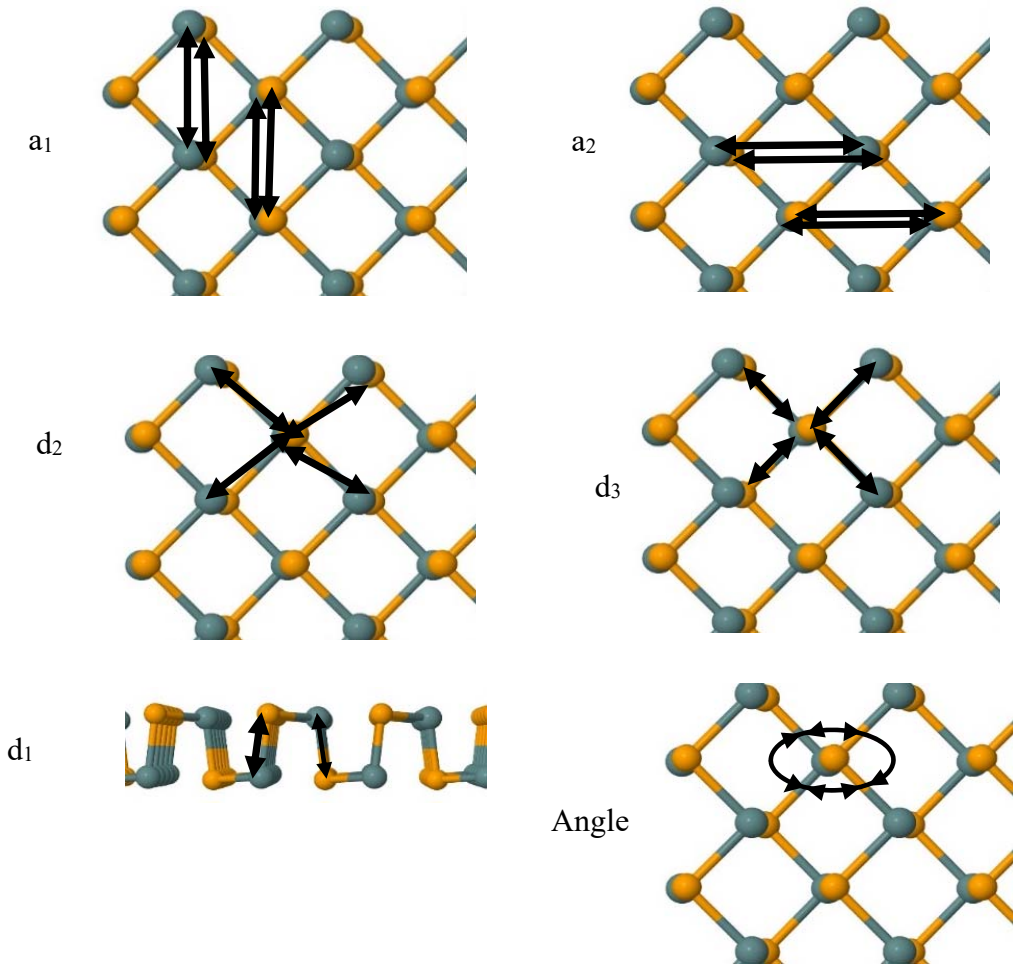


Figure 26. Structural order parameters.  $a_1$   $a_2$  are lattice parameters,  $d_1$ ,  $d_2$  and  $d_3$  are the first, second, and third nearest neighbor distances.

However, the value of  $d_1$  remains unchanged, even at a higher temperature of 425 K for both monolayer and bilayer of GeSe throughout the entire simulation. Physically,  $d_1 = \text{constant}$  means the distance between two upper and lower sublayers of the material remains constant, which allows this to be called a two-dimensional phase transition. This fact is crucial for the understanding the nature of this phase transition. The evolution of order parameters for SnSe monolayer at 100 K, 175 K, and 300 K is illustrated in Figure 29 and in Figure 30 for SnSe bilayers at 100 K, 200 K, and 350 K. The trend of the order parameters of SnSe is similar to GeSe but the transition temperature is smaller.

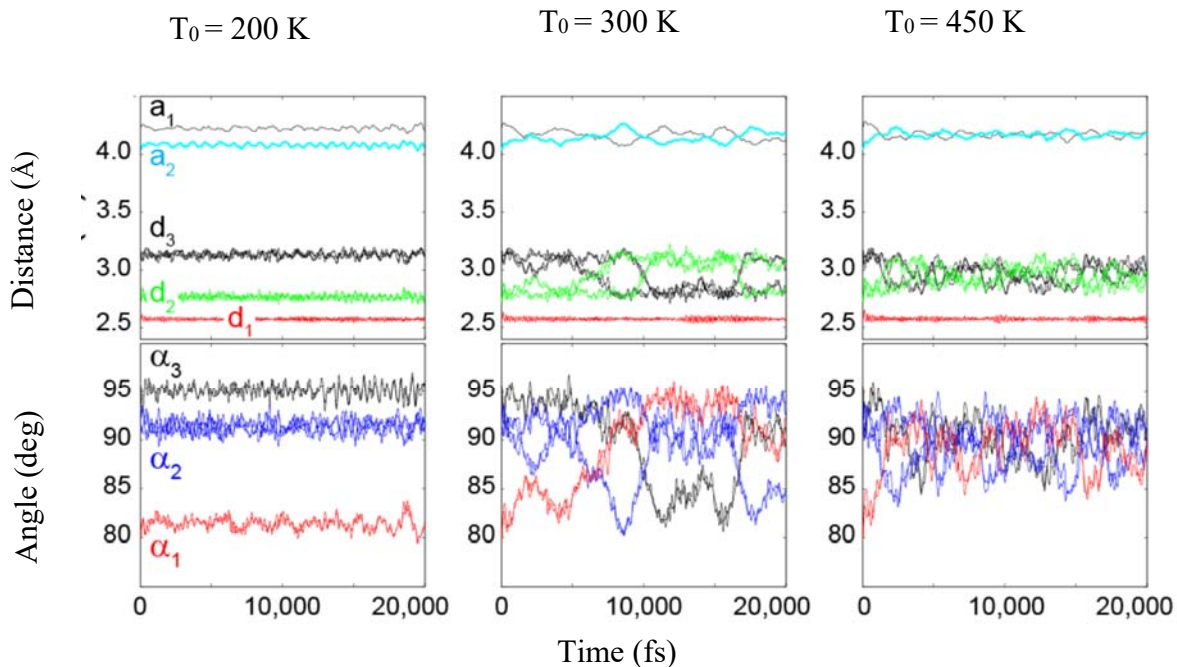


Figure 27. Time evolution of order parameters for GeSe ML.

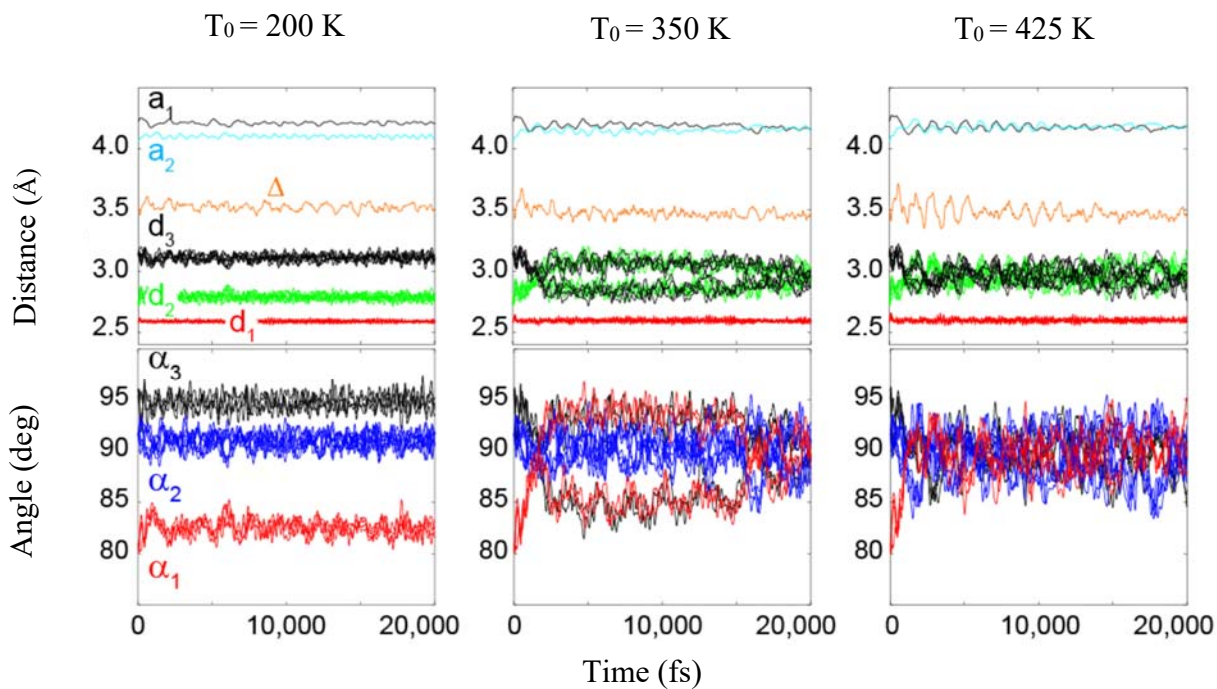


Figure 28. Time evolution of order parameters for GeSe BL.

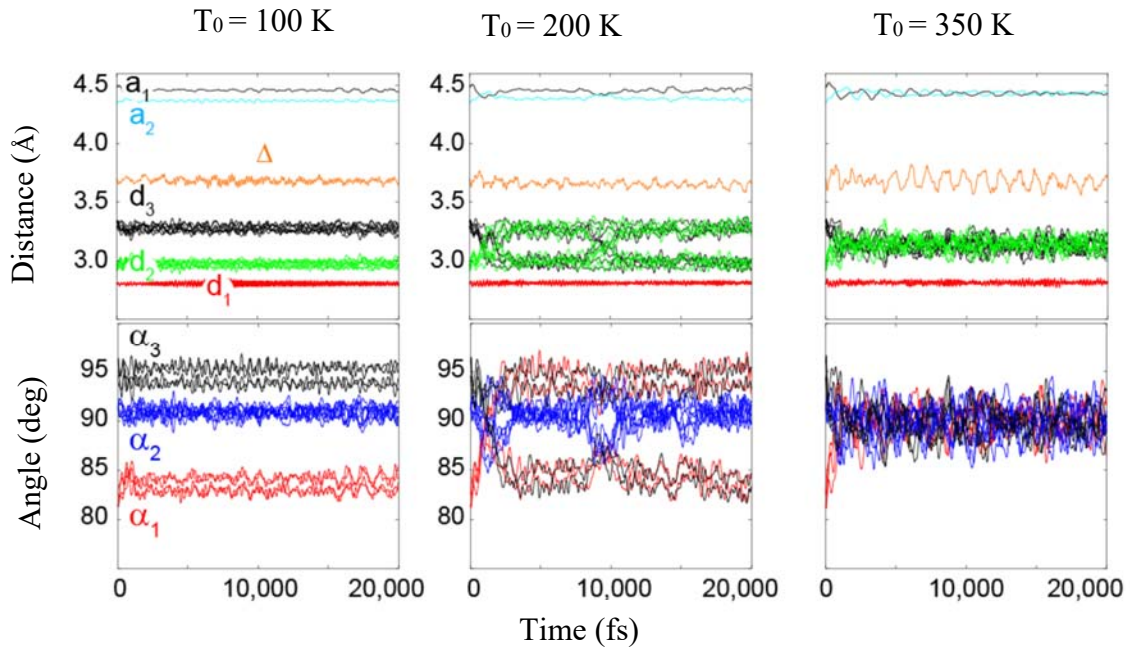


Figure 29. Time evolution of order parameters for SnSe BL.

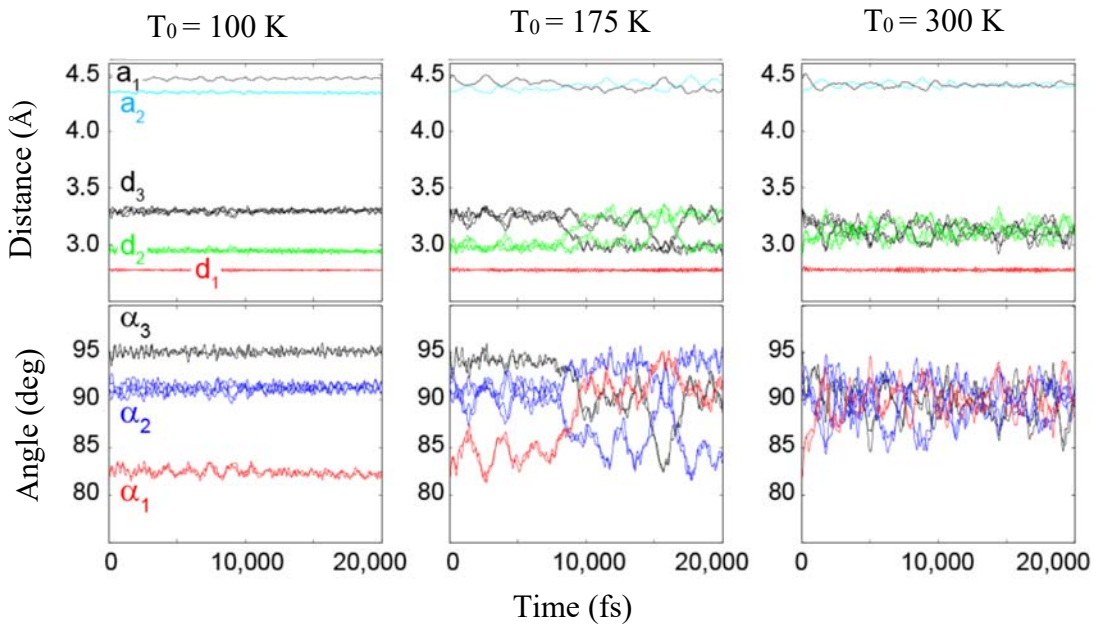


Figure 30. Time evolution of order parameters for SnSe ML.

**Evolution of order parameters by temperature:** For a better illustration of the transition temperature, the average of each order parameter was calculated over the last 15,000 time-steps of the MD calculations. Figures 31 and 32 show the trend of time-averaged order parameters by temperature for monolayer of GeSe, bilayer of GeSe, monolayer of SnSe, and bilayer of SnSe, respectively, and which constitute the most important results of this dissertation.

Figure 31 shows that the average of the two lattice parameters of a monolayer of GeSe collapses to a single value at about  $T_c = 300$  K. This also can be confirmed by  $d_2$ ,  $d_3$ , and the three angles shown in Figure 31. It is worthwhile to emphasize that the nature of these transition is different from melting, as melting transition would be signaled by an isotropic change of all three distances,  $d_1$ ,  $d_2$ , and  $d_3$ .

For GeSe bilayers, the behavior of order parameters show that the transition temperature is slightly higher than the single layer and is  $T_c = 350 \pm 16$  K.

The averages of order parameters of SnSe show  $T_c = 175 \pm 11$  K for monolayers and  $T_c = 225 \pm 9$  K for bilayers. The value of  $T_c$  for bilayers is higher than that of monolayers. This is consistent with the value of phase transition in the bulk which is of the order of 800 K. It was beyond the scope of this research to calculate the phase transition of the multilayer form of these materials.

#### **5.4 Material properties of monolayers and bilayers of GeSe and SnSe**

Strain is a method to modify the properties of crystalline materials, which means change in the structure of crystalline materials will have effects on their properties. Since temperature changes lattice parameters, one can investigate the properties of materials before and after transition temperature in an effect similar to strain. Therefore, the electronic and optical properties of these

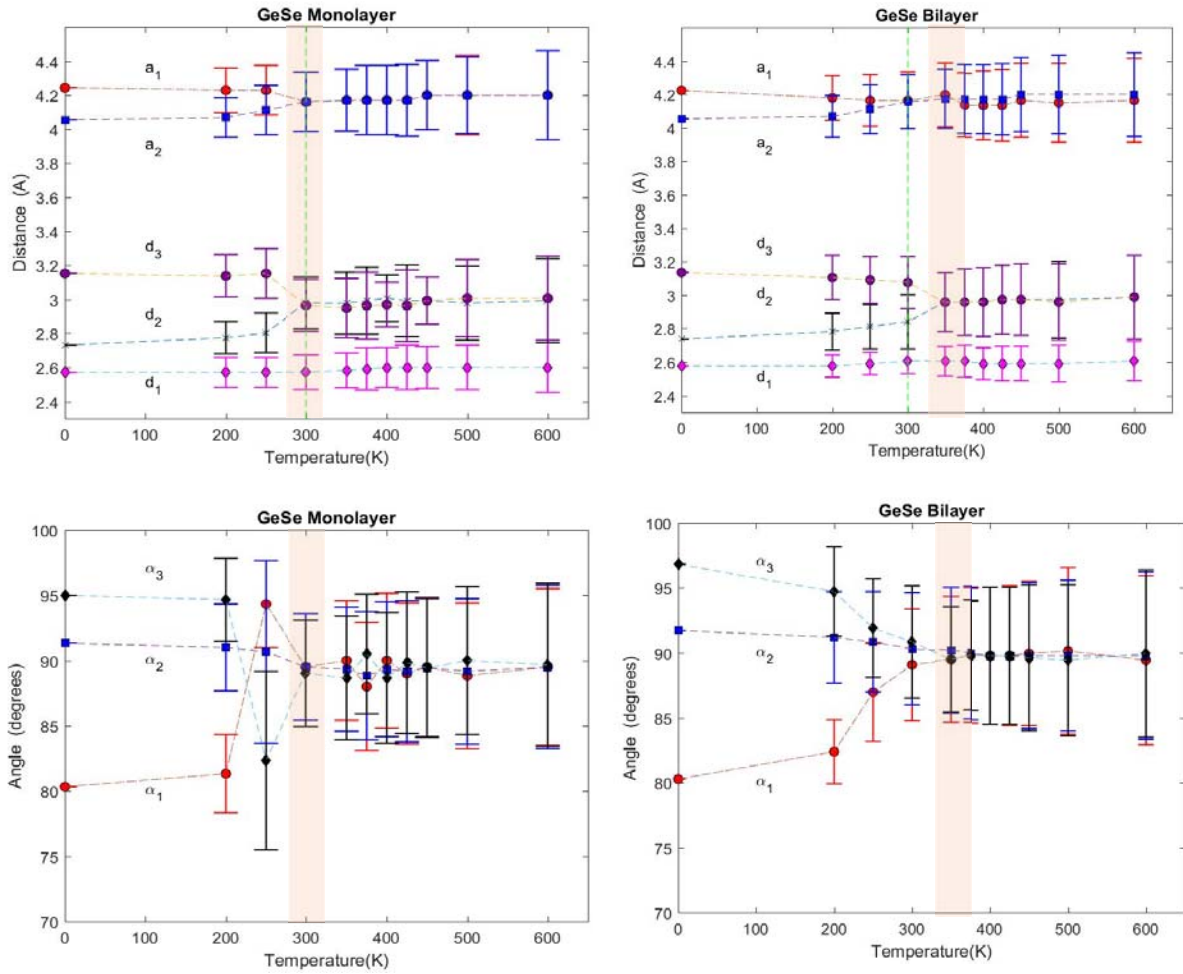


Figure 31. The evolution of averaged order parameters by temperature for GeSe monolayer and bilayers.

materials were investigated above and below the transition temperature.

**MD sample structures:** The estimation of optoelectronic properties was performed on averaged single unit cells. A sampling approach to find the appropriate unit cells at each temperature was used. All the samples must be chosen from the frames after the material is equilibrated. 150 samples were chosen with steps of 100 fs at times given by:

$$t = 100i + 5000 \quad 1 \leq i \leq 150 \quad (\text{Equation 40})$$



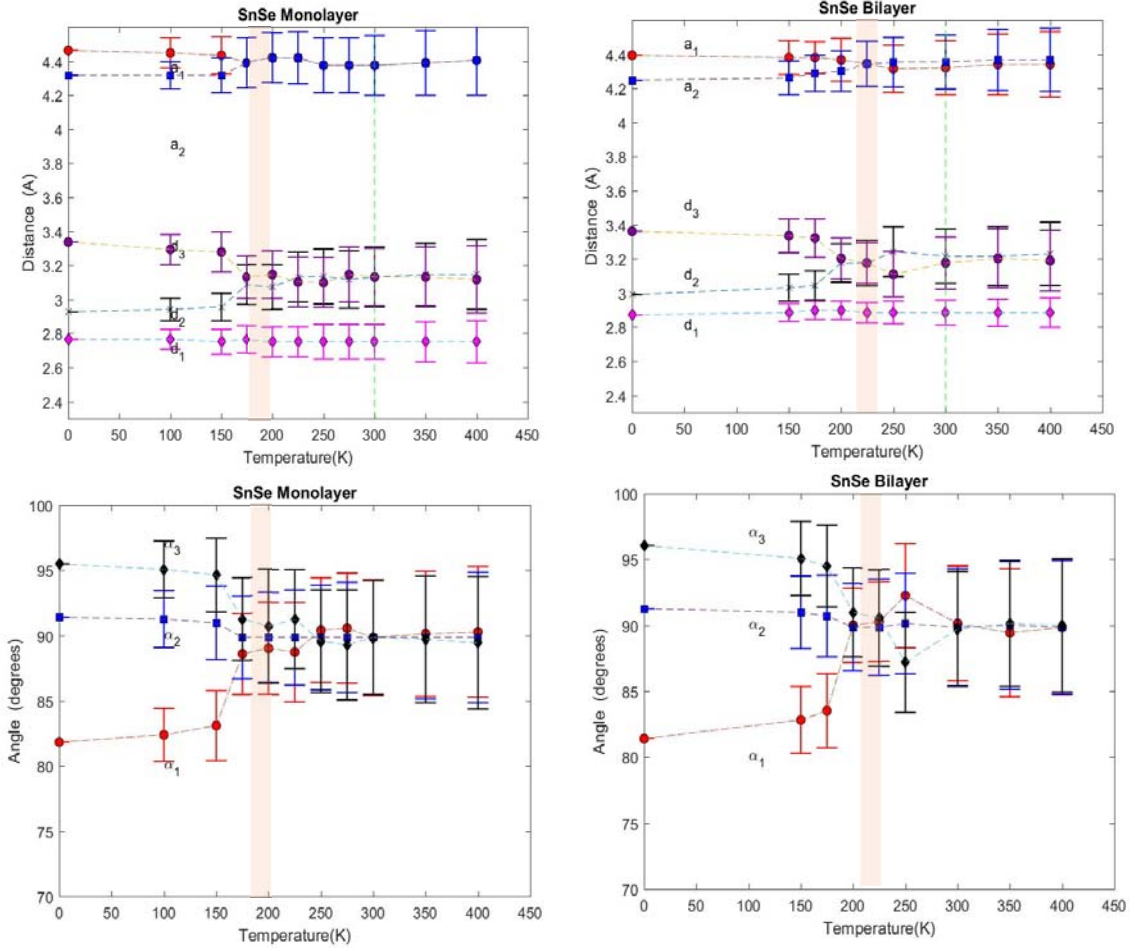


Figure 32. The evolution of averaged order parameters by temperature for SnSe monolayer and bilayer.

## 5.5 Electronic band gap and density of states

The band structure calculations were performed with SIESTA code along the highly symmetric points indicated in Figure 33.

After calculating band structure of all 150 sample unit cells at three different temperatures, they were superimposed on a single figure for each temperature which shows an effective electron coupling. Figure 34 shows these band structures of SnSe monolayer and bilayer at three

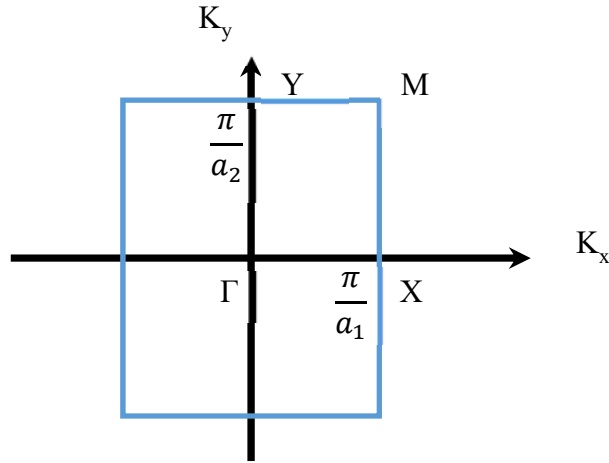


Figure 33. Highly symmetrical points of MMs structure.

temperatures, 0 K, 100 K, and 200 K. Figure 35 shows these band structures of GeSe monolayer and bilayer at three temperatures, 0 K, 200 K, and 400 K.

All four investigated materials will remain semiconductors below and above  $T_c$  as can be seen from the wide gap between conduction and valence bands in Figures 34 and 35. The density of states on the full, non-averaged supercell also show no occupied bands between the conduction band and valence band.

The values of band gap for these materials at different temperatures are shown in Table 6. Upon increasing the material temperature, the magnitude of the band gap changes. The band gap of all four materials are indirect at temperatures below the transition temperature going from kpoint X in the valence band to Y in the conduction band. There is a considerable amount of spin polarization in the conduction and valence bands of these materials at temperature below  $T_c$ . As the temperature becomes close the  $T_c$ , the value of band gap decreases and the indirect band gap of the material becomes direct. Due to the change from a rectangular unit cell to a square one, X and Y in the reciprocal space become equal resulting in a more symmetric band structure.

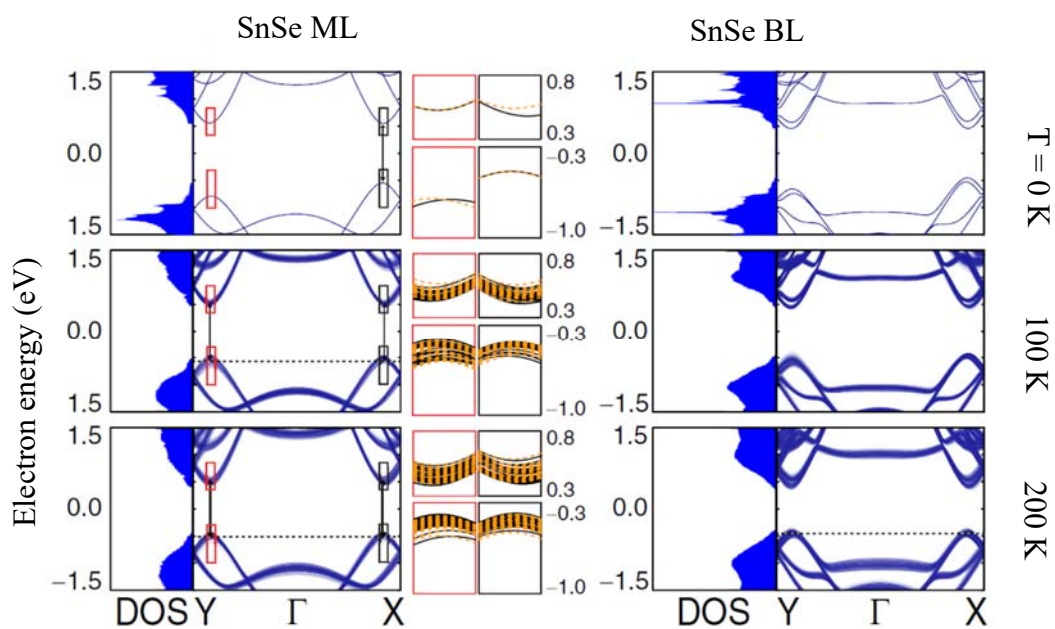


Figure 34. Band structure and density of states of SnSe monolayer and bilayer.

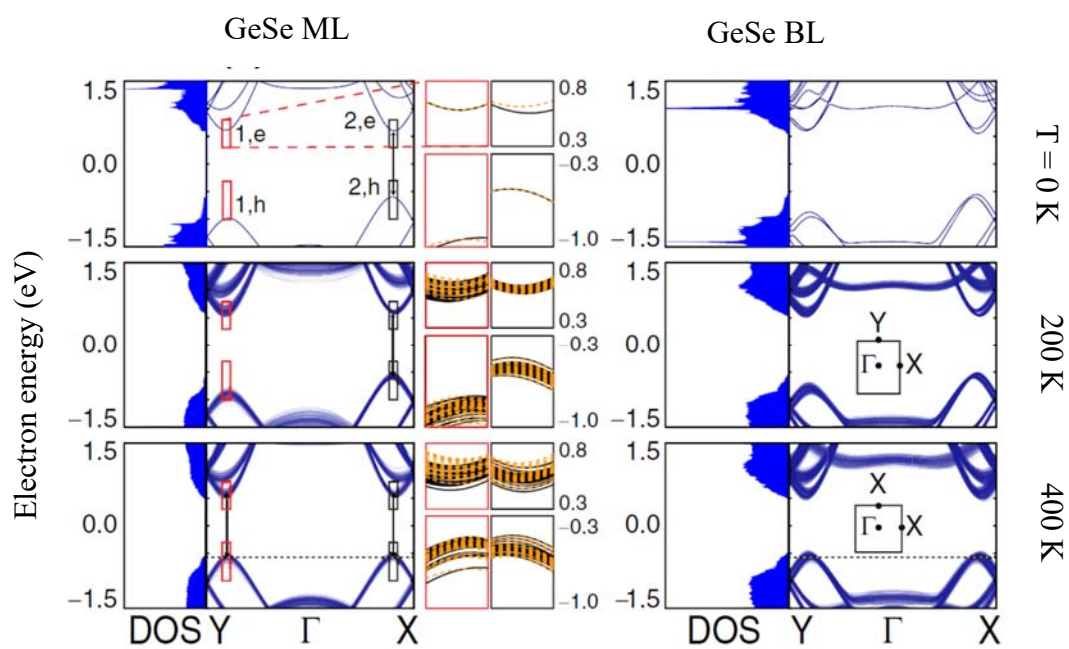


Figure 35. Band structure and density of states of GeSe monolayer and bilayer.

In addition, increasing temperature will cause the spin polarization to be degraded, because the spin up and down bands become broader. Therefore, for the rest of the results, the spin orbit coupling effect was neglected. For the bilayer, because the materials have an AB stacking configuration, the spin polarization is zero due to inversion symmetry.

Table 6. The band gap of SnSe and GeSe monolayers and billayers at  $T = 30$  K,  $T = T_c$  and  $T > T_c$

		SnSe ML	GeSe ML	SnSe BL	GeSe BL
T = 30 K	Band gap (eV)	1.096	1.195	0.910	1.104
	Direct value (eV)	1.0961	1.195	0.911	1.104
	Type of band gap (eV)	direct	direct	indirect	direct
T = $T_c$	Band gap (eV)	$0.916 \pm 0.031$	$1.02 \pm 0.054$	$0.873 \pm 0.025$	$1.07 \pm 0.022$
	Direct value (eV)	$0.958 \pm 0.037$	$1.11 \pm 0.033$	$0.894 \pm 0.0191$	$1.08 \pm 0.015$
	Type of band gap (eV)	indirect	indirect	indirect	indirect
T > $T_c$	Band gap (eV)	$0.854 \pm 0.038$	$0.854 \pm 0.038$	$0.798 \pm 0.039$	$0.100 \pm 0.041$
	Direct value(eV)	$0.931 \pm 0.035$	$0.934 \pm 0.035$	$0.835 \pm 0.029$	$1.05 \pm 0.041$
	Type of band gap (eV)	indirect	indirect	indirect	Indirect

## 5.6 Optical absorption

Another signature of the structural transition is the linear polarized optical absorption spectra shown in Figure 36. In this figure, dashed red lines show the linear optical absorption along the  $a_1$ -line and black lines along  $a_2$ . The gray line is the confidence interval for the black line, and the orange dashed line is the confidence interval for the dashed red line. At  $T < T_c$ , the valleys X and Y are not equal. Therefore, their optical absorption plot versus photon energy are different. However, as the temperature becomes  $T_c$  and above, the optical absorption for both horizontally and vertically polarized light becomes identical.

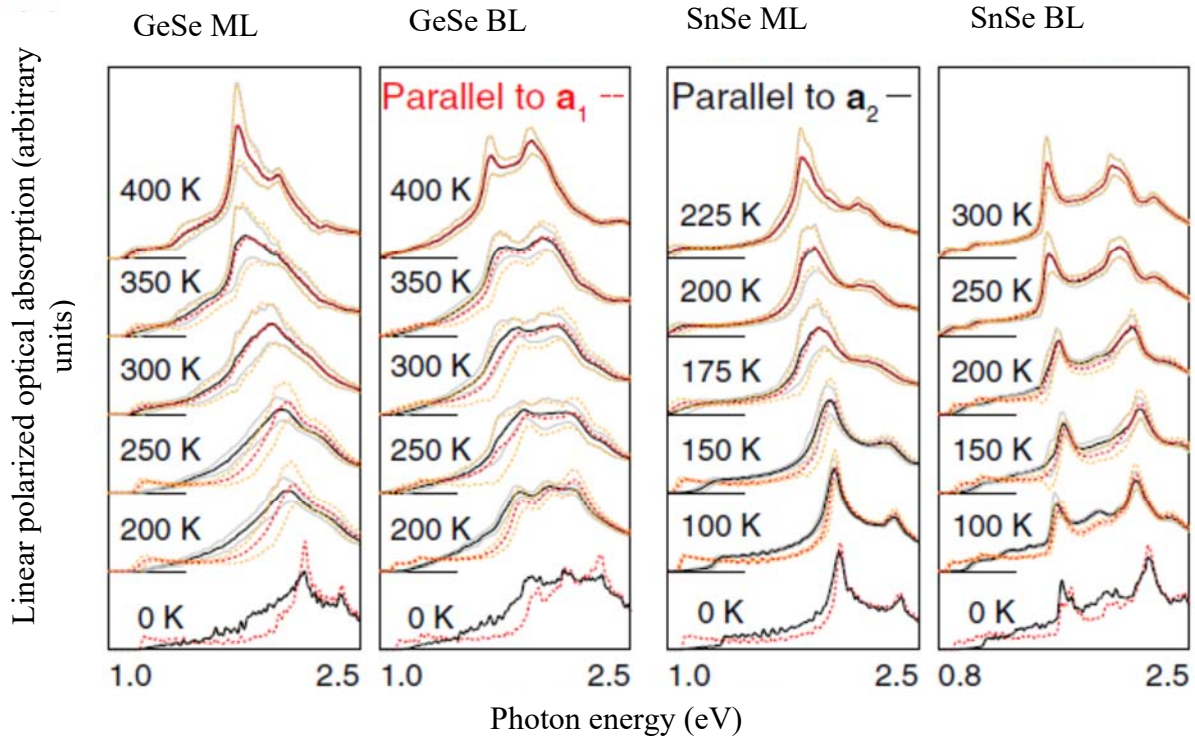


Figure 36. The evolution of optical absorption of four investigated materials.

## 5.7 Piezoelectricity and pyroelectricity

**Piezoelectricity:** Recently, group IV monochalcogenide monolayers were shown to exhibit a high piezoelectric effect [7,8]. All the mentioned studies were performed at zero temperature. However, it is essential to investigate the effect of temperature on the piezoelectricity of these materials especially for  $T > T_c$ . For this purpose, calculations were performed on the 150 averaged unit cells acquired from molecular dynamics calculations. To see the evolution of the piezoelectric effect with temperature, the electronic and ionic dipole moment of GeSe and SnSe monolayer were calculated and plotted in Figure 37.

The magnitude of the dipole moment as a function of temperature at  $T < T_c$ , is consistent with previous studies showing large piezoelectric response at zero temperature. However, there is a sudden change in the value of dipole moment as the temperature becomes close to  $T_c$ . For  $T >$

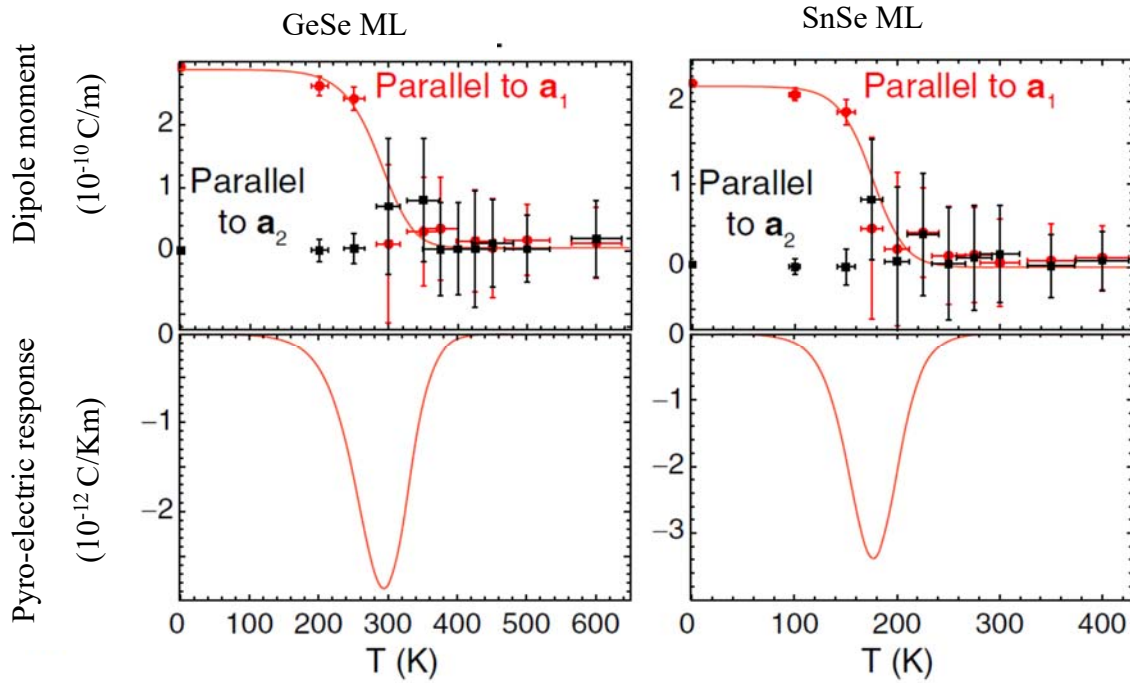


Figure 37. The temperature evolution of the dipole moment and pyroelectric response of GeSe and SnSe monolayers.

$T_c$  the dipole moment becomes zero or very close to zero. Due to the transition, the average orientation of dipole moments in the supercell becomes zero. Consequently, the piezoelectric effect vanishes at  $T > T_c$ .

**Pyroelectricity:** Pyroelectricity is the ability of certain crystals to produce temporary voltage upon change in their temperature. Pyroelectric materials are naturally polarized and by change in their temperature, a large electric field will be created which creates temporary voltage in these materials. If the material stays at a temperature for some time, the electric field vanishes due to leakage current. Pyroelectricity is different from thermoelectricity in which the material is conducting heat between two unequal temperatures and, consequently, creates voltage. The pyroelectric coefficient is the change of the spontaneous polarization vector by temperature as shown in Equation 37:

$$p_i = \frac{dP}{dT} \quad (\text{Equation 37})$$

The lower plots of Figure 37 show the pyroelectric response of monolayers of GeSe and SnSe.

## 5.8 Summary and discussion

In this chapter, structural changes in group IV monochalcogenides were described. To exemplify, monolayers and bilayers of GeSe and SnSe were selected. These materials undergo a 2D phase transition, which is the main contribution of this dissertation. This phase transition is due to the degeneracy in the structural ground state of these materials, which was discussed in Chapter Four. The phase transition transforms the average unit cell of these materials from a rectangular unit cell to a square one. This 2D phase transition also changes the properties of these materials. The effect of this phase transition on properties of these materials were investigated using Car-Parrinello molecular dynamics. The 2D phase transition for SnSe monolayer and bilayer happens at 200 K and 225 K, respectively. Phase transition for monolayer and bilayer of GeSe occurs at a higher temperature of 300 K and 350 K, respectively.

The electronic band gap of these materials below  $T_c$  has two distinct valleys in the conduction bands and two different valleys in the valence bands near the X and Y points in the Brillouin zone. Upon the 2D phase transition, the X and Y valleys in the conduction band become equal and X and Y valleys in the valence band also become equal. This fact is an additional signature of the phase transition, and it shows the effect of phase transition on the electronic properties of the material.

Below  $T_c$ , GeSe ML and SnSe ML have dipole moments equal to  $2.6 \times 10^{-10}$  C/m and  $2.3 \times 10^{-10}$  C/m, respectively. Consequently, these materials exhibit a large piezoelectric response.

However, at temperatures close to and above  $T_c$ , the dipole moment of these materials vanishes. This reduces the piezoelectricity of these materials near and above critical temperature, and induces a pyroelectric response.



## References

- [1] A.A. Pacheco Sanjuan, M. Mehboudi, E.O. Harriss, H. Terrones and S. Barraza-Lopez, "Quantitative Chemistry and the Discrete Geometry of Conformal Atom-Thin Crystals," *ACS nano*, vol. 8, no. 2, pp. 1136-1146.
- [2] M. Mehboudi, K. Utt, H. Terrones, E.O. Harriss, A.A. Pacheco SanJuan and S. Barraza-Lopez, "Strain and the optoelectronic properties of nonplanar phosphorene monolayers," *Proc.Natl.Acad.Sci.U.S.A.*, vol. 112, no. 19, May 12, pp. 5888-5892.
- [3] H. Liu, A.T. Neal, Z. Zhu, Z. Luo, X. Xu, D. Tománek and P.D. Ye, "Phosphorene: An Unexplored 2D Semiconductor with a High Hole Mobility," *ACS Nano*, vol. 8, no. 4, pp. 4033-4041.
- [4] J. Dai and X.C. Zeng, "Bilayer phosphorene: effect of stacking order on bandgap and its potential applications in thin-film solar cells," *The Journal of Physical Chemistry Letters*, vol. 5, no. 7, pp. 1289-1293.
- [5] L.C. Gomes and A. Carvalho, "Phosphorene analogues: Isoelectronic two-dimensional group-IV monochalcogenides with orthorhombic structure," *Physical Review B*, vol. 92, no. 8, pp. 085406.
- [6] P. Bridgman, "Two new modifications of phosphorus." *J.Am.Chem.Soc.*, vol. 36, no. 7, pp. 1344-1363.
- [7] L.C. Gomes, A. Carvalho and A.C. Neto, "Enhanced piezoelectricity and modified dielectric screening of two-dimensional group-IV monochalcogenides," *Physical Review B*, vol. 92, no. 21, pp. 214103.
- [8] R. Fei, W. Li, J. Li and L. Yang, "Giant piezoelectricity of monolayer group IV monochalcogenides: SnSe, SnS, GeSe, and GeS," *Appl.Phys.Lett.*, vol. 107, no. 17, pp. 173104.
- [9] R. Haleoot, C. Paillard, T.P. Kaloni, M. Mehboudi, B. Xu, L. Bellaiche and S. Barraza-Lopez, "Photostrictive two-dimensional materials in the monochalcogenide family," *Phys.Rev.Lett.*, vol. 118, no. 22, pp. 227401.
- [10] M. Mehboudi, B.M. Fregoso, Y. Yang, W. Zhu, A. van der Zande, J. Ferrer, L. Bellaiche, P. Kumar and S. Barraza-Lopez, "Structural phase transition and material properties of few-layer monochalcogenides," *Phys.Rev.Lett.*, vol. 117, no. 24, pp. 246802.
- [11] M. Mehboudi, A.M. Dorio, W. Zhu, A. van der Zande, H.O. Churchill, A.A. Pacheco-Sanjuan, E.O. Harriss, P. Kumar and S. Barraza-Lopez, "Two-dimensional disorder in black phosphorus and monochalcogenide monolayers," *Nano Letters*, vol. 16, no. 3, pp. 1704-1712.
- [12] P. Hohenberg and W. Kohn, "Inhomogeneous electron gas," *Physical Review*, vol. 136, no. 3B, pp. B864.

- [13] W. Kohn and L.J. Sham, "Self-consistent equations including exchange and correlation effects," *Physical review*, vol. 140, no. 4A, pp. A1133.
- [14] R. Peierls, "Some properties of solids," *Ann.Inst.Henri Poincaré*, vol. 5, pp. 177-222.
- [15] K. Novoselov, A.K. Geim, S. Morozov, D. Jiang, M. Katsnelson, I. Grigorieva, S. Dubonos and A. Firsov, "Two-dimensional gas of massless Dirac fermions in graphene," *Nature*, vol. 438, no. 7065, pp. 197-200.
- [16] E. Hwang, S. Adam and S.D. Sarma, "Carrier transport in two-dimensional graphene layers," *Phys.Rev.Lett.*, vol. 98, no. 18, pp. 186806.
- [17] K.I. Bolotin, K. Sikes, Z. Jiang, M. Klima, G. Fudenberg, J. Hone, P. Kim and H. Stormer, "Ultrahigh electron mobility in suspended graphene," *Solid State Commun.*, vol. 146, no. 9, pp. 351-355.
- [18] K. Novoselov, A.K. Geim, S. Morozov, D. Jiang, M.K.I. Grigorieva, S. Dubonos and A. Firsov, "Two-dimensional gas of massless Dirac fermions in graphene," *Nature*, vol. 438, no. 7065, pp. 197-200.
- [19] K.S. Novoselov, Z. Jiang, Y. Zhang, S.V. Morozov, H.L. Stormer, U. Zeitler, J.C. Maan, G.S. Boebinger, P. Kim and A.K. Geim, "Room-temperature quantum Hall effect in graphene," *Science*, vol. 315, no. 5817, Mar 9, pp. 1379.
- [20] S.D. Sarma, S. Adam, E. Hwang and E. Rossi, "Electronic transport in two-dimensional graphene," *Reviews of Modern Physics*, vol. 83, no. 2, pp. 407.
- [21] S. Ghosh, I. Calizo, D. Teweldebrhan, E.P. Pokatilov, D.L. Nika, A.A. Balandin, W. Bao, F. Miao and C.N. Lau, "Extremely high thermal conductivity of graphene: Prospects for thermal management applications in nanoelectronic circuits," *Appl.Phys.Lett.*, vol. 92, no. 15, pp. 151911.
- [22] A.A. Balandin, S. Ghosh, W. Bao, I. Calizo, D. Teweldebrhan, F. Miao and C.N. Lau, "Superior thermal conductivity of single-layer graphene," *Nano Letters*, vol. 8, no. 3, pp. 902-907.
- [23] C.R. Dean, A.F. Young, I. Meric, C. Lee, L. Wang, S. Sorgenfrei, K. Watanabe, T. Taniguchi, P. Kim and K.L. Shepard, "Boron nitride substrates for high-quality graphene electronics," *Nature Nanotechnology*, vol. 5, no. 10, pp. 722-726.
- [24] Y.Y. Wang, Z.H. Ni, T. Yu, Z.X. Shen, H.M. Wang, Y.H. Wu, W. Chen and A.T. Shen Wee, "Raman studies of monolayer graphene: the substrate effect," *The Journal of Physical Chemistry C*, vol. 112, no. 29, pp. 10637-10640.
- [25] S. Choi, S. Jhi and Y. Son, "Effects of strain on electronic properties of graphene," *Physical Review B*, vol. 81, no. 8, pp. 081407.

- [26] V.M. Pereira, R. Ribeiro, N. Peres and A.C. Neto, "Optical properties of strained graphene," *EPL (Europhysics Letters)*, vol. 92, no. 6, pp. 67001.
- [27] G.G. Naumis, S. Barraza-Lopez, M. Oliva-Leyva and H. Terrones, "Electronic and optical properties of strained graphene and other strained 2D materials: a review," *Reports on Progress in Physics*, vol. 80, no 9, pp 096501.
- [28] K.F. Mak, C.H. Lui, J. Shan and T.F. Heinz, "Observation of an electric-field-induced band gap in bilayer graphene by infrared spectroscopy," *Phys.Rev.Lett.*, vol. 102, no. 25, pp. 256405.
- [29] J. Yan, Y. Zhang, P. Kim and A. Pinczuk, "Electric field effect tuning of electron-phonon coupling in graphene," *Phys.Rev.Lett.*, vol. 98, no. 16, pp. 166802.
- [30] J. Chen, C. Jang, S. Xiao, M. Ishigami and M.S. Fuhrer, "Intrinsic and extrinsic performance limits of graphene devices on SiO<sub>2</sub>," *Nature Nanotechnology*, vol. 3, no. 4, pp. 206-209.
- [31] C. Lee, X. Wei, J.W. Kysar and J. Hone, "Measurement of the elastic properties and intrinsic strength of monolayer graphene," *Science*, vol. 321, no. 5887, Jul 18, pp. 385-388.
- [32] Y. Zhang, T. Tang, C. Girit, Z. Hao, M.C. Martin, A. Zettl, M.F. Crommie, Y.R. Shen and F. Wang, "Direct observation of a widely tunable bandgap in bilayer graphene," *Nature*, vol. 459, no. 7248, pp. 820.
- [33] W. Liu, S. Kraemer, D. Sarkar, H. Li, P.M. Ajayan and K. Banerjee, "Controllable and rapid synthesis of high-quality and large-area Bernal stacked bilayer graphene using chemical vapor deposition," *Chemistry of Materials*, vol. 26, no. 2, pp. 907-915.
- [34] H. Min, B. Sahu, S.K. Banerjee and A. MacDonald, "Ab initio theory of gate induced gaps in graphene bilayers," *Physical Review B*, vol. 75, no. 15, pp. 155115.
- [35] K. Jeon, Z. Lee, E. Pollak, L. Moreschini, A. Bostwick, C. Park, R. Mendelsberg, V. Radmilovic, R. Kostecki and T.J. Richardson, "Fluorographene: a wide bandgap semiconductor with ultraviolet luminescence," *ACS Nano*, vol. 5, no. 2, pp. 1042-1046.
- [36] J. He, M.G. Kanatzidis and V.P. Dravid, "High performance bulk thermoelectrics via a panoscopic approach," *Materials Today*, vol. 16, no. 5, pp. 166-176.
- [37] C. Satterthwaite and R. Ure Jr, "Electrical and thermal properties of Bi<sub>2</sub>Te<sub>3</sub>," *Physical Review*, vol. 108, no. 5, pp. 1164.
- [38] D. Hsieh, Y. Xia, D. Qian, L. Wray, F. Meier, J. Dil, J. Osterwalder, L. Patthey, A. Fedorov and H. Lin, "Observation of time-reversal-protected single-Dirac-cone topological-insulator states in Bi<sub>2</sub>Te<sub>3</sub> and Sb<sub>2</sub>Te<sub>3</sub>," *Phys.Rev.Lett.*, vol. 103, no. 14, pp. 146401.

- [39] A. Subedi, L. Zhang, D.J. Singh and M. Du, “Density functional study of FeS, FeSe, and FeTe: Electronic structure, magnetism, phonons, and superconductivity,” *Physical Review B*, vol. 78, no. 13, pp. 134514.
- [40] H. Kotegawa, S. Masaki, Y. Awai, H. Tou, Y. Mizuguchi and Y. Takano, “Evidence for unconventional superconductivity in arsenic-free iron-based superconductor FeSe: a  $^{77}\text{Se}$ -NMR study,” *Journal of the Physical Society of Japan*, vol. 77, no. 11, pp. 113703-113703.
- [41] T. Ying, X. Lai, X. Hong, Y. Xu, L. He, J. Zhang, M. Wang, Y. Yu, F. Huang and S. Li, “Nodal superconductivity in FeS: Evidence from quasiparticle heat transport,” *Physical Review B*, vol. 94, no. 10, pp. 100504.
- [42] Q.H. Wang, K. Kalantar-Zadeh, A. Kis, J.N. Coleman and M.S. Strano, “Electronics and optoelectronics of two-dimensional transition metal dichalcogenides,” *Nature Nanotechnology*, vol. 7, no. 11, pp. 699-712.
- [43] R. Ganatra and Q. Zhang, “Few-layer MoS<sub>2</sub>: a promising layered semiconductor,” *ACS Nano*, vol. 8, no. 5, pp. 4074-4099.
- [44] B. Radisavljevic, A. Radenovic, J. Brivio, V. Giacometti and A. Kis, “Single-layer MoS<sub>2</sub> transistors,” *Nature Nanotechnology*, vol. 6, no. 3, pp. 147-150.
- [45] Q. Lu, Y. Yu, Q. Ma, B. Chen and H. Zhang, “2D Transition-Metal-Dichalcogenide-Nanosheet-Based Composites for Photocatalytic and Electrocatalytic Hydrogen Evolution Reactions,” *Adv Mater*, vol. 28, no. 10, pp. 1917-1933.
- [46] L. Li, Y. Yu, G.J. Ye, Q. Ge, X. Ou, H. Wu, D. Feng, X.H. Chen and Y. Zhang, “Black phosphorus field-effect transistors,” *Nature Nanotechnology*.
- [47] H. Liu, A.T. Neal, Z. Zhu, Z. Luo, X. Xu, D. Tománek and D.Y. Peide, “Phosphorene: an unexplored 2D semiconductor with a high hole mobility,”.
- [48] R. Eymard and A. Otto, “Optical and electron-energy-loss spectroscopy of GeS, GeSe, SnS, and SnSe single crystals,” *Physical Review B*, vol. 16, no. 4, pp. 1616.
- [49] M. Parenteau and C. Carlone, “Influence of temperature and pressure on the electronic transitions in SnS and SnSe semiconductors,” *Physical Review B*, vol. 41, no. 8, pp. 5227.
- [50] P.D. Antunez, J.J. Buckley and R.L. Brutchey, “Tin and germanium monochalcogenide IV–VI semiconductor nanocrystals for use in solar cells,” *Nanoscale*, vol. 3, no. 6, pp. 2399-2411.
- [51] G.A. Tritsarlis, B.D. Malone and E. Kaxiras, “Optoelectronic properties of single-layer, double-layer, and bulk tin sulfide: A theoretical study,” *J.Appl.Phys.*, vol. 113, no. 23, pp. 233507.

- [52] L. Zhao, S. Lo, Y. Zhang, H. Sun, G. Tan, C. Uher, C. Wolverton, V.P. Dravid and M.G. Kanatzidis, "Ultralow thermal conductivity and high thermoelectric figure of merit in SnSe crystals," *Nature*, vol. 508, no. 7496, pp. 373.
- [53] L.D. Zhao, G. Tan, S. Hao, J. He, Y. Pei, H. Chi, H. Wang, S. Gong, H. Xu, V.P. Dravid, C. Uher, G.J. Snyder, C. Wolverton and M.G. Kanatzidis, "Ultrahigh power factor and thermoelectric performance in hole-doped single-crystal SnSe," *Science*, vol. 351, no. 6269, Jan 8, pp. 141-144.
- [54] V. Steinmann, R. Jaramillo, K. Hartman, R. Chakraborty, R.E. Brandt, J.R. Poindexter, Y.S. Lee, L. Sun, A. Polizzotti and H.H. Park, "3.88% efficient tin sulfide solar cells using congruent thermal evaporation," *Adv Mater*, vol. 26, no. 44, pp. 7488-7492.
- [55] P. Sinsermsuksakul, K. Hartman, S. Bok Kim, J. Heo, L. Sun, H. Hejin Park, R. Chakraborty, T. Buonassisi and R.G. Gordon, "Enhancing the efficiency of SnS solar cells via band-offset engineering with a zinc oxysulfide buffer layer," *Appl.Phys.Lett.*, vol. 102, no. 5, pp. 053901.
- [56] P. Sinsermsuksakul, L. Sun, S.W. Lee, H.H. Park, S.B. Kim, C. Yang and R.G. Gordon, "Overcoming Efficiency Limitations of SnS-Based Solar Cells," *Advanced Energy Materials*, vol. 4, no. 15.
- [57] J.P. Heremans, V. Jovovic, E.S. Toberer, A. Saramat, K. Kurosaki, A. Charoenphakdee, S. Yamanaka and G.J. Snyder, "Enhancement of thermoelectric efficiency in PbTe by distortion of the electronic density of states," *Science*, vol. 321, no. 5888, Jul 25, pp. 554-557.
- [58] E.V. Castro, K. Novoselov, S. Morozov, N. Peres, J.L. Dos Santos, J. Nilsson, F. Guinea, A. Geim and A.C. Neto, "Biased bilayer graphene: semiconductor with a gap tunable by the electric field effect," *Phys.Rev.Lett.*, vol. 99, no. 21, pp. 216802.
- [59] M.Y. Han, B. Özyilmaz, Y. Zhang and P. Kim, "Energy band-gap engineering of graphene nanoribbons," *Phys.Rev.Lett.*, vol. 98, no. 20, pp. 206805.
- [60] A. Rodin, A. Carvalho and A.C. Neto, "Strain-induced gap modification in black phosphorus," *Phys.Rev.Lett.*, vol. 112, no. 17, pp. 176801.
- [61] S. Zhang, J. Yang, R. Xu, F. Wang, W. Li, M. Ghufraan, Y. Zhang, Z. Yu, G. Zhang and Q. Qin, "Extraordinary photoluminescence and strong temperature/angle-dependent Raman responses in few-layer phosphorene," *ACS Nano*, vol. 8, no. 9, pp. 9590-9596.
- [62] J. He, D. He, Y. Wang, Q. Cui, M.Z. Bellus, H. Chiu and H. Zhao, "Exceptional and anisotropic transport properties of photocarriers in black phosphorus," *ACS Nano*, vol. 9, no. 6, pp. 6436-6442.
- [63] J. Qiao, X. Kong, Z.X. Hu, F. Yang and W. Ji, "High-mobility transport anisotropy and linear dichroism in few-layer black phosphorus," *Nat.Commun.*, vol. 5, Jul 21, pp. 4475.

- [64] T. Low, A. Rodin, A. Carvalho, Y. Jiang, H. Wang, F. Xia and A.C. Neto, "Tunable optical properties of multilayer black phosphorus thin films," *Physical Review B*, vol. 90, no. 7, pp. 075434.
- [65] A. Castellanos-Gomez, L. Vicarelli, E. Prada, J.O. Island, K. Narasimha-Acharya, S.I. Blanter, D.J. Groenendijk, M. Buscema, G.A. Steele and J. Alvarez, "Isolation and characterization of few-layer black phosphorus," *2D Materials*, vol. 1, no. 2, pp. 025001.
- [66] K.L. Utt, P. Rivero, M. Mehboudi, E.O. Harriss, M.F. Borunda, A.A. Pacheco SanJuan and S. Barraza-Lopez, "Intrinsic defects, fluctuations of the local shape, and the photo-oxidation of black phosphorus," *ACS Central Science*, vol. 1, no. 6, pp. 320-327.
- [67] D.D. Vaughn, S. In and R.E. Schaak, "A precursor-limited nanoparticle coalescence pathway for tuning the thickness of laterally-uniform colloidal nanosheets: the case of SnSe," *ACS Nano*, vol. 5, no. 11, pp. 8852-8860.
- [68] L. Li, Z. Chen, Y. Hu, X. Wang, T. Zhang, W. Chen and Q. Wang, "Single-layer single-crystalline SnSe nanosheets," *J.Am.Chem.Soc.*, vol. 135, no. 4, pp. 1213-1216.
- [69] B. Mukherjee, Y. Cai, H.R. Tan, Y.P. Feng, E.S. Tok and C.H. Sow, "NIR Schottky photodetectors based on individual single-crystalline GeSe nanosheet," *ACS applied materials & interfaces*, vol. 5, no. 19, pp. 9594-9604.
- [70] A.K. Singh and R.G. Hennig, "Computational prediction of two-dimensional group-IV monochalcogenides," *Appl.Phys.Lett.*, vol. 105, no. 4, pp. 042103.
- [71] Y. Ji, H. Dong, M. Yang, T. Hou and Y. Li, "Monolayer germanium monochalcogenides (GeS/GeSe) as cathode catalysts in nonaqueous Li-O<sub>2</sub> batteries," *Physical Chemistry Chemical Physics*, vol. 19, no. 31, pp. 20457-20462.
- [72] C. Chowdhury, S. Karmakar and A. Datta, "Monolayer Group IV-VI Monochalcogenides: Low-Dimensional Materials for Photocatalytic Water Splitting," *The Journal of Physical Chemistry C*, vol. 121, no. 14, pp. 7615-7624.
- [73] A. Shafique and Y. Shin, "Thermoelectric and phonon transport properties of two-dimensional IV-VI compounds," *Scientific Reports*, vol. 7, no. 1, pp. 506.
- [74] K. Chang, J. Liu, H. Lin, N. Wang, K. Zhao, A. Zhang, F. Jin, Y. Zhong, X. Hu, W. Duan, Q. Zhang, L. Fu, Q.K. Xue, X. Chen and S.H. Ji, "Discovery of robust in-plane ferroelectricity in atomic-thick SnTe," *Science*, vol. 353, no. 6296, Jul 15, pp. 274-278.
- [75] M. Born and R. Oppenheimer, "Zur quantentheorie der molekeln," *Annalen der Physik*, vol. 389, no. 20, pp. 457-484.

- [76] D.R. Hartree, “The wave mechanics of an atom with a non-Coulomb central field. Part I. Theory and methods,” *Mathematical Proceedings of the Cambridge Philosophical Society*, vol. 24, no. 1, pp. 89-110.
- [77] L.H. Thomas, “The calculation of atomic fields,” *Mathematical Proceedings of the Cambridge Philosophical Society*, vol. 23, no. 5, pp. 542-548.
- [78] P. Hohenberg and W. Kohn, “Inhomogeneous electron gas,” *Physical review*, vol. 136, no. 3B, pp. B864.
- [79] W. Kohn and L.J. Sham, “Self-consistent equations including exchange and correlation effects,” *Physical review*, vol. 140, no. 4A, pp. A1133.
- [80] J.P. Perdew and K. Burke, “Comparison shopping for a gradient-corrected density functional,” *International Journal of Quantum Chemistry*, vol. 57, no. 3, pp. 309-319.
- [81] J.P. Perdew, K. Burke and M. Ernzerhof, “Generalized gradient approximation made simple,” *Phys.Rev.Lett.*, vol. 77, no. 18, pp. 3865.
- [82] D.M. Ceperley and B. Alder, “Ground state of the electron gas by a stochastic method,” *Phys.Rev.Lett.*, vol. 45, no. 7, pp. 566.
- [83] J.P. Perdew, K. Burke and M. Ernzerhof, “Generalized gradient approximation made simple,” *Phys.Rev.Lett.*, vol. 77, no. 18, pp. 3865.
- [84] M. Dion, H. Rydberg, E. Schröder, D.C. Langreth and B.I. Lundqvist, “Van der Waals density functional for general geometries,” *Phys.Rev.Lett.*, vol. 92, no. 24, pp. 246401.
- [85] G. Román-Pérez and J.M. Soler, “Efficient implementation of a van der Waals density functional: application to double-wall carbon nanotubes,” *Phys.Rev.Lett.*, vol. 103, no. 9, pp. 096102.
- [86] H. Rydberg, B.I. Lundqvist, D.C. Langreth and M. Dion, “Tractable nonlocal correlation density functionals for flat surfaces and slabs,” *Physical Review B*, vol. 62, no. 11, pp. 6997.
- [87] D. Langreth, B.I. Lundqvist, S.D. Chakarova-Käck, V. Cooper, M. Dion, P. Hyldgaard, A. Kelkkanen, J. Kleis, L. Kong and S. Li, “A density functional for sparse matter,” *Journal of Physics: Condensed Matter*, vol. 21, no. 8, pp. 084203.
- [88] G. Kresse and J. Furthmüller, “Efficient iterative schemes for ab initio total-energy calculations using a plane-wave basis set,” *Physical Review B*, vol. 54, no. 16, pp. 11169.
- [89] G. Kresse and D. Joubert, “From ultrasoft pseudopotentials to the projector augmented-wave method,” *Physical Review B*, vol. 59, no. 3, pp. 1758.

- [90] P. Ordejón, E. Artacho and J.M. Soler, “Self-consistent order-N density-functional calculations for very large systems,” *Physical Review B*, vol. 53, no. 16, pp. R10441.
- [91] J.M. Soler, E. Artacho, J.D. Gale, A. García, J. Junquera, P. Ordejón and D. Sánchez-Portal, “The SIESTA method for ab initio order-N materials simulation,” *Journal of Physics: Condensed Matter*, vol. 14, no. 11, pp. 2745.
- [92] J.M. Soler, M.R. Beltrán, K. Michaelian, I.L. Garzón, P. Ordejón, D. Sánchez-Portal and E. Artacho, “Metallic bonding and cluster structure,” *Physical Review B*, vol. 61, no. 8, pp. 5771.
- [93] H.J. Monkhorst and J.D. Pack, “Special points for Brillouin-zone integrations,” *Physical Review B*, vol. 13, no. 12, pp. 5188.
- [94] Z. Ong, Y. Cai, G. Zhang and Y. Zhang, “Strong thermal transport anisotropy and strain modulation in single-layer phosphorene,” *The Journal of Physical Chemistry C*, vol. 118, no. 43, pp. 25272-25277.
- [95] G. Qin, Q. Yan, Z. Qin, S. Yue, M. Hu and G. Su, “Anisotropic intrinsic lattice thermal conductivity of phosphorene from first principles,” *Physical Chemistry Chemical Physics*, vol. 17, no. 7, pp. 4854-4858.
- [96] A. Jain and A.J. McGaughey, “Strongly anisotropic in-plane thermal transport in single-layer black phosphorene,” *Sci.Rep.*, vol. 5, Feb 17, pp. 8501.
- [97] D.R. Lide, “Handbook of Chemistry and Physics.” Section 4, Properties of Elements and Inorganic Compounds”, *CRC Press* 2004.
- [98] D. Wales, “Energy landscapes: Applications to clusters, biomolecules and glasses,” Chapter 6 page 283, *Cambridge University Press* 2003.
- [99] R.B. Potts, “Some generalized order-disorder transformations,” *Mathematical proceedings of the Cambridge Philosophical Society*, vol. 48, no. 1, pp. 106-109.
- [100] H. Wang and X. Qian, “Two-dimensional multiferroics in monolayer group IV monochalcogenides,” *2D Materials*, vol. 4, no. 1, pp. 015042.



## **Appendix A: Description of research for popular publication**

Title: structural phase transitions in 2-D atomic materials

By: Mehrshad Mehboudi

Two-dimensional materials which are made of one or few atom thick regular bulk materials have many unique properties that are different and more desirable compared to their bulk parents. For example, graphene – one layer of graphite – is harder than steel and has much higher thermal and electronic conductivity. Recently a new class of two-dimensional materials was predicted to be stable as the next candidates of optoelectronic devices. These materials which have only one sheet of atoms are compounds of group IV and group VI of the periodic table, for example, tin selenide (SnSe) or germanium sulfide (GeS). The crystalline structure of these materials can be built by putting together small and equal rectangular cells called unit cells. Each rectangle consists of four atoms (two of each element). This research predicted that this class of material acts differently than other 2D materials because there are four ways to create their atomistic arrangement. These four ways compete with each other and may cause disorder in the structure at room temperature. In addition, it was numerically predicted in this research that at a certain temperature, the rectangular unit cell of some of these materials will convert to square ones. These changes in the structure will modify properties of these materials and lead to unforeseen optoelectronic properties. Therefore, temperature can be used to modify the properties of these materials. A change in electronic properties of these materials upon passing the transition temperature is also predicted. For example, piezoelectric properties (capability to produce electricity by applying mechanical deformation to the material) of these materials reduces significantly due to phase transition.

The study of 2D materials will revolutionize many fields of study such as electronics,

lasers, transistors, filters, digital screens and sensors. The essential part of these applications are semiconductors. Semiconductors are used in most of electronic devices from computers to cell phones. In order to have faster computers and cell phones, we need to use a material that has high electronic mobility and can be integrated into nano-scaled transistors. While most electronic devices are made of silicon, search for new alternative materials with higher electron mobility is always desirable. For many years, the main approach to increase the speed of computers was to reduce the size of silicon transistors. However, this approach has reached physical limitations which has led researchers to find alternative materials for silicon. 2D materials such as phosphorene and monochalcogenide monolayers are viable alternatives for silicon due to many unique electric properties. The surface of 2D materials are very sensitive because almost every atom of these materials is on the surface. Therefore, sensors made from 2D materials potentially can detect very small changes that cannot be detected by current sensors.

The variety of 2D materials with extraordinary properties has made these materials one of the most investigated class of materials which can be new arsenal for future industries.

## **Appendix B: Executive summary of newly created intellectual property**

The following intellectual property was created in this research:

1. 2D structural phase transition in group IV monochalcogenide monolayers and bilayers.
2. Several MATLAB codes, Linux scripts, and FORTRAN codes for extracting and analyzing data.

## **Appendix C: Potential patent and commercialization aspects of listed intellectual property items**

### **C.1 Patentability of intellectual property (Could Each item be patented)**

1. 2D structural phase transition in group IV monochalcogenide monolayers and bilayers is a behavior of studied materials and is not patentable.
2. Codes that are developed to analyze data are not patentable.

### **C.2 Commercialization prospects (should each item be patented)**

1. The 2D phase transition in group IV monochalcogenides monolayers and bilayers could not be patented as a commercialized product.
2. The code also could not be patented as a commercialized product.

### **C.3 Possible prior disclosure of IP**

1. The results of the research are disclosed (see Appendix G).
2. The codes are not disclosed to the public and it is only available in the research group. The codes can be shared if direct interest arises.

## **Appendix D: Broader impact of research**

### **D.1 Applicability of research methods to other problems**

The 2D structural phase transition may happen in any 2D material with degenerate ground state. Most of the 2D materials have an asymmetric unicell. The asymmetric unicell will lead to a degeneracy in the ground state. Consequently, there is an energy barrier which separates different degenerate ground states. One can calculate the energy barrier of other 2D material by using the methods explained in this dissertation. For those materials that the energy barrier is less than the melting point, possible disorder in the structure will happen and may affect the properties of the materials. This fact potentially can lead to new properties in materials which opens new doors or research.

### **D.2 Impact of research results on U.S. and global society**

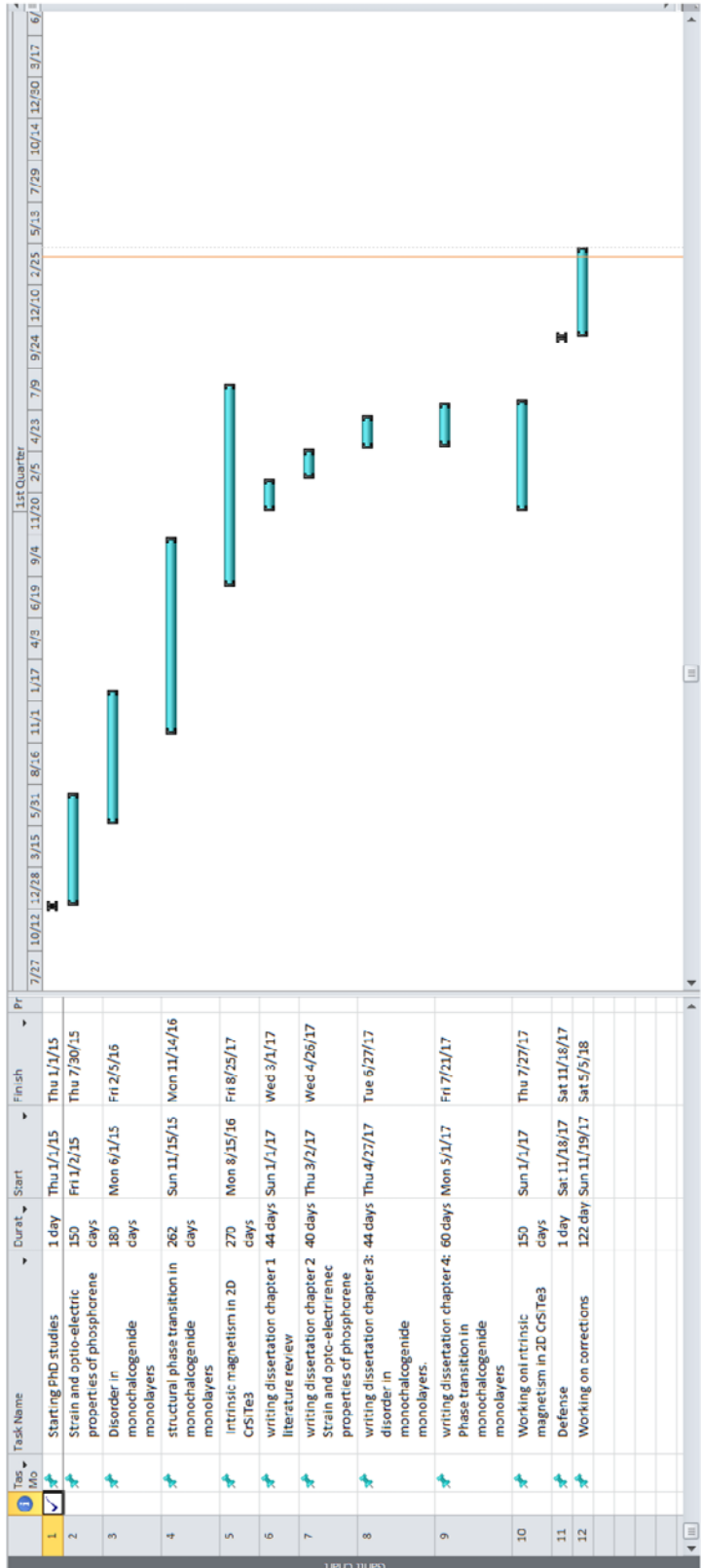
New materials are new arsenals for industries. 2D materials are one of the most exciting areas of material science. This work is significant because it gives insight into a new class of materials with promising applications in optoelectronic devices such as lasers, LEDs, photodetectors, solar cell, piezoelectric materials, computer processors, energy harvesting, and sensors. This work, for the first time, shows that some 2D materials undergoes 2D structural phase transition as a result of temperature which alters their properties. In addition, optoelectronic properties of many of these materials are numerically predicted below and above the transition temperature.

### **D.3 Impact of research results on the environment.**

Research on 2D materials can benefit the environment due to extensive unique properties. Many 2D materials have been discovered that can be used as thermoelectric materials with a very

high figure of merit. These 2D materials which outperform current thermoelectric materials, potentially can revolutionize the energy industries by providing electricity efficiently and reduce environmental pollution. Many 2D materials, such as, few layer black phosphorus, and molybdenum disulfide, are known as the best materials for solar cell application which can directly reduce the hazardous effects of fossil fuel on the environment.

# Appendix E: Microsoft Project for PhD Micro-EP degree plan



## **Appendix F: Identification of all software used in research and dissertation generation**

Computer #1:

Model Number: Dell Dimension 8300

Location: Physics building 231

Owner: Professor Barraza-Lopez

Software #1:

Name: Apache open-office

Free License: Downloaded by Mehrshad Mehboudi

Software #2:

Name: MATLAB 2016

Purchased by: University License

Software #3:

Name: Adobe Acrobat Professional 10.0

Purchased by: UA

Software #4

Name: Jmol

Free License: Downloaded by Mehrshad Mehboudi

Software #4:

Name: VMD

Free License: Downloaded by Mehrshad Mehboudi

Computer #2:

Model Number: Dell

Location: Phys 231



Owner: Professor Barraza-Lopez

Software #1:

Name: Linux Ubuntu

Free License: Downloaded by Mehrshad Mehboudi

Software #2: VASP

Name: Apache open-office

Free License: Downloaded Mehrshad Mehboudi

Computer #2: Mullin library computers

Software #1:

Name: MATLAB 2016

Purchased by: UA

Software #2:

Name: Microsoft Office

Purchased by: UA

Software #3:

Name: Adobe Acrobat readers

Purchased by: UA

## Appendix G: Publications and Presentations

### Publications

1. A.A. Pacheco Sanjuan, M. Mehboudi, E.O. Harriss, H. Terrones and S. Barraza-Lopez, "Quantitative Chemistry and the Discrete Geometry of Conformal Atom-Thin Crystals," ACS nano, vol. 8, no. 2, pp. 1136-1146.
2. M. Mehboudi, K. Utt, H. Terrones, E.O. Harriss, A.A. Pacheco SanJuan and S. Barraza-Lopez, "Strain and the optoelectronic properties of nonplanar phosphorene monolayers," Proc.Natl.Acad.Sci.U.S.A., vol. 112, no. 19, May 12, pp. 5888-5892.
3. R. Haleoot, C. Paillard, T.P. Kaloni, M. Mehboudi, B. Xu, L. Bellaiche and S. Barraza-Lopez, "Photostrictive two-dimensional materials in the monochalcogenide family," Phys.Rev.Lett., vol. 118, no. 22, pp. 227401.
4. M. Mehboudi, B.M. Fregoso, Y. Yang, W. Zhu, A. van der Zande, J. Ferrer, L. Bellaiche, P. Kumar and S. Barraza-Lopez, "Structural phase transition and material properties of few-layer monochalcogenides," Phys.Rev.Lett., vol. 117, no. 24, pp. 246802.
5. M. Mehboudi, A.M. Dorio, W. Zhu, A. van der Zande, H.O. Churchill, A.A. Pacheco-Sanjuan, E.O. Harriss, P. Kumar and S. Barraza-Lopez, "Two-dimensional disorder in black phosphorus and monochalcogenide monolayers," Nano Letters, vol. 16, no. 3, pp. 1704-1712.
6. K.L. Utt, P. Rivero, M. Mehboudi, E.O. Harriss, M.F. Borunda, A.A. Pacheco SanJuan and S. Barraza-Lopez, "Intrinsic defects, fluctuations of the local shape, and the photo-oxidation of black phosphorus," ACS Central Science, vol. 1, no. 6, pp. 320-327.

### Presentations

1. M. Mehboudi, K. Utt, H. Terrones, A. Pacheco, E. Harriss, and S. Barraza-Lopez, "Atoms dictating shape: The discrete geometry of conformal two-dimensional materials". APS March Meeting (2015).
2. M. Mehboudi, S. Barraza-Lopez, A.M. Dorio, W. Zhu, A. van der Zande, H. O. Churchill, A. A. Pacheco-Sanjuan, E. O. Harriss, and P. Kumar, "Ground state degeneracy, energy barriers, and molecular dynamics evidence for two-dimensional disorder in black phosphorus and monochalcogenide monolayers at finite temperature". APS March Meeting (2016).

3. S. Barraza-Lopez, M. Mehboudi, P. Kumar, E.O. Harriss, H.O. Churchill, A.M. Dorio, W. Zhu, A. van der Zande, A.A. and Pacheco SanJuan, “Two dimensional disorder in black phosphorus and layered monochalcogenides”. APS March Meeting (2016).
4. M. Mehboudi, K. Park, and S. Barraza-Lopez, “Intrinsic magnetic behavior in CrSiTe<sub>3</sub> monolayers”. APS March Meeting (2017)